Experimental Implementation of a Quantum Game

Diplomarbeit an der Fakultät für Physik
der
Ludwig-Maximilians-Universität München
Arbeitsgruppe Prof. Dr. Harald Weinfurter

Carsten Schuck

22. Juli 2003

Erstgutachter: Prof. Dr. Harald Weinfurter
Zweitgutachter: Prof. Dr. Klaus Sengstock

Contents

1 Introduction

The combination of game theory and quantum information led to the new field of quantum games. The classical theory of games, which is a well established discipline of applied mathematics, and quantum communication are both concerned with *information* and how information is processed and utilized.

Game theory analyzes situations of interactive decision making and provides models of conflict and cooperation [1]. It has numerous applications, most importantly among many others in economics, social sciences, politics and biology. However, in every game the players have to inform the other players or the game's arbiter about the decisions they take for the game to evolve. In fact the players need to communicate information.

Quantum mechanical systems offer new possibilities for the communication and processing of information. The basis for the theory of quantum information and computation [2] will be shortly reviewed in section 2.1. Accordingly, one can provide the players of a game with quantum mechanical systems as carriers of information they need to communicate. As this extends the possibilities for communication, novel strategies become possible in quantum games.

It turns out that entanglement and linear combinations of the classical strategies can enable the players to reach higher benefits in the quantum mechanical version of a game than classically achievable (s. section 2.2). Yet, quantum communication problems also can be viewed in the light of game theory. Just as new solutions to classically unsolvable games can be found in quantum game theory, it is the aim of some quantum communication protocols to provide a quantum solution to an otherwise unsolvable classical problem. It is thus possible to rephrase problems in quantum communication or computation as games.

Consider for example eavesdropping in quantum cryptography: To analyse how vulnerable a quantum cryptography protocol is, one can try to find the optimal quantum strategy for an eavesdropper, trying to obtain as much information as possible in a given setup, playing against Alice and Bob, who are trying to communicate securely. Likewise, searching a database for a particular entry can be formulated as game between two players, both trying to find this entry first. The optimal (quantum) strategy in this game then corresponds to an optimal (quantum) algorithm to solve the problem.

As a contribution to the new field of quantum games I will show in chapter 3 how the quantum version of a well known classical game, the *prisoner's dilemma*, can be implemented. The dilemma of the classical game is that it is not possible to maximize the payoff of all rational players with optimal single player strategies. In the quantum version of the game, however, the players are supplied with one subsystem of an entangled state each. If they may perform any quantum mechanically allowed operation to encode their choice of strategy on their respective subsystem before sending it to an arbiter determining each player's benefit, the dilemma can be resolved. It is the goal of this work to realize the idea in practice.

In the experimental part, I will present the first optical realization of this quantum game using polarization-time-entangled photon pairs on which arbitrary (quantum-) strategies can be performed. The entangled photon pairs are generated with high temporal definition in a parametric down-conversion process, explained in section 2.3. It will be shown how a compact and highly efficient entangled photon pair source is set up to generate the initial state of the game (section 3.1). The need for such highly efficient sources of entangled photons grew with the interest in fundamental tests of quantum mechanics (tests of Bell's inequality) and the realization of quantum computation and communication schemes, for example dense coding and teleportation.

To experimentally demonstrate the efficiency of quantum strategies, two players can perform single-qubit operations corresponding to the angular settings of a combination of $\lambda/2$- and $\lambda/4$-waveplates, as discussed in section 3.2. To determine the player's benefits, the final state is transformed into a Bell state and projected onto the complete set of maximally entangled basis-states of the two-particle polarization Hilbert space. This so-called Bell measurement is very important for many quantum communication experiments (e.g. dense coding, teleportation and quantum cryptography [3]), and will be covered in section 3.3. Lütkenhaus et al. presented a no-go theorem for a perfect Bell state analysis of two polarization-entangled qubits involving only linear optical elements [4]. Nevertheless, in this experiment, it will for the first time be possible to perform a complete Bell measurement with a method presented by P. Kwiat and H. Weinfurter [5]; the results are presented in chapter 4.

The idea behind this measurement is to make use of simultaneous entanglement in multiple degrees of freedom. If the photons are entangled in more than one degree of freedom one can operate in a higher dimensional Hilbert space. In our case the intrinsic time-energy entanglement of the down-converted photons will be employed to achieve additional arrival-time correlations of the photons after having passed an asymmetric interferometer with polarizing beam splitters to temporally separate horizontal and vertical polarizations. Since the photons are entangled in the polarization and the time degrees of freedom, i.e. they are embedded in a larger Hilbert space, and a complete Bell state analysis to determine the payoffs is possible. This will for example allow to realize optimal dense coding, where the full two bits of information are encoded in the polarization of the two qubits of a Bell state. This

class of state transformations can be regarded as a realization of a simple non-trivial two-qubit quantum logic network.

Apart from the possibility to distinguish between all four Bell states and the implementation of single qubit gates it is noteworthy that our quantum network involves a controlled NOT operation. The importance of a controlled NOT gate stems from the fact that it is (together with a set of single-qubit gates) a universal quantum gate [6, 7]. Single qubit gates are relatively simple to realize (s. section 3.2), but the controlled-NOT is generally much more difficult to implement, because it requires two separated carriers of quantum information to interact in a controlled manner. Here the advantage of the optical approach, namely the photon's intrinsic lack of decoherence when transported through free space or optical fibers, turns into a drawback. Since the photon-photon interaction is extremely weak and hence takes place with a negligible probability of success, an optical implementation of a two-qubit gate necessarily requires strong non-linearities.

One idea to avoid the need for a direct nonlinear coupling between photons is to mediate the interaction by something else, for example an atom, of course at the expense of introducing noise into the system. Therefore, current experiments are trying to map the state of photons onto atom or ion states and vice versa to implement a non-trivial two-particle gate with these systems. Nevertheless it is desirable to have an optical implemention of such gates with linear elements to avoid all the problems (e.g. decoherence, noise, more complex setups, etc.) that come with schemes involving atoms or ions.

A circumvention of the necessity for a strong non-linearity to implement a controlled-NOT gate has been proposed by E. Knill, R. Laflamme and G.J. Milburn (KLM). They showed that scalable quantum information processing with linear optical elements "is possible in principle but technically difficult" [8]. Their scheme for "efficient quantum computation" requires phase shifters, beam splitters, deterministic (i.e. on-demand) single-photon sources and the intrinsic non-linearity of highly efficient discriminating single photon detectors. They propose that it is possible to increase the probability of success asymptotically (as $n/(n+1)$) at the expense of an increasing number (n) of auxiliary photons which have to be independently prepared in any desired entangled state. Using beamsplitters it is possible to couple the additional auxiliary modes to the initial input state so that the resulting state is living in the direct product of the two Hilbert spaces and therefore, a larger Hilbert space as well.

Of course, our approach is not sufficient for the implementation of general purpose controlled-NOT operation in universal quantum networks, because it requires entanglement in more than one degree of freedom, which will generally be difficult to achive. But since the generation of the necessary entangled ancilla states in the KLM scheme is very challenging, it is interesting to apply the presented idea of entangled states embedded in higher dimensional Hilbert spaces as an extension.

In the following I will present the first optical implementation of a quantum game, showing how entanglement and quantum strategies give rise to a new solution of a classically unsolvable game. For the first time a complete Bell state analysis with linear optical elements is performed utilizing entanglement in higher dimensional Hilbert spaces. Furthermore, results will be given demonstrating optimal dense coding.

2 Theory

Contents

2.1 Quantum Information

The discussions and research concerning the foundations of quantum mechanics has led to the new field of quantum information and communication in recent years. The debate about how much information a quantum state may contain and whether this information completely decribes the state, brought up a new treatment of information for quantum systems and many ideas how to perform classically impossible information processing tasks.

Quantum information processing deals with all forms of communication tasks, i.e. transmission of information through a channel from a sender to a receiver, making use of quantum mechanical systems and operations. Therefore, the quantum theory of information depends on how information can be encoded in a carrier (e.g. photons and atoms),involving entanglement and coherent superpositions of states, which I will describe in the following paragraphs.

In the mathematical formalism of quantum mechanics, a *state* is treated as a vector in a Hilbert space and *observables* are represented by hermitian, generally incompatible (i.e. non-commuting) operators.
In quantum information theory a state is in the first place understood as the representation of information carried by a physical system.

The fundamental concepts in quantum information theory are the superposition principle and entanglement. Their importance most prominently becomes apparent in quantum computation applications, where many computational tasks can be performed simultaneously. In a classical physics context, information is always defined by the observation of measurement results but in quantum physics it is possible to simultaneously process information encoded in linear combinations of states incompatible with the classical coding scheme of information. This is the reason why certain problems, such as integer factorization or simulations of many particle quantum systems, can be solved very efficiently using a quantum computer, although it may not perform better than classical computers in general purpose computation. The computation of these particular problems speeds up exponentially with the number of input qubits if it is possible to utilize (destructive) interference of parallel processed information to limit the number of possible output states.

Within quantum theory one has to distinguish between classical and quantum information. Classical information can be copied without any restrictions, but in accordance with general relativity it cannot be distributed faster than at the speed of light. On the contrary, properties of entangled systems can simultaneously be present at different locations. The key feature distinguishing quantum from classical information theory are the non-classical correlations between outcomes of mea-

surements performed on physical carriers of (quantum) information. Therefore, an important task of quantum information theory is to characterize entanglement and its interrelation with classical information.

Although it is understood that entangled composite systems have more information contained in the correlations of measurement outcomes than any classical mixture of its individual constituents could ever have, there are still open questions. For example, it is still discussed what the most general constraints are the correlations have to violate in order to be called non-classical, and which classes of states violate these constraints, especially for higher dimensional and for multipartite states. In this chapter I will only describe some of the currently discussed most general criteria for entanglement, as violation of a Bell inequality or entanglement witnesses based on separability criteria, but there are already new approaches to this question [9].

In the following I will introduce some of the common notations and concepts of quantum information processing. Furthermore, I will briefly review the historic discussion about the foundations of quantum mechanics to show where current research interests originate and to clarify what the distinct quantum features are from which the new possibilities of quantum information arise. However, a more extensive overview of quantum information and computation can be found in [10, 11, 2].

2.1.1 Qubits

The basic unit of classical information is called a **bit**. For example, it can be implemented by a two-state system, with (boolean) states one may call $|0\rangle$ and $|1\rangle$, which can take on two different logical values, 0 and 1. The two states could be realized as two distinguishable voltages (as in classical computers) or two different polarization states ($|H\rangle$, $|V\rangle$) of a photon.

In quantum mechanics a two-state system may also exist in any *coherent superposition* of the two distinguishable classical states: $|\psi\rangle = a|0\rangle + b|1\rangle$. A single bit of binary information contained in a two-state quantum system is therefore called a quantum bit or **qubit** and is the quantum analog of the classical bit. Typically a qubit is carried by a microscopic system where the two classical boolean states $|0\rangle$ and $|1\rangle$ form the basis of a two-dimensional Hilbert space $\mathbb{H}$. The continuous set of superposition states is represented by complex linear combinations of basis states. The coefficients squared absolute values can be interpreted as probabilities which have to sum up to unity, $|a|^2 + |b|^2 = 1$. If measured, the system is found randomly in one of the two states, according to the probability distribution. As any qubit can be represented as a vector on the Bloch or Poincaré sphere (s. Fig. 2.1), two quantum states can only be unambiguously distinguished from each other if they are orthogonal.

The state in which the qubit is encoded has no analog in classical physics, since it has to be a coherent superposition and not an incoherent mixture of the classical states! Contrary to incoherent mixtures, for coherent superposition states it is always possible to find a transformation of the basis of the state space such that the qubit transforms into a basis vector with a well defined qubit-value.

The most famous example of quantum superposition is single photon interference observed in the double slit experiment or in a Mach-Zehnder interferometer. In both examples the condition for interference to occur is the fundamental impossibility to determine which path (slit) the photon took.

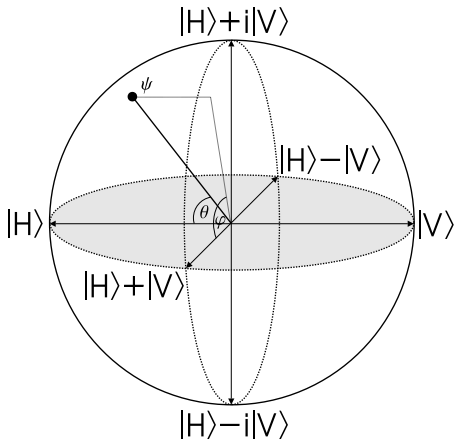

Figure 2.1: Poincaré sphere representation of a qubit's Hilbert space.

2.1.2 Entanglement

New and especially interesting features for quantum information processing arise when one considers two (or more) qubit systems.

It is straightforward in a classical coding scheme to encode one bit of information on each qubit. A pair of qubits[1] could then be prepared in any of the four boolean states, $|00\rangle$, $|01\rangle$, $|10\rangle$ and $|11\rangle$. However, in quantum mechanics it is also possible to encode the information onto a pair of qubits in any superposition of the four classical states $|00\rangle$, $|01\rangle$, $|10\rangle$ and $|11\rangle$, in particular also onto entangled states which contain correlations between their subsystems, much stronger than any classical correlation. The way the information is encoded either in the properties of the individual subsystems or in the joint properties of both qubits the states are labeled "separable" or "entangled". All two-qubit states are called *separable* if they can be written as a combination of tensor products of single particle states (s. 2.1.3). All classical states are separable because they can completely be described by the properties of each part separately. All other states are called non-separable or *entangled* states[2]. For these states it is generally not possible to attribute to each subsystem individually any well defined information (i.e. a definite state vector), only all qubits together contain all the information.

For a quantum system with two qubits the four orthonormal maximally entangled states forming a complete basis of a four dimensional Hilbert space are called

[1] For n qubits the quantum state could be represented by a vector in a 2^n-dimensional Hilbert space, where every dimension corresponds to a different classical state: $\psi = \sum_{i=0\ldots2^n-1} p_i|i\rangle$

[2] The term "*entanglement*", or "Verschränkung" in german, was introduced by Schrödinger in [12].

Bell states[3]. They are coherent superpositions of four possible separable states:

$$|\psi^+\rangle = \frac{1}{\sqrt{2}}(|HV\rangle + |VH\rangle) \tag{2.1}$$

$$|\psi^-\rangle = \frac{1}{\sqrt{2}}(|HV\rangle - |VH\rangle) \tag{2.2}$$

$$|\phi^+\rangle = \frac{1}{\sqrt{2}}(|HH\rangle + |VV\rangle) \tag{2.3}$$

$$|\phi^-\rangle = \frac{1}{\sqrt{2}}(|HH\rangle - |VV\rangle) \tag{2.4}$$

These states have the property that it is enough to manipulate only one of the two entangled photons to transform one basis state into any other of the four Bell states. Thus it is possible with single qubit operations to encode two bits of information per photon, i.e. four possible orthogonal states of a two-photon system [13].

2.1.3 Verification of Entanglement

In quantum information, entanglement is one of the central resources to realize quantum communication protocols. Hence it is important for experimental implementations to verify that one really created an entangled state, e.g. with spontaneous parametric down conversion (s. section 2.3.2). The most simple example of an entangled state is a *pure state* ρ_{ab}, for which the reduced density matrices of its subsystems are diagonal[4]. In general, however, a state which is intended to be an entangled pure state will be in a *mixed state*[5] or might even be separable due to imperfections and its uncontrollable interaction with the environment.

To detect whether a given state is entangled, there are different methods such as tests of the polarization correlations (s. section 4.1), generalized Bell inequalities (s. equation (2.6)) and witness operators (s. equation 2.13).
Given a pure state, all of the above criteria are able to satisfactorily show that it is entangled. For experimentally generated two-qubit states a general criterion based on the properties of the partial transpose of the state was found to be a sufficient test for entanglement. For higher dimensional mixed states however, no such general criterion could be obtained to test if existing correlations of measurement results are

[3]These states maximally violate a *Bell* inequality, therefore they are called *Bell* states.

[4]The reduced density matrix of one subsystem can be found by tracing ρ_{ab} over all states of the other subsystem (e.g. $\rho_a = Tr(\rho_{ab})_b = \sum_{i=0,1}\langle i|\rho_{ab}|i\rangle = \sum_{i=0,1}|p_i|^2|i\rangle\langle i|$)

[5]Mixed states can be produced in many different ways but it is not possible to find out how a given mixed state actually was produced and thus one cannot extract all the information the state really contains.

quantum or not. Only for some particular cases it is possible to find out what kind of correlations they contain using the so-called entanglement witness operators.

In the following I will review the discussion about EPR's paradox, because it first pointed out the remarkable features of entangled states and it led to the first method (Bell's inequality) to distinguish some of them from classical (or separable) states. Then witness operators are presented, which are a rather new and more powerful tool to detect entanglement compared to Bell's inequality.

EPR's Paradox

The counterintuitive features of entangled quantum systems were used by Einstein, Podolsky and Rosen (EPR) to argue that the quantum mechanical description of the physical reality cannot be considered complete [14]. They understand a theory to be complete if every *element of the physical reality* is represented in the physical theory and they give the following **criterion of reality**:
"If, without in any way disturbing a system, we can predict with certainty (i.e. with probability equal to unity) the value of a physical quantity, then there exists an element of physical reality corresponding to this physical quantity."
One assumption underlying the EPR-paper is *Einsteins locality principle*[6] stating that the properties observed on one subsystem are independent of whatever manipulation and measurement is performed on any other subsystem, together making up for the whole composite system. For completion they suggested that there might be a supplementary, more exact picture, in which individual systems are described by their wavefunction and additional *hidden variables*[7].

Bohm explicitly constructed a hidden variable interpretation of quantum mechanics [16] and rephrased the EPR argument for two spin-$\frac{1}{2}$ particles in a singlet state [17]:

$$|\psi\rangle = \frac{1}{\sqrt{2}}(|\uparrow\rangle_a|\downarrow\rangle_b - |\downarrow\rangle_a|\uparrow\rangle_b) \tag{2.5}$$

The spin singlet state is spherically symmetric and has no preferred direction in space. Note, that if one identifies the spins with polarizations one recognizes one of the Bell states, which can be used as the necessary input state for our experiment.

N. Bohr [18] was the first to realize that knowing the state of a composite system does not necessarily mean that one has knowledge about its parts, which are not in any defined state - the feature we refer to as nonseparability.

None of the two qubits in (2.5) has a defined bit value and it is impossible to predict which of the two possible product states will be realized if a measurement is performed on one of them, instantaneously determining the value of *both* qubits.

[6] *"But on one supposition we should, in my opinion, absolutely hold fast: the real factual situation of the system S_2 is independent of what is done with the system S_1, which is spatially separated from the former."* A. Einstein in [15]

[7] The parameters are called "hidden" because their values cannot directly be measured.

This holds true even if the qubits are separated by an arbitrary distance. This feature, called *nonlocality*, is a consequence of linear superpositions of correlated many particle states and cannot be reproduced classically, i.e. on the basis of local properties of the subsystems[8]. For a more detailed discussion of the paradox and its philosophical aspects see [19, 20].

Bell's Inequality

The underlying philosophical concept of local hidden variable (LHV) theories is called *local realism*[9]. A hidden variable theory making the same predictions as quantum mechanics can be shown to necessarily involve either signals propagating instantaneously between spatially separated particles and hence not being Lorentz invariant [21, 22] or being not deterministic and thus measurement results would be inherently unpredictable. In 1964, Bell [23] used these peculiarities to formulate a testable inequality for observables of spin correlation experiments, for which predictions of hidden variable theories based on Einsteins locality principle and the requirement for determinism do not agree with the statistical predictions of quantum mechanics.

Clauser, Horne, Shimony and Holt (CHSH) generalized Bell's theorem [24] such that it applies to realizable experimental tests with pair detection of all local hidden variable theories. A proof of the *CHSH inequality* by Bell can also be found in [22], here I rather give the result. For any local hidden variable theory the expectation values $E(i,j)$ of spin measurements on two particles have to fulfill the inequality

$$-2 \leq S_{Cl}(\alpha,\alpha',\beta,\beta') = \\ E(\alpha,\beta) - E(\alpha,\beta') + E(\alpha',\beta) + E(\alpha',\beta') \leq 2 \tag{2.6}$$

for *any* combination of analyzer settings $i = \alpha, \alpha'$ and $j = \beta, \beta'$. The proof of Bell's theorem is then completed by showing, that there in fact exist analyzer settings for which the predictions of quantum mechanics violate the inequality $|S_{Cl}| \leq 2$. For entangled two-qubit states,

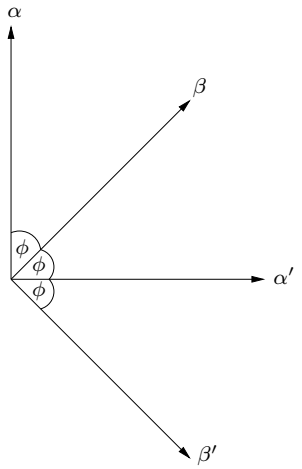

Figure 2.2: Orientations of $\alpha, \alpha', \beta, \beta'$ for maximal violation of the CHSH inequality (2.6).

[8] Note that nonlocality does not contradict relativity because no information is transfered when the result of a measurement on particle a is determined and hence the result of a similar measurement on the other particle, b, is known instantaneously, since the correlation can only be ascertained by a subsequent comparison through a classical channel.

[9] Realism follows from the criterion of reality and locality, which deduces from causality, i.e. the cause has to precede its effect, and relativity, i.e. all inertial frames are equitable.

maximal violation occurs for the orientations shown in figure 2.2 with $\phi = 45°$. For this case one obtains Cirel'son's upper bound [25] on S for quantum mechanics:

$$S(\alpha, \alpha', \beta, \beta')_{QM} = 2\sqrt{2} > |S_{Cl}|. \tag{2.7}$$

Bell's inequality shows that entanglement leads to observable effects which confirm the existence of entangled states.

How to actually observe such a violation of Bell's inequality in a laboratory was first shown for a set of local measurements on the two subsystems of an EPR singlet state by Fredman and Clauser [] and later most prominently by A. Aspect et al. [26, 27, 28] with photons[10] and by M. Lamehi-Rachti and W. Mittig [30] with protons.

All experiments to date (for an overview see [19, 22]) are in agreement with the predictions of quantum mechanics and hence confirm[11] the existence of the entangled states needed for my experiment.

Entanglement Witness

Another possibility to detect entanglement is the application of so called *entanglement witnesses*. I will explain this concept in more detail, because it is not covered in standard text books. This approach is not intended to rule out any local hidden variable theories (in fact for the example below it is possible to construct a LHV model which reproduces the quantum mechanically expected results) but the overall motivation is to characterize the set of separable and entangled states.

The starting point is the *separability problem*:
When does the state of a composite quantum system contain no quantum correlations or entanglement?
As discussed in [31, 32], non-separability in quantum mechanics implies non-classical phenomena.

A state ρ is called separable if ρ can be written as a combination of product states forming a convex set [33]:

$$\rho_{sep} = \sum_{i=1}^{k} p_i \rho_i^a \otimes \rho_i^b, \tag{2.8}$$

with $\sum_i p_i = 1$ and $p_i \geq 0$. If the expectation value of a joint measurement of two observables, A and B, acting on two respective subsystems always factorizes

[10] More recent tests of "Bell's Inequality under Strict Einstein locality Conditions" are presented in [19, 29].

[11] Since detection efficiencies of greater than 71% are required for experimental tests of Bell's inequality all tests today rely on some feasible but not testable assumptions (e.g. the fair sample assumption) from which loopholes could be constructed.

$Tr[(A \otimes B)\rho_u] = Tr[A\rho_u]\ Tr[B\rho_u]$, the corresponding state ρ_u is said to be uncorrelated. In case the expectation value does not factorize $Tr[(A \otimes B)\rho^{ab}_{sep}] = \sum_{i=1}^{n} p_i\ Tr[A\rho^a_{sep,i}]\ Tr[B\rho^b_{sep,i}]$ the state ρ^{ab}_{sep} (2.8) is termed classically correlated. A separable state contains no quantum correlations because it can be prepared by two parties using only local operations and classical communication (LOCC). Consequently, a mixed state of a composite quantum system is called non-separable if it cannot be written as a convex combination of product states.

The Horodeckis showed that non-separable states can be identified by means of positive maps[12]. In fact the characterization of entanglement and separability is rather a mathematical problem of how to classify and characterize positive operator maps [31, 34].
Peres found that as a necessary condition for separability [35] of a given state ρ the partial transpose (s. A.2), $\rho^{T_a} = \sum_{i=1}^{k} p_i(\rho^a_i)^t \otimes \rho^b_i$, is only allowed to have non-negative eigenvalues.

From the fact that positive maps as well as partial transposition preserve hermiticity, although they are not a unitary operation, the Horodeckis deduced a sufficient condition for separability [31]:

A state ρ is separable if and only if the tensor product of every positive map acting on subsystem a and the identity acting on subsystem b maps the state ρ onto a non-negative operator.

Together with the necessary condition of Peres one obtains the following theorems [31, 35]:

Theorem 1 (Peres-Horodecki) *If ρ is separable then $\rho^{T_a} \geq 0$.*

Theorem 2 (Peres-Horodecki) *If $\rho^{T_a} \geq 0$ in composite Hilbert spaces of dimensions 2×2 or 2×3, then ρ is separable.*

For higher dimensional Hilbert spaces there exist bound entangled states[13] which are not separable.

For *bipartite density matrices*, ρ_{ab}, a necessary and sufficient condition for separability involving the witness operator W was introduced by B. Terhal [34, 36]:

Theorem 3 (Terhal) *If ρ_{ab} is entangled, then there exists a hermitian operator W acting on $H_a \otimes H_b$ such that:*

$$Tr(W\rho_{ab}) < 0 \text{ and } Tr(W\rho_{ab,sep}) \geq 0$$

for all positive semidefinite separable density matrices $\rho_{ab,sep}$.

[12] Maps are said to be positive if they map positive operators onto positive operators. Positiv operators, P, are a subclass of Hermitian operators which have the property that for any vector $|v\rangle$ the inner product, $\langle v|P|v\rangle$, is real and non negative.

[13] i.e. entangled states with positive partial transpose (PPT) from which no pure entangled state can be distilled.

To prove this theorem, one has to show the existence of a hyperplane separating the set of all separable density matrices on $H_a \otimes H_b$ from the point corresponding to ρ_{ab}. This hyperplane (s. Fig. 2.3) is a set of density matrices, τ, characterized by its normal vector W, i.e. $Tr(W\tau) = 0$, which defines a positive map. Therefore one can say that W detects entanglement and it is called an *entanglement witness*. The hyperplane is perpendicular to the connecting line between the identity (at the center of the set of separable states) and the density matrix in question.

From figure 2.3 it is clear that the most useful witnesses correspond to hyperplanes being tangent on the set of separable states. A witness is said to be optimal if no other witness can be found which detects more entangled states. An optimal witness therefore has to touch the set of separable states and then has to be rotated until it detects a maximum of entangled states [37].

For a given experimental situation where we aim at producing a certain state, in our case a Bell state, it is always possible to construct an optimal witness operator in the following manner [38]. Consider the case that we aim at producing the pure Bell state (2.3)

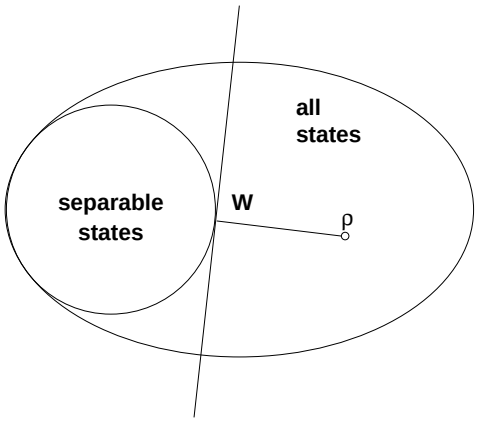

Figure 2.3: Schematic representation of a (optimal) witness operator.

$$\rho_{ab}(\phi^+) = |\phi^+\rangle\langle\phi^+| = \frac{1}{2}\begin{pmatrix} 1 & 0 & 0 & 1 \\ 0 & 0 & 0 & 0 \\ 0 & 0 & 0 & 0 \\ 1 & 0 & 0 & 1 \end{pmatrix}. \tag{2.9}$$

Due to noise, represented by the mixed state σ, in the experiment we will effectively have produced the convex combination

$$\rho_{ab} = p|\phi^+\rangle\langle\phi^+| + (1-p)\sigma \tag{2.10}$$

with the (unknown) probability $0 \leq p \leq 1$ of having produced the desired entangled state, $\rho_{ab}(\phi^+)$ and white noise σ. To construct the entanglement witness W, which fulfills theorem 3, one has to find the eigenvector $|e_{min}\rangle$ of $\rho_{ab}^{T_a}(\phi^+)$ corresponding to an eigenvalue $\lambda_{min} < 0$. Solving the eigenvalue equation $\rho_{ab}^{T_a}(\phi^+)|e_{min}\rangle = \lambda_{min}|e_{min}\rangle$ for the particular case of white noise, corresponding to the maximally mixed state $\sigma = \frac{1}{4}\mathbb{1}$, one obtains the minimal eigenvalue $\lambda_{min} = -1/2$ and the corresponding minimal eigenvector $|e_{min}\rangle = (|HV\rangle - |VH\rangle)/\sqrt{2}$. Therefore, according to the Peres-Horodecki criteria (theorems 1 & 2) $\rho_{ab}(\phi^+)$ is not separable and we obtain

the optimal witness operator which detects the entanglement of ρ_{ab}:

$$W = (|e_{min}\rangle\langle e_{min}|)^{T_a} = \frac{1}{2}\begin{pmatrix} 0 & 0 & 0 & -1 \\ 0 & 1 & 0 & 0 \\ 0 & 0 & 1 & 0 \\ -1 & 0 & 0 & 0 \end{pmatrix}. \tag{2.11}$$

It can now be shown [39] that this witness also works for any other kind of noise.

To be able to experimentally test whether a given (imperfect) state is entangled or not, one has to decompose the witness operator into a sum of local projectors on product states[14]. With the definitions given in A.2, one finds the optimal decomposition to be

$$W = \frac{1}{2}(|HV\rangle\langle HV| + |VH\rangle\langle VH| - |PP\rangle\langle PP| - |MM\rangle\langle MM| + |LL\rangle\langle LL| + |RR\rangle\langle RR|). \tag{2.12}$$

and one determines

$$Tr(W\rho_{ab}) = \sum_{i,j}\langle ij|W\rho_{ab}|ij\rangle \tag{2.13}$$

Since the trace is invariant under basis transformations[15], it can be written as a sum of expectation values which correspond to measurement values (s. 4.1). Assuming that σ is white noise, one can calculate [38] the probability $p = (1 - 4Tr(W\rho_{ab})]/3$. Note that in general, a witness does not provide a measure of entanglement.

Thus it is possible with this method to determine if the produced state ρ_{ab} is entangled, i.e. $Tr(W\rho_{ab}) < 0$ and with which probability p we really generated the desired pure state $\rho_{ab}(\phi^+)$.

Although a Bell inequality is some kind of entanglement witness, the criteria for non-separability of Peres, Horodecki and Terhal (Theorems 1-3) are stronger than any known Bell inequality in the following sense: Even though every pure entangled bipartite state and many distillable[16] mixed bipartite states violate a Bell inequality, while separable states don't, there exist non-separable states which do not violate any known Bell inequality. A Bell inequality can therefore be understood as an entanglement witness which is not optimized. Hence, states which are lying close to the set of separable states might not be detected by a Bell inequality. For example Werner states (a mixture of a maximally entangled state and the separable maximally mixed state, i.e. the identity operator) only violate the CHSH inequality if the

[14] Of course, the state can also be determined performing state tomography with local measurements only and then checking for nonpositivity of its partial transpose but this requires many more measurements then the witness-method.

[15] $Tr(\rho_{ab}) = \sum_{i,j}\sum_{m,n}\langle ij|mn\rangle\langle mn|\rho_{ab}|ij\rangle = \sum_{i,j}\sum_{m,n}\langle mn|ij\rangle\langle ij|\rho_{ab}|mn\rangle = \sum_{m,n}\langle mn|\rho_{ab}|mn\rangle$

[16] Distillable states are mixed entangled state which can be mapped onto a pure entangled state using only LOCC and auxillary measurements.

probability of having the maximally entangled state in the mixture exceeds $1/\sqrt{2}$. However, they are entangled if and only if the probability p is higher than $1/3$ and this entanglement can be detected by a witness [40]. For two-qubit states the Peres-Horodecki is sufficient to detect all entangled states. However, for higher dimensional and multipartite states it is unknown until now whether all (e.g. PPT) entangled states violate some Bell inequality. Entanglement witnesses are (currently) able to detect more non separable states than a Bell inequality, and therefore, this method will be used in the experimental part of this work as a state-of-the-art technique, demonstrating the presence of entangled states.

2.2 Game Theory

The theory of games is the theory of interactive decision making and tries to forecast which will be the most rational development of a given game. It provides mathematical models and techniques to analyse situations (competition as well as cooperation) in which several parties have to make a decision, according to their individual interests, influencing one anothers welfare.

To understand how decisions are made games serve as hypothetical examples of social situations involving individuals called players. The models may appear unrealistically simplified than the more complicated situations of real life, but by ignoring the less important details of reality it is possible to focus on the more fundamental questions of conflict and cooperation.

In a game two (or more) players are trying to reach a final state which ensures them the best benefit as a cooperation or as an individual. The *Strategic* or *Normal Form Representation* of a game consists of [41]:

- set of players ($i = 1, ..., N$)
  The players are assumed to act rational and intelligent. Rational means that they will try to maximize their individual expected payoffs measured in some utility scale and intelligent is meant in the sense that they understand game theory and the behavior of other intelligent[17] players.

- set of strategies ($\mathcal{H}, \{s_i\}$)
  The strategies are the options available to the players in certain game situations. According to the rules, they determine the allowed states of the game associated with the state space $\mathcal{H}$ and the permissible operations of the players which define the strategic space S_i from which each player, i, has to choose one strategy.

- payoff functions ($\$_i$)
  The payoff or utility function $\$_i$ specifies the benefit, i.e. a real number, of the i- th player for a given final state of the game. This quantitative characterization of an individual players preference depends on the strategies of all other player's too.

The behavior of the players can be understood by the *expected-utility maximation theorem* [1]. It follows from models of evolutionary selection for complex organisms (e.g. social organizations) that "there must exist some way of assigning

[17] I'm not trying to make a statement about businessmen here, but as a matter of fact there do exist theories in economics assuming rationality but NOT intelligence of the players, e.g. price theory.

utility numbers to the various possible outcomes [that a rational decision-maker] cares about, such that he would always choose the option that maximizes his expected utility" [1]. The possible operations (according to the rules) performed by the players can be referred to as *moves*. An instruction that specifies the move to be made in each possible game situation is called a *strategy*, and the combination of strategies that the players might choose is a *strategic profile*. If a player opts for a *pure* strategy, he or she will always play a given move depending on the actual situation of the game. In *mixed* strategies a player will select one move from a subset of different moves with a certain classical probability (s.2.2.1).

Of particular interest are *static games of complete information*. A game is called *static* when all players choose their actions simultaneously, i.e. without knowing what the other players are going to do, contrary to dynamic games where the players perform sequential moves by turn, like in chess. Furthermore, each player knows the values of the payoff functions of all opponents and has therefore *complete information* about the consequences of all possible choices.

For this class of games, one distinguishes *zero sum games*[18], where the expected payoffs of all players sum up to zero for every final state (e.g. in a two-player game: $\$_A(s_A, s_B) = -\$_B(s_A, s_B)\ \forall s_A \in S_A, s_B \in S_B$), and *non-zero sum games* otherwise. In zero sum games the interests of the players are diametrically opposed, while in non-zero sum games they no longer appear in strict opposition to each other, but may rather benefit from mutual cooperation.

The goal of game theory is to find that ensemble of strategies that gives each player the best chance of winning. Hence the rational *Solution of the Game* is the strategic profile which is actually played. It is said to be acceptable only if it unambiguously specifies one such profile.

2.2.1 Classical Solution Concepts

To find the rational solution of a game there are classical concepts [41] which I will present in the following. Thereby any rule that specifies a prediction about how the players are expected to behave is meant by a 'solution concept'.

Elimination of strictly dominated strategies

A strategy s_i of the i-th player is strictly dominated by another strategy $s_i^{'}$ if

$$\$_i(s_1, ..., s_i, ..., s_N) < \$_i(s_1, ..., s_i^{'}, ..., s_N) \quad \forall \quad (s_1, ..., s_{i-1}, s_{i+1}..., s_N). \tag{2.14}$$

Since rational players are trying to maximize their benefits, they won't play strictly dominated strategies. Therefore, one may find a rational solution by eliminating all

[18] The fundamental theorem of "zero-sum" games was published by the Hungarian mathematician John von Neumann [42]

strictly dominated strategies. However, for some problems there are no dominating strategies and hence new solution concepts are needed.

Nash Equilibrium

A very important concept to find a solution to a non-zero sum game is the determination of Nash[19] Equilibria.

A **Nash equilibrium** is a strategic profile $(s_1^*, s_2^*, ..., s_N^*)$ where every strategy s_i^* satisfies

$$\$_i(s_1^*, ..., s_i^*, ..., s_N^*) \geq \$_i(s_1^*, ..., s_i, ..., s_N^*) \quad \forall \quad s_i \in S_i \tag{2.15}$$

for each player, i.

For example in a two-player game (s_A^*, s_B^*) is called a Nash equilibrium if $\$_A(s_A^*, s_B^*) \geq \$_A(s_A, s_B^*)$ and $\$_B(s_A^*, s_B^*) \geq \$_B(s_A^*, s_B)$ $\forall s_A \in S_A, s_B \in S_B$.

Hence, a Nash equilibrium corresponds to that combination of strategies which is the best choice for each single player if all his opponents take their best decisions, too. Each of the players looking at his move in retrospective comes to the conclusion that he or she could not have done better by unilaterally changing his or her own strategy. It is a stable equilibrium, since no player has a motivation to unilaterally change his strategy from the Nash equilibrium solution, as he would suffer some loss in his own payoff. If only one strategic profile survives the process of elimination of strictly dominated strategies it constitutes a *unique* Nash equilibrium of the game.

The set $(s_1^*, ..., s_N^*)$ is called *Pareto optimal*[20] if it is not possible to increase one players payoff without lessening the payoff of another player. Hence, for a Pareto optimal outcome of a game, there is no other outcome that would make all players better off. A Nash equilibrium is not necessarily Pareto optimal, i.e. efficient, even if it is unique and there can be another outcome which would make both players better off.

But there exist games with no or multiple Nash equilibria, where no rational prediction about the development of the game can be made. Game theory neither shows how to compute a Nash equilibrium nor how to choose a particular one if multiple equilibria are already known. One only gets an acceptable solution if the Nash equilibrium is unique. Thus, a new solution concept is needed for all other problems.

[19] John Nash received the Economics "Nobel" prize in 1994 for his contributions to game theory. In 2001 the life and work of Nash was also subject to the Oscar awarded movie "A Beautiful Mind".

[20] This concept was invented by the Italian economist Vilfredo Pareto.

Mixed Classical Strategies

Within the framework of classical game theory, the players might not only be allowed to play pure strategies, but also mixed strategies. In mixed classical strategies, a probability distribution assigns a classical probability p_i^α to each pure strategy s_i^α; α indicates one out of all possible strategies of the i-th player. If the game would repeatedly be played, the different strategic profiles should appear according to the probability distributions. Allowing the players to utilize mixed strategies also in cases where a game is only played once is actually an extension of the rules, as if you would allow them to use a random number generator, biased depending on their choice of probabilities, when taking the decision which move to play. Depending on the situation of the game, a player will then select the pure strategy s_i^α from the strategic space with probability p_i^α. This probability distribution corresponds to the uncertainty of each player about another players choice of strategy as well as his own in one specific situation of the game.

The payoffs $\$_i$ have to be treated now as the average gain of the i-th player. Hence, the *expected* payoff functions become:

$$\langle \$_i \rangle (\{p_i\}, ..., \{p_N\}) = \sum_{\alpha,\beta,...,\nu} p_1^\alpha p_2^\beta \cdots p_N^\nu \$_i(s_1^\alpha, s_2^\beta, ..., s_N^\nu) \quad , \tag{2.16}$$

where $\{p_i\}$ is the set of probabilities associated with the set of strategies $\{s_i\}$. As an example for two players A and B, and two strategies the probabilities are $\{p_A\} = \{p, 1-p\}\ \forall p \in [0,1]$ and $\{p_B\} = \{q, 1-q\}\ \forall q \in [0,1]$.

It was shown by Nash in 1951 that the following 'general existence theorem' applies to games where classical mixed strategies are allowed:

Theorem 1 (Nash) *In every N-player normal form game with finite state space there always exists at least one Nash Equilibrium in pure or mixed strategies.*

However, this Nash equilibrium does not have to be a unique solution for the problem! One might obtain multiple Nash equilibria which all satisfy the notion of a rational solution so that the theory fails to say which of them represents the real development of the game.

2.2.2 Quantum Solution Concepts

The most important classical solution concepts have been discussed, but there still do remain games which are classically undeterminable, or which have unsatisfactory solutions. An idea brought up by J. Eisert, M. Wilkens, and M. Lewenstein [43, 44] to solve such games is to use **Quantum Strategies** and **Entanglement**.

First I want to specify my terms concerning the meaning of the expressions 'strategy' and 'state' of a game because there has been some confusion about this issue [45, 46]. A strategy is the players choice of what move to play. To clarify

what I mean by the state of a game, consider a game where every player gets a coin, heads up, and has to choose between flipping or not flipping the coin as the only two possible strategies. Initially all coins may be in the 'state' heads up and so is the state of the game. After the players executed their moves the state of the game has changed to some final state depending on the players strategies, i.e. a combination of coins heads up and tails up.

In the quantum mechanical formulation of game theory, the outcome of a classical strategy s_i^α, s_i^β,... of the i-th player is treated as a state represented by basis vectors $|s_i^\alpha\rangle$, $|s_i^\beta\rangle$,... of the strategic space, which is given the structure of an Hilbert Space, $\mathbb{H}_i$. Additionally to the discrete set of basis vectors, also any linear superposition of them, $|\psi_i\rangle = a_i^\alpha|s_i^\alpha\rangle + a_i^\beta|s_i^\beta\rangle + \ldots$, is an allowed state vector. The state of the game formally is a vector in the tensor product space of the single players strategic spaces, $\mathcal{H} = \mathbb{H}_i \otimes \mathbb{H}_j \otimes \ldots$. The resulting Hilbert Space is spanned by the classical game basis, $|s_i^\alpha s_j^\alpha \ldots\rangle$, $|s_i^\beta s_j^\alpha \ldots\rangle$,... It includes the set of all possible quantum states and contains the discrete and finite set of classical (pure and mixed) states as a subspace, where all pure states form a complete basis. Note that by pure and mixed states here I mean states resulting from the players having chosen pure or mixed strategies, not the quantum mechanical notion of pure and mixed states as used in 2.1.2. As the game proceeds, the players are allowed to perform operations represented by unitary matrices acting in $\mathbb{H}_i$, $\mathbb{H}_j$,... respectively, i.e. they act locally on their subsystem only, being able to jointly prepare any state they wish to.

Quantum states of the game therefore are linear combinations of pure classical states with complex coefficients which give the probability of having played a particular pure classical strategy (like for a mixed classical strategy). Hence, in a quantum game one has to compute the expectation values of the players payoffs. Note that we don't expect any quantum interference effects between the amplitudes as long as we are dealing with static games.

Concluding, one distinguishes two types of states on which the players later on perform their local transformation corresponding to the strategy they decided to play:

Factorizable States

Factorizable initial states can be written in the form

$$|\psi_{in}\rangle = \sum_\alpha a_i^\alpha |s_i^\alpha\rangle \otimes \sum_\alpha a_j^\alpha |s_j^\alpha\rangle \otimes \ldots \tag{2.17}$$

Choosing appropriate expressions for their operations, the players will always be able to arrive at the same final state of the game, and the expected payoff functions will remain unchanged, independent of the initial state. Factorizable Quantum States are able to reproduce the results of the mixed classical game if the players are al-

lowed to apply unitary (hermitian) operations on their respective subsystem. Hence, factorizable states correspond to states prepared with classical mixed strategies.

Entangled Quantum States

For entangled quantum states the initial state cannot be written as in equation (2.17). However, the quantum state space contains both the factorizable states, corresponding to the pure and mixed strategies of the classical theory, and the non-factorizable states, which might enable the players to solve classically unsolveable games and unescapable dilemmas [1, 47]. If the subsystems on which the players perform their operations are entangled, the choice of strategy of one player can have an influence on another players subsystem. This considerably extends the range of possible strategies, even though neither player has knowledge of the other's decision.

Here, the choice of the initial state is relevant because the payoff functions corresponding to the Nash equilibria are all initial state dependent. If the state of a game is an entangled quantum state, it corresponds to more than one set of probabilities $\{p_i^\alpha\}$, compared to mixed classical strategies. An entangled pair of states satisfying the Nash equilibrium conditions is the best rational set of choices which is stable against unilateral deviations.

2.2.3 Quantum Games

Generally speaking a quantum game consists of three steps:

1. Selection of an arbitrary initial quantum state from the state space $\mathcal{H}$.

2. Each player's manipulation of the initial state by performing local transformations.

3. Determination of the expected payoff for each player by projecting the final quantum state onto the basis vectors of $\mathcal{H}$.

In the third step the probabilistic structure of the theory is apparent: The expected payoff function is an average reward each player would receive if the game was repeated many times.

As already mentioned in the preceeding paragraph, the initial state of the quantum game may be an entangled state, so that the game is actually played in a basis of entangled states. The operators $\hat{J}$ and $\hat{J}^\dagger$ are essentially basis transformations between the classical product state basis and the quantum entangled state basis.

This description may appear fairly technical but it suits very well for an experimental realization of a *two player quantum game*. Imagine that the two players are supplied with a photonic qubit (instead of a piece of paper or a coin) on which they can "write down" their choice of strategy. The three stages can then be implemented using the schematic setup shown in Fig.2.4. The two qubit gates $\hat{J}$ and $\hat{J}^\dagger$

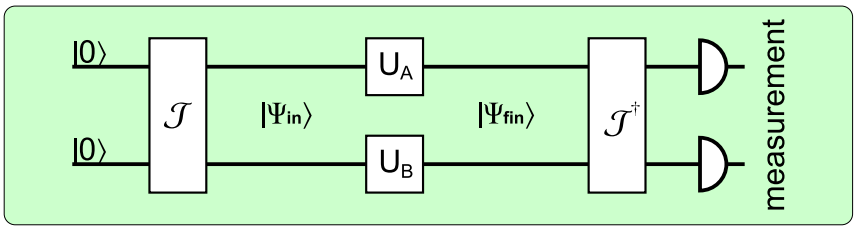

Figure 2.4: Setup for a two player quantum game.

and the single qubit gates $\hat{U}_A$ and $\hat{U}_B$ are discussed in the following paragraph for a classically well known game, comparing classical and quantum solution concepts.

Prisoner's Dilemma

Two gangsters, ***A****lice* and ***B****ob*, have been arrested on suspicion of having commited a crime. Awaiting their trial they are put in separate rooms for questioning with no possibility to communicate with one another. If one of them defects and confesses to the police while the other keeps silent he will be treated as a principal witness, exempted from punishment, and the other will be sent to prison for five years. In case both suspects cooperate against the police, i.e. they both remain silent, they will get away with a two year jail sentence. However, if they both defect and blame each other, the police will have enough evidence to send both of them down for four years.

The Prisoner's Dilemma is a non-zero sum two player static game of complete information [44]. The two players, ***A****lice* (A) & ***B****ob* (B), can independently decide whether they want to ***C****ooperate* (C) or ***D****efect* (D). Depending on their respective decisions, the players obtain a certain payoff, which provides a quantitative measure of their personal preferences. The payoffs given in table 2.5 can be understood as number of years of freedom the players will enjoy in the five years lying ahead of them.

To find the solution of the game and forecast how the two players will behave, we consider the solution concepts presented in the preceeding paragraphs. Rational reasoning will lead Alice ($s_A = \hat{C}, \hat{D}$) to defect if Bob cooperates because it gives a better payoff (five instead of three). If Bob defects, Alice will choose to defect as well, since her payoff becomes one instead of zero and therefore defection is a dominant strategy. Since the game is symmetric, the same applies to Bob. Thus, mutual defection, $\hat{D} \otimes \hat{D}$, constitutes a unique Nash equilibrium and is the solution of the classical Prisoner's dilemma. However, this solution is not Pareto optimal, since both players would benefit more from mutual cooperation, $\hat{C} \otimes \hat{C}$. The players face a dilemma because there is a conflict between the Nash equilibrium and the Pareto optimal outcome. By rational reasoning they are lead to choose the dominant

		Alice	
		C	D
Bob	C	(3,3)	(0,5)
	D	(5,0)	(1,1)

Figure 2.5: Payoff matrix in the Prisoner's Dilemma. The first entry in the parenthesis denotes Bob's payoff, the second entry Alice's payoff.

strategy, defection, although mutual cooperation would make both better off, i.e. receiving a higher payoff (three instead of one).

But to overcome their "rational" instinct towards selfishness is not the only way how cooperation can arise. The players can also escape the dilemma by using quantum strategies and entanglement.

The initial state of the classical game is a vector in the tensor product space spanned by the basis states $|CC\rangle$, $|CD\rangle$, $|DC\rangle$, $|DD\rangle$. To be able to play the quantum version of the game, we will transform the classical initial state into an entangled state in $\mathcal{H}$. The unitary entangling operator $\hat{J}$ is symmetric (for interchange of the players) for fair games and known to both players. It is shown in [43] that the entangling operator can be written as $\hat{J} = \frac{1}{\sqrt{2}}(\hat{C} \otimes \hat{C} + i\hat{D} \otimes \hat{D})$, if one requires the classical game to be contained in the quantum version[21].

Applying the entangling operator to the classical basis states then yields the four entangled basis states:

$$|\psi_{CC}\rangle = \hat{J}|CC\rangle = (|CC\rangle + i|DD\rangle)/\sqrt{2} \tag{2.18}$$

$$|\psi_{CD}\rangle = \hat{J}|CD\rangle = (|CD\rangle - i|DC\rangle)/\sqrt{2} \tag{2.19}$$

$$|\psi_{DC}\rangle = \hat{J}|DC\rangle = (|DC\rangle - i|CD\rangle)/\sqrt{2} \tag{2.20}$$

$$|\psi_{DD}\rangle = \hat{J}|DD\rangle = (|DD\rangle + i|CC\rangle)/\sqrt{2}. \tag{2.21}$$

The entangling operator is chosen such that the matrix representation of the classical strategies remains unchanged for $|\psi_{CC}\rangle$ being the initial state of the quantum game.

In the second step, Alice and Bob can manipulate their qubits by applying unitary operators $\hat{U}_A$ and $\hat{U}_B$ chosen from a subset of all unitary 2×2 matrices. These operators represent local transformations acting exclusively on the qubits in Alice's

[21] i.e. $\hat{J}$ has to commute with the direct product of any pair of classical moves.

and Bob's possession, respectively. The operators $\hat{C} = \begin{pmatrix} 1 & 0 \\ 0 & 1 \end{pmatrix}$ and $\hat{D} = \begin{pmatrix} 0 & 1 \\ -1 & 0 \end{pmatrix}$ acting on the players respective qubit, $|\psi_{A,B}\rangle = a|C\rangle + b|D\rangle$, are associated with the strategies 'cooperate' and 'defect' respectively and correspond to the identity and a spin flip.

After having executed their operations, they forward their qubits for the final measurement which determines their payoff, where the final state of the game prior to detection is given by [43]:

$$|\psi_{fin}\rangle = \hat{J}^{\dagger}(\hat{U}_A \otimes \hat{U}_B)\hat{J}|CC\rangle \tag{2.22}$$

The disentangling gate $\hat{J}^{\dagger}$, applied prior to the measurement on the final state, corresponds to a transformation of the basis of the entangled states (2.18-2.21), back into the basis of the classical product states. Then, the expectation values of Alice's and Bob's payoffs are:

$$\langle \$_i \rangle = P_{CC,i}|\langle\psi_{fin}|CC\rangle|^2 + P_{CD,i}|\langle\psi_{fin}|CD\rangle|^2 + P_{DC,i}|\langle\psi_{fin}|DC\rangle|^2 + P_{DD,i}|\langle\psi_{fin}|DD\rangle|^2 \tag{2.23}$$

where $P_{uv,i}$ for $u, v = C, D$ and $i = A, B$ are Alice's and Bob's entries in the payoff matrix.

For computation of the final state and the payoff functions, several subsets of allowed unitary operations, $\hat{U}_i$, can be considered as the strategic space:

One-parameter set of local unitary operations This set contains essentially all local rotations

$$\hat{U}(\theta) = \begin{pmatrix} \cos\frac{\theta}{2} & \sin\frac{\theta}{2} \\ -\sin\frac{\theta}{2} & \cos\frac{\theta}{2} \end{pmatrix} \tag{2.24}$$

for $\theta \in [0, \pi]$, e.g. $\hat{U}(0) = \hat{C}$ and $\hat{U}(\pi) = \hat{D}$ [44].

This situation is equivalent to the Prisoner's Dilemma with mixed strategies (classical probabilities $p = \cos^2\frac{\theta}{2}$ for $\hat{C}$ and $1-p = \sin^2\frac{\theta}{2}$ for $\hat{D}$). Again one obtains the unique Nash equilibrium for mutual defection $\hat{D} \otimes \hat{D}$ which is not Pareto optimal and therefore not efficient.

Two-parameter set of local unitary operations For this (still restricted) set of quantum strategies the operators take the form

$$\hat{U}(\theta, \phi) = \begin{pmatrix} e^{i\phi}\cos\frac{\theta}{2} & \sin\frac{\theta}{2} \\ -\sin\frac{\theta}{2} & e^{-i\phi}\cos\frac{\theta}{2} \end{pmatrix} \tag{2.25}$$

for $\theta \in [0, \pi]$ and $\phi \in [0, \frac{\pi}{2}]$, e.g. $\hat{U}(0, 0) = \hat{C}$ and $\hat{U}(\pi, 0) = \hat{D}$ [44].

With this set of operators one finds a new unique Pareto optimal Nash equilibrium, $\hat{Q} \otimes \hat{Q}$, i.e. both players choose to play

$$\hat{Q} = \hat{U}(0, \frac{\pi}{2}) = \begin{pmatrix} i & 0 \\ 0 & -i \end{pmatrix} \tag{2.26}$$

This is the only acceptable solution of the game[22], giving a payoff $\$_A(Q, Q) = \$_B(Q, Q) = 3$. By enlarging the set of allowed strategies mutual defection ceases to be an equilibrium solution, instead a new solution emerges for which the dilemma has disappeared!

One may object that the police will not allow the gangsters to use quantum strategies and entanglement and hence it is a change of the rules of the game that is not very likely to happen. However, only allowing the players to get an entangled initial state does not make a difference to the classical game, because as long as the prisoners are not able to use quantum strategies they will not be able to make use of this extra resource. On the contrary if the players in the classical as well as the quantum game are constraint to the same set of (quantum) strategies the input state determines if the game is classical or quantum. Hence neither the input state nor quantum strategies alone constitute a fundamental change of the classical game. In the classical prisoner's dilemma as it is presented in 2.2.3 you may still argue that the suspects lawyers will try to make the most of the situation by all means and as long as the police is not aware of the prisoners being able to use quantum strategies they won't realize that Alice and Bob will have a benefit of an entangled initial state.

Set of general local unitary operations The full range of pure quantum strategies includes every $\hat{U} \in SU(2)$. This set of allowed strategies contains the previously discussed sets as subsets. The operators may be written as [49]

$$\hat{U}(\theta, \alpha, \beta) = \begin{pmatrix} e^{i\alpha} \cos\frac{\theta}{2} & ie^{i\beta} \sin\frac{\theta}{2} \\ ie^{i\beta} \sin\frac{\theta}{2} & e^{-i\alpha} \cos\frac{\theta}{2} \end{pmatrix} \tag{2.27}$$

for $\theta \in [0, \pi]$ and $\alpha, \beta \in [-\pi, \pi]$, e.g. $\hat{U}(0, 0, 0) = \hat{C}$ and $\hat{U}(\pi, 0, \frac{3\pi}{2}) = \hat{D}$.

As a consequence of this further enlargment of the strategic space, the Pareto optimal unique Nash equilibrium from the two-parameter set, $\hat{Q}$, is no Nash equilibrium solution anymore because now every strategy of a player has a counter strategy of his opponent, giving the opponent the maximum payoff while the player is left with the minimum payoff. For example, for any operation $\hat{U}_B(\theta, \alpha, \beta)$ of Bob there

[22] It is not required to have a *maximally* entangled state to reach the Pareto optimal Nash equilibrium! In the partially entangled case, there is a critical value of entanglement above which the quantum strategy $\hat{Q}$ instead of the classically dominant strategy $\hat{D}$ gives a maximal payoff. [48]

exists an optimal answer of Alice $\hat{D}\hat{U}_A(\theta, -\alpha, \frac{\pi}{2} - \beta)$, i.e. "undoing" Bob's move and then defecting, such that she gets the maximum payoff $\$_A(\hat{U}_A, \hat{U}_B) = 5$ while Bob is left with $\$_B(\hat{U}_A, \hat{U}_B) = 0$. The game being symmetric, Bob can improve his payoff by changing his strategy to the optimal counter strategy for Alice's operation. Hence, there is no pair of strategies $(\hat{U}_A, \hat{U}_B)$ leading to an equilibrium solution!

But there remain Nash equilibria in *mixed* operations which are more efficient than the classical outcome, $\$_i(\hat{D}, \hat{D}) = 1$. In mixed operations each player selects a particular operation from the set of allowed operations with a certain classical probability, p_A^i, p_B^j:

$$|\psi_{fin}\rangle = \sum_{i,j} p_A^i p_B^j \hat{J}^\dagger (\hat{U}_A^i \otimes \hat{U}_B^j) \hat{J} |CC\rangle \tag{2.28}$$

with $p_A^i, p_B^j \in [0, 1]$, $\sum_i p_A^i = \sum_j p_B^j = 1$.

One can find multiple Nash equilibria which consist of pairs of mutually optimal answers $\hat{U}_A^{(1)}$, $\hat{U}_A^{(2)}$ and $\hat{U}_B^{(1)}$, $\hat{U}_B^{(2)}$[23], played with equal probabilities $p_A^{(1)} = p_A^{(2)} = p_B^{(1)} = p_B^{(2)} = \frac{1}{2}$.

$\hat{U}_B^{(i)}$ is Bob's optimal answer if Alice plays $\hat{U}_A^{(j)}$ for $i = j$, providing Bob with the maximum payoff of five and Alice with the minimum of zero, while the payoffs are reversed for $i \neq j$. The expectation value of the payoffs for each player then is the average, $\overline{\$}_A = \overline{\$}_B = 2.5$. In this case the (mixed) Nash equilibrium payoff is below that of mutual cooperation. We still have a conflict between the Nash equilibrium and the Pareto optimal outcome, but at least we have an improvement over the classical Nash equilibrium result of mutual defection.

However, there is a continuous set of Nash equilibria[24] and it is not obvious which one the players will realize or whether a Nash equilibrium will be played at all. The issue of multiple equilibria for the prisoner's dilemma is resolved by the gametheoretical concept of the "*focal point effect*" [1]:

In a game with more than one equilibrium, anything that attracts the players attention towards one of the equilibria will make them all expect it and hence realize it. A focal equilibrium has some property that distinguishes it from all other equilibria; consider for example the following situation [50]: You arrange to meet with someone on the platform of a railway station. By the time you get there you realize that the platform is crowded and (infinitely) long. However, at some point on the platform you can see a huge tree. Where will you meet? - At the tree! Even

[23] E.g. $\hat{U}_A^{(1)} = \hat{C} = \begin{pmatrix} 1 & 0 \\ 0 & 1 \end{pmatrix}, \hat{U}_A^{(2)} = -Q = \begin{pmatrix} -i & 0 \\ 0 & i \end{pmatrix}, \hat{U}_B^{(1)} = \hat{D} = \begin{pmatrix} 0 & 1 \\ -1 & 0 \end{pmatrix}, \hat{U}_B^{(2)} = DQ = \begin{pmatrix} 0 & -i \\ -i & 0 \end{pmatrix}$

[24] $\hat{U}_A^{(1)}(\theta, \alpha, \beta), \hat{U}_A^{(2)}(\theta, \frac{\pi}{2} + \alpha, \frac{\pi}{2} + \beta)$ and $\hat{U}_B^{(1)}(\pi - \theta, \frac{\pi}{2} + \beta, \alpha), \hat{U}_B^{(2)}(\pi - \theta, \pi + \beta, \frac{\pi}{2} + \alpha)$ for arbitrary θ, α and β played with equal probability by Alice and Bob respectively.

if this position of the platform might not be better or worse than any other, the tree is the only thing that attracts attention.

In our case this isolated *focal equilibrium* which is different from all other Nash equilibria is the one where the initial state is mapped on the maximally mixed state. For this set of strategies the case where the two players are choosing randomly (with probability 1/2) between the two classical strategies, $\hat{C}$ and $\hat{D}$, is in fact the focal equilibrium. Only this strategy, where every base state will be realized with probability 1/4, is equal to its equilibrium in optimal counterstrategies, and therefore is the solution of the game. It turns out that by maximally enlarging the strategic space, a completely classical strategy becomes the solution of the quantum game! However, this surprising result does not mean that the game is classical again, because the solution is actually a consequence of the presence of quantum strategies eliminating other (classical) strategies, which were superior for the restricted sets.

The expected payoffs the players will receive are $\overline{\$}_A = \overline{\$}_B = 2.25$, while for all other strategies both players are ambivalent between the continuous set of symmetric equilibria. This focal equilibrium again is not Pareto optimal, but more efficient than the classical outcome. Note that *the actual achievable payoff in such a game depends on the set of allowed strategies!*

The scheme presented in the preceeding paragraphs applies not only to the prisoner's dilemma, but to any two player binary choice symmetric game. Some other examples of such classical games and their applications are given in the appendix A.2.

2.3 Optics

In this section I will cover the necessary theoretical concepts of linear as well as non-linear optics, which are indispensable for building a highly efficient source for entangled photon pairs. It is essential to calculate how to set up the source to optimize the collection of down-converted photon pairs as explained in the following chapter. A necessary treatment of Gaussian beam parameters needed for this calculation is hence presented. Furthermore, the non-linear process of parametric down conversion with a classical pump field for the generation of entangled photons is introduced.

2.3.1 Parameters of Gaussian Beams

In this section, the most important parameters of Gaussian beams are reviewed [51, 52], and it is shown how they can be manipulated using paraxial optical elements. The optical wave equation and its solution are given in A.2. Solving the (paraxial) wave equation (A.1), one obtains the beam intensity

$$I(x,y,z) = \tilde{u}\tilde{u}^* \propto e^{\frac{-ikr^2}{2}(\frac{1}{\tilde{q}(z)}-\frac{1}{\tilde{q}^*(z)})} \propto e^{\frac{-2r^2}{\mathtt{w}^2}}, \tag{2.29}$$

showing a Gaussian dependence on r (Fig. 2.6).

The transverse scale of the beam defined by the spot size (s. A.2) gives the distance $r = \mathtt{w}(z)$ from the axis of propagation at point z where the intensity has fallen off to $1/e^2$, i.e. the amplitude to $1/e$, compared to the axial value at $r = 0$.

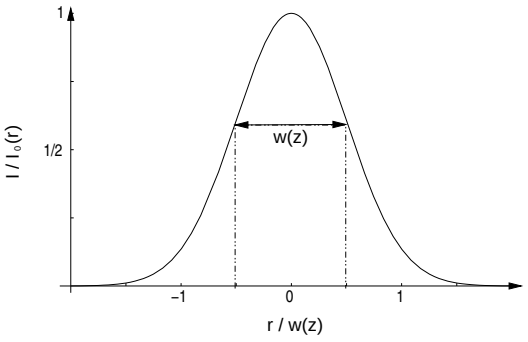

Figure 2.6: Intensity profile of a Gaussian beam.

The field pattern of a lowest order Gaussian beam (Fig. 2.7) is entirely characterized by the wavelength λ in the medium and the beam waist $\mathtt{w}_0$, which is defined as the spot size at $z = z_0 = 0$. There, the reference plane has infinite curvature R_0. The *propagation law* in free space takes the form

$$\tilde{q}(z) = \tilde{q}_0 + z = z + iz_R \quad , \tag{2.30}$$

where the Rayleigh range z_R describes how rapidly a Gaussian beam expands due to diffraction as it propagates. The radius of curvature R (s. A.2), the spot size $\mathtt{w}$

and the complex beam parameter $\tilde{q}(z)$ at any plane z are related via

$$\frac{1}{\tilde{q}(z)} = \frac{1}{R(z)} - i\frac{\lambda}{\pi \mathtt{w}^2(z)} \quad . \tag{2.31}$$

Hence for $\tilde{q}_0$, z_R and $\mathtt{w}_0$ holds the relation

$$\tilde{q}_0 = i\frac{\pi \mathtt{w}_0^2}{\lambda} = iz_R \quad . \tag{2.32}$$

All important beam parameters can be expressed in terms of the waist spot size $\mathtt{w}_0$ and the wavelength λ:

$$\mathtt{w}(z) = \mathtt{w}_0\sqrt{1 + \left(\frac{z}{z_R}\right)^2} \tag{2.33}$$

$$R(z) = z(1 + \left(\frac{z_R}{z}\right)^2) \tag{2.34}$$

$$z_R = \frac{\pi \mathtt{w}_0^2}{\lambda} \quad . \tag{2.35}$$

Equation (2.35) fixes the Rayleigh range z_R at the distance from the waist where the beam has increased its diameter by a factor of $\sqrt{2}$, i.e. doubled its aera. Furthermore it follows that the smaller the waist gets, the more rapidly the beam expands due to diffraction. The Rayleigh range separates the near-field (Fresnel) and the far field (Fraunhofer) region, where the beam size expands linearly with distance. For $z \gg z_R$, the relation between the waist and the spot size becomes $\mathtt{w}(z) \approx \frac{\mathtt{w}_0 z}{z_R} = \frac{\lambda z}{\pi \mathtt{w}_0}$. Defining the beam divergence (i.e. the (half) angular spread) by the diameter at the radial distance where the optical field amplitude has dropped by $1/e$, one determines the asymptotic angle (Fig. 2.7):

$$\theta_{div} = \lim_{z\to\infty} \frac{\mathtt{w}(z)}{z} = \frac{\lambda}{\pi \mathtt{w}_0} \tag{2.36}$$

The Gaussian-spherical wave solution (A.7) of the paraxial wave equation describes the properties of a freely propagating TEM_{00} Gaussian mode[25].

ABCD Matrices

Gaussian beams are not only be the eigenfunctions of free space but also of general paraxial systems (for the paraxial approximation, s. A.2). In geometric optics,

[25] lowest order Transverse Electric and Magnetic mode

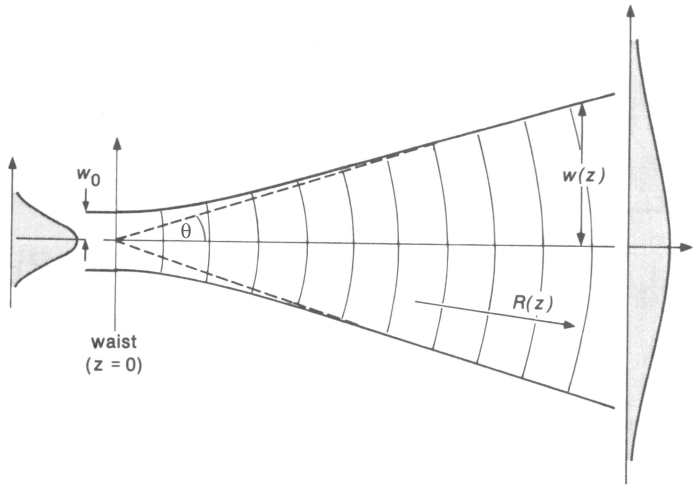

Figure 2.7: Lowest order Gaussian beam diverging away from its waist [51].

a ray transmitted or reflected by optical elements, such as lenses and mirrors, is characterized by its radial and angular displacement with respect to the optical axis of the element. Within the paraxial approximation, the beam parameters of the incident and the outgoing beam are connected with a linear transformation. In the matrix formulation of geometric optics (s.[51],[52]), a given optical element is completely characterized (within the paraxial ray approximation) by the ray- or ABCD matrix. The matrix elements A,B,C,D contain the paraxial focussing properties of the optical element. An array of paraxial elements is handled by multiplying the individual ABCD matrices in reverse order.

For a spherical wavefront with radius of curvature $R_{in}(z)$ passing through an arbitrary paraxial system which is specified by its ABCD matrix, the emerging wavefront will still be spherical and its radius of curvature, $R_{out}(z)$, can be calculated for a given ray matrix.

Using the reduced parameter $\hat{R}(z) = R(z)/n(z)$, the complex beam parameter $\tilde{q}$ becomes

$$\frac{1}{\hat{q}} = \frac{n}{\tilde{q}} = \frac{1}{\hat{R}} - i\frac{\lambda_{vac}}{\pi \mathtt{w}^2}, \tag{2.37}$$

where $\lambda_{vac} = \lambda(z)/n(z)$ is the wavelength in the vacuum, and $\lambda(z)$, $n(z)$ the local wavelength and index of refraction, respectively. The complex Gaussian beam parameter is defined in this way to obtain the ABCD-law, describing how Gaussian beams propagate through an arbitrary paraxial optical system. Hence, $\tilde{q}$ can be transformed by exactly the same law as applied to the radius of curvature R for a spherical wave using only geometric optics.

The **ABCD law of Gaussian beam propagation** connecting in- and output

complex beam parameters reads

$$\hat{q}_{out} = \frac{A\hat{q}_{in} + B}{C\hat{q}_{in} + D}. \tag{2.38}$$

This Gaussian beam transformation rule gives a simple and complete description of how a beam propagates through (multiple) paraxial elements if their ABCD matrices are known. A *material with index of refraction n*, length L and surfaces normal to the direction of beam propagation is characterized by the matrix:

$$\begin{pmatrix} 1 & L/n \\ 0 & 1 \end{pmatrix}. \tag{2.39}$$

From the law of geometric optics for a *thin lens*, the ABCD marix writes

$$\begin{pmatrix} 1 & 0 \\ -1/f & 1 \end{pmatrix}. \tag{2.40}$$

The reflection of a *spherical (concave) mirror* of radius of curvature R, i.e. focal length $f = R/2$, is given by

$$\begin{pmatrix} 1 & 0 \\ -2/R & 1 \end{pmatrix}. \tag{2.41}$$

2.3.2 Spontaneous Parametric Down Conversion

An interaction of electromagnetic fields with matter will always cause electrical dipoles to align with some preferred direction in space, which corresponds to a (change of the) macroscopic polarisation of the crystal

$$\vec{P} = \varepsilon_0 \, (\chi^{(1)}_{lin} \, \vec{E} + \sum_{i=x,y,z} \chi^{(2)}_{ijk} \, E_j \, E_k \vec{e_i} + \dots). \tag{2.42}$$

The first term describes all linear effects (e.g. dispersion and refraction), while the second term contains contributions from three-wave mixing and parametric fluorescence. As the second order susceptibility $\chi^{(2)}_{ijk}$[26] is about ten orders of magnitude smaller than the first order $\chi^{(1)}_{lin} \approx 1$, non-linear effects are negligible for weak fields in linear media. However, for a field in special media exhibiting a strong nonlinearity, the polarization does not only depend linearly on the field strength anymore. For strong light fields in such media non-linear contributions then have to be taken into account, according to the symmetry of the lattice structure[27].

[26] The second order susceptibility is a non-linear tensor for which the convention to sum over homonymous indices applies.

[27] For parametric fluorescence to occur, the lattice of the crystal must not contain centers of inversion.

In a crystal with non-linear properties, in our case Beta-Barium Borate (BBO), with a small probability a high energetic photon splits up into two lower energetic daughter photons. Beta-Barium Borat ($\beta - BB_2O_4$) is a negative uniaxial crystal, which means that along the optical axis, the ordinary index of refraction n_0 is higher than the extraordinary index n_e[28].

For the generation of polarization entangled photon pairs I will only consider the effect of spontaneous parametric down conversion (SPDC), which describes the classically forbidden spontaneous decay of a pump beam photon into so called signal and idler beam photons. This process has to occur in a non-linear environment to simultaneously conserve energy and momentum for the decay of a massless particle. A single atom in the vacuum would therefore suffice for the decay to take place, but only in a non-linear crystal it is possible that the generated photons are emitted in different directions as a result of the different indices of refraction. Therefore, the interaction of the incident pump field with the crystal polarization leading to this decay can be described by a Hamiltonian containing only non-linear contributions to the polarization. In first order perturbation theory it is then possible to calculate the state of the fluorescence modes after some interaction time T_C, which turns out to contain only a vacuum- and a two photon contribution [54]. The interaction time corresponds to the coherence time of the pump field and was in our case $T_C \approx 17$ ns (corresponding to a coherence length of 5 m [53]).

In this calculation, one has to distinguish two phase-matching conditions for the wave vectors of the signal ($\vec{k_s}$), the idler ($\vec{k_i}$) and the pump photon ($\vec{k_p}$): In type-I parametric fluorescence the two photons generated from an extraordinary polarized pump beam have ordinary polarization relative to the optical axis. For type-II fluorescence, one photon is ordinary polarized and the other extraordinary. In the following I will consider type-II fluorescence, because only for this case one obtains polarization entangled photon pairs directly from the decay process [55]. Except from this polarization correlation of the two photons created in the decay process of a pump photon, they are furthermore correlated by the conservation of energy and momentum [56]:

$$\omega_p = \omega_s + \omega_i \tag{2.43}$$

$$\vec{k_p} = \vec{k_s} + \vec{k_i}. \tag{2.44}$$

Note that these conditions also contain the time-energy correlations of the generated photons.

For type-II phase-matching, signal and idler photons with equal wavelength are consequently emitted in two cones, the ordinary and the extraordinary polarized one [55]. The opening angle of the cones depends on the angle between the optical axis of the crystal and the pump beam, as well as the indices of refraction which are

[28] Their wavelength dependence is described by the Sellmeier equations [53].

different for ordinary and extraordinary polarized photons. For an increasing angle, the two cones tilt towards the pump beam, and at some point they will overlap, as shown for the non collinear case in figure 2.8.

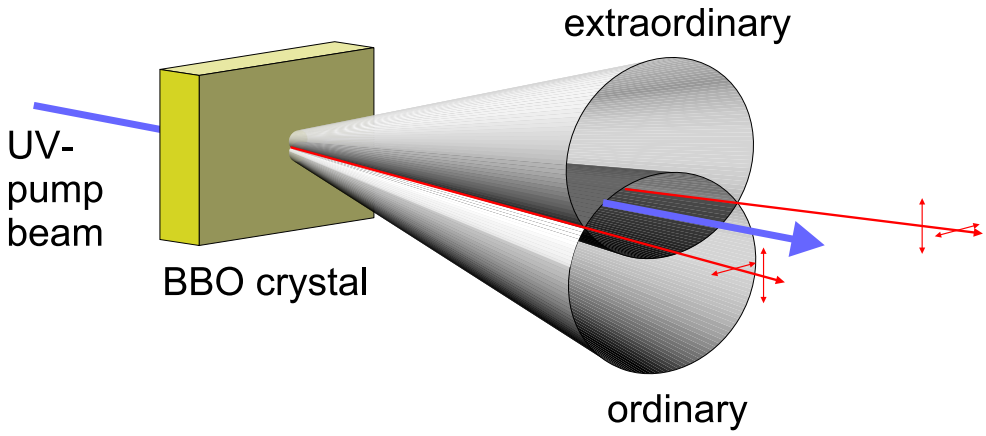

Figure 2.8: Emission cones of typ II parametric down conversion in the degenerate case.

As momentum has to be conserved, the two photons of one pair are always emitted on diametrically opposed sides of the pump beam outside the crystal. The photons which are emitted along the two intersections do not carry any individual polarization, it is only known that their polarizations are orthogonal. Therefore, a photon pair created from a vertically polarized pump photon in the crystal emerging from the intersection points is in an entangled state [55]:

$$|\psi\rangle = (|HV\rangle + e^{i\varphi}|VH\rangle)/\sqrt{2} \tag{2.45}$$

The relative phase φ between the two terms represents the birefringence in the non-linear crystal, and can be adjusted as explained in 3.1.

For my experiment, it was furthermore necessary that down converted photons from the intersection points of two cones with the same wavelength $\lambda_s + \lambda_i = 2\lambda_p$ are collected. Only in this case - called *non-collinear degenerate down conversion* - the photons can be prepared as indistinguishable, which is decisive in our case.

Spontaneous parametric down conversion is currently the most common method to generate entangled photon pairs [57, 53] as well as multiphoton states [58, 59]. No other method, e.g. atomic cascade decays, seems to be capable of producing as many entangled photon pairs as it was achieved with parametric down conversion in non-linear crystals.

3 Implementation

Contents

The implementation of the prisoner's dilemma as a quantum game has already been sketched in 2.2.3. In this chapter I will describe how the necessary one- and two-qubit quantum logic gates shown in the schematic quantum network of figure 2.4 can experimentally be realized for pairs of photonic qubits.

In section 3.1 it is described how a highly efficient and compact pair-photon source was set up to prepare the entangled initial state of the game given in section 2.2.3. The implementation of the player's strategies as manipulations of the photon's polarization is outlined in section 3.2. It is shown how classical as well as quantum strategies are realized in the actual experiment. To finally be able to determine the player's payoffs, it will be necessary to identify all four Bell states with linear optical elements. How a complete Bell state analysis is achieved for the first time and its importance for quantum information processing applications is discussed in section 3.3.

3.1 Initial State Preparation

This section describes how the initial state needed for the quantum version of the prisoner's dilemma given in equation (2.18) can be prepared. Since the states described in (2.18-2.21) form a complete basis like the Bell states do, there always exists a transformation between the two sets (s. section 3.2). Hence, it suffices to initially produce one of the four Bell states and then transform it into the desired initial state of the game, $|\psi_{CC}\rangle = (|CC\rangle + i|DD\rangle)/\sqrt{2}$. We will associate the state $|C\rangle$ with the state of a horizontally polarized photon $|H\rangle$, and $|D\rangle$ with a vertically polarized photon $|V\rangle$.

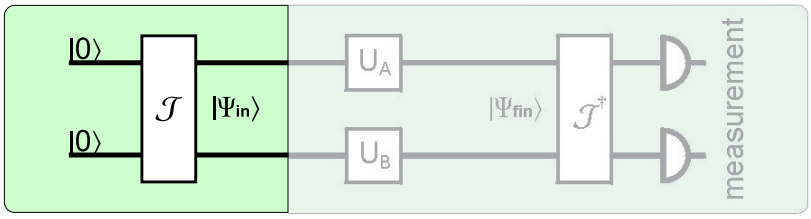

Figure 3.1: Initial State Preparation

The aim in this part of the experiment was to set up a *compact*, *highly efficient*, *non-collinear degenerate type-II* spontaneous parametric down conversion source of entangled photon pairs to prepare the initial state needed for the quantum version of the prisoner's dilemma.

For experiments on foundations of quantum mechanics [19, 27] and the implementation of quantum information processing tasks, a large number of entangled photon pairs is required. It has already been mentioned (s. 2.3.2) that spontaneous parametric down conversion is the most successful method in this respect, but still it takes place with a probability of about 10^{-10} and only scales linearly with pump power. Therefore, it is important to optimize the collection efficiency to be able to perform experiments with reasonable counting statistics. Here, it should be demonstrated that efficient coupling of downconverted photon pairs into single-mode optical fibers is possible, with a compact, simplified setup, yielding countrates comparable with highest ones previously achieved [57].

In the following it will be shown how to build a source which fulfills the above conditions and supplies us with the entangled two-photon state needed for the implementation of the prisoner's dilemma (s. fig. 3.1).

3.1.1 Guidelines

In principle all you need to generate entangled photon pairs from spontaneous parametric fluorescence is a non-linear crystal, a powerful laser to pump the crystal and

some collection optics.

In my setup a two millimeter long BBO crystal provided the non-linear environment for spontaneous parametric down conversion to occur, because BBO shows a high non-linear coefficient while being transparent in the ultraviolet. The crystal had an anti-reflective coating for the pump wavelength (351nm) as well as for the wavelength of the downconverted photons we want to collect (702nm). To realize the previously introduced non-collinear degenerate down conversion (2.3.2) for 702nm photons which have just twice of the pump wavelength, the BBO crystal has to be cut and aligned such that the optical axis and the direction of the pump beam include an angle of $\theta_p = 49.7°$.

For this case the surfaces of the cones intersect under 90° (s. fig. 3.2) and hence the origin of a photon cannot be inferred from the spectral distribution in both directions, which is also advantageous for efficient coupling into single-mode fibers [57]. The emission directions (θ, ϕ) of the downconversion photons can be calculated from their wavelength (for a fixed pump wavelength) and one obtains, that the opening angle between the intersections is just 6°. To obtain the desired spatially separated but otherwise indistinguishable entangled photon pairs, the collection optics images the crossing points of the cones into fibers.

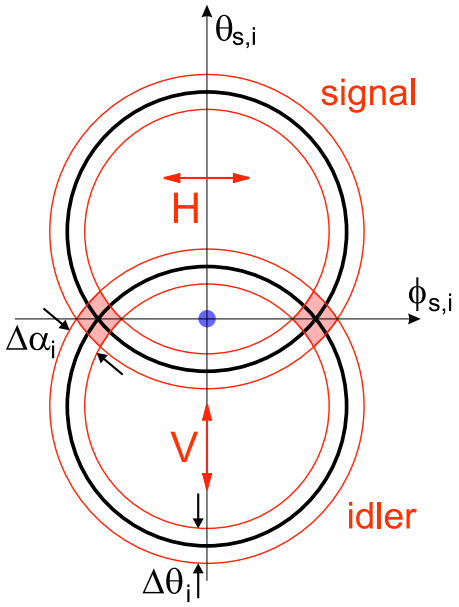

Figure 3.2: Spectral angular distribution, $\Delta\theta$, of fluorescence photons.

To pump the non-linear crystal, an Argon ion laser running at 351nm[1] was used, providing up to 700 mW pump power. For single (longitudinal) mode selection, an etalon, consisting of an uncoated plane-parallel, transparent silica plate, was placed inside the cavity. Ultraviolet pump light is used, because it allows to produce entangled photon pairs which are very efficiently detectable with Silicon avalanche photodiodes. The pump beam is vertically polarized. With respect to the downconversion source that means extraordinary polarized, i.e. the polarization vector lies in the plane spanned by direction of propagation and the optical axis of the BBO crystal[2].

To select a clean and well defined spatial mode from the intersection points, it is desirable to couple the down converted light into single mode fibers. Due to

[1] This corresponds to the transition between two configurations of the $3s^2 3p^4 (^3P) 4p$ electron.
[2] Consequently, the ordinary polarization vector is perpendicular to the optical axis

the small core diameter and the profile of the index of refraction of such an optical fiber, light can only propagate in the TEM_{00}-mode. To couple light efficiently into the fiber, its modes have to match these boundary conditions. Therefore, the collection of straylight from the crystal or other luminous sources is strongly suppressed. Coupling into a fiber also allows more freedom in designing the experimental setup, because the photons can be transported to any desired position on the optical table for further processing. Of course, one has to take care that the different phase shifts and polarization rotations the photons accumulate when travelling through a fiber are properly compensated for.

The pump beam is supplied by an Ar^+-laser, which is a rather expensive device to purchase as well as to maintain. In the last two years, however, the first blue diodelasers became commercially available, and as soon as they offer sufficient pump power in single mode operation together with a well defined spatial mode, they will allow to build cheap and more compact sources for entangled photon pairs. As a first step towards taking entangled photon pairs out of a laboratory, it was thus the aim to set up the source as compact as possible, so that one would just have to replace the big Ar^+-laser by a tiny diode to fit the whole assembly in a portable box.

3.1.2 Design of the setup

To achieve optimal collection of entangled photon pairs, one has to maximize the overlap of the two-photon-mode emitted from the crystal and the two single field mode profiles of the single-mode fibers. The idea is to geometrically match, i.e. overlap, the pumped region in the non-linear crystal optimally to the target field mode defined by the Gaussian mode of the fiber with which the photons should be collected. The mode matching condition for the waist ω_p and ω_0 of the pump- and fluorescence mode to allow an optimal observation of the down conversion process then reads

$$\omega_p \stackrel{!}{=} \mathtt{w}_0 \quad . \tag{3.1}$$

One of the main problems to efficiently collect the downconverted photons is their broad spectral width. This setup was designed to collect photons from the intersection points with a spectral width (FWHM) of $\Delta\lambda = 4$ nm centered around twice the pump wavelength, i.e. $\lambda = 702$ nm. Depending on the spectral width of the fluorescence photons one can determine the beam waist of the fluorescence mode to which the pump beam has to be focussed. Because of the wavelength dependence of the flare angles of the emission cones and the axial symmetry of the intersection points, photons in the range of $\lambda \pm \Delta\lambda/2$ will propagate from their point of origin into a solid angle of $\theta \pm \Delta\theta/2$, as shown in figure 3.2. The angular spread of the

downconverted photons for a given spectral width can be determined from [57]

$$\Delta\theta = \frac{d\theta}{d\lambda}\Delta\lambda \quad . \tag{3.2}$$

The differential angular distribution of parametric fluorescence $\frac{d\theta}{d\lambda}$ was studied in [53]. For $\theta_p = 49.7°$ and $\lambda = 702$ nm, the dispersion properties of BBO lead to $\frac{d\theta}{d\lambda} = 0.055°/\text{nm}$, yielding $\Delta\theta = 0.22°$. Assuming that the fluorescence mode is Gaussian (for axially symmetric intersection points), it is then possible to calculate the divergence θ_{div} of the target mode [57]:

$$\theta_{div} = \frac{\Delta\theta}{\sqrt{2ln2}} = 0.186° \tag{3.3}$$

From equation (2.36), the waist of the fluorescence mode is found to be $\mathtt{w}_0 = 68.5\mu$m. The corresponding Rayleigh range is $z_R = 2.1$ cm. This target mode has then to be mapped into single-mode fibers[3] with a waist of 2.28μm. To increase the countrates a little further it might be advantageous to choose a slightly lower divergence, resulting in a bigger Gaussian beam waist. In this way it is possible to compensate for additional divergence due to the angular distribution in the pump beam [57].

With the parameters introduced in section 2.3 and a given focal length of the coupling optics, one can now calculate where the optical components have to be placed in order to obtain a fluorescence mode as specified in the above paragraph.

First of all, a telescope was set up to focus the pump beam down from 1mm to 68.5μm in the BBO crystal (s. fig. 3.3). The waist of the Argon ion laser beam was taken to be 544 μm (corresponding to a Rayleigh range of 2.65 m for the Argon ion beam) and the distance from the waist to the first lens of the telescope is approximately 4 m, determined in a previous experiment [53]. In the ABCD matrix formalism (equations (2.30) & (2.38)-(2.40)), the distance between the first lens and the desired waist was calculated for different combinations of lenses (i.e. different focal lengths). I obtained the minimal value of 42.2 cm (distance between the lenses: 14.8 cm; distance between the second lens and the waist: 27.4 cm) for a focal length of 100 mm and 40 mm, respectively. The lenses were set up accordingly and the crystal was placed at the position of the waist.

Secondly, the distance from the crystal to the single-mode fiber was calculated analogously for an aspheric lens[4] with a focal length of 11 mm. As a result, the fiber couplers (containing the lens in a thread) and the fiber connector were placed

[3] FC Single Mode Patch Cable with a cutoff wavelength of 630 nm from Thorlabs (P1-3224-FC)

[4] Because spherical aberration is dominant (over diffraction) for spherical lenses, it is typically not possible to achive spot sizes small enough to couple into a fiber. Aspherical lenses are corrected such that spherical aberration is eliminated. The local spot size is then only limited by diffraction.

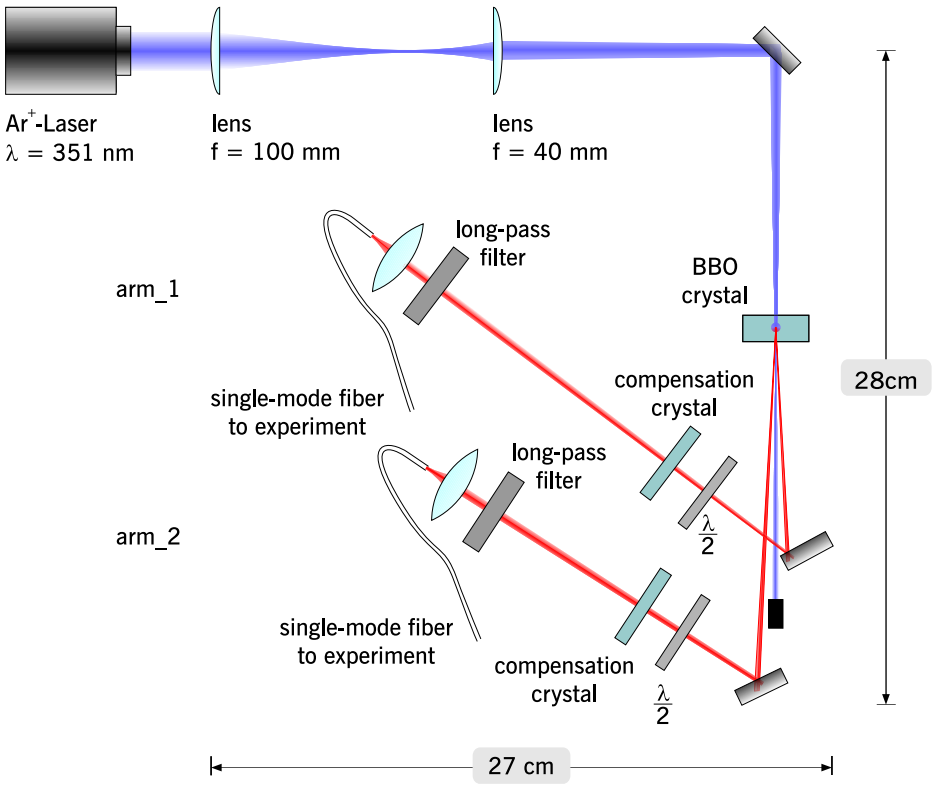

Figure 3.3: Down Conversion Setup

34.1 cm behind the crystal. The position of the lens in the coupler was adjusted such that the light from a 702 nm laser diode sent "backwards" through fiber and lens matches the calculated target mode in the crystal. This can be verified by measuring the spot size at three positions, from which the waist and its position can be determined. In the final stages of the experiment it turned out that the distance between the lens and the fiber is crucial for efficient coupling into a single-mode fiber. Therefore, our method might not have been precise enough to achive the optimal count rates. This could be improved by using translation mounts, where the separation of lens and fiber can be adjusted more accurately, compared to the mount used (i.e. a screw thread).

The exact orientation of the optical axis of the BBO crystal is found by placing 702nm interference filters in front of the fiber couplers and then tilting the crystal until the countrate of photons from down conversion is maximal. For first alignment of the fiber couplers, the diode laser was adjusted such that it travels along the same path the downconversion photons on the intersections of the cones including an angle

of 6° are supposed to take.

The setup was then folded by introducing mirrors as shown in figure 3.3 to get it as compact as possible. Note that this setup is a simplification of previous ones, because the four degrees of freedom needed for optimizing the alignment of the fiber couplers were available through the mirrors and tilting of the fibercoupler mounting. In prior experiments, a more space consuming array of translation stages was used.

3.1.3 Beam walk-off and state preparation

With the collection optics described above one can very efficiently observe photons created in the focal region of the single mode fiber. To increase the total count rate, one might think about using longer non-linear crystals. However, the story is not that easy due to the birefringence in the non-linear material, which causes a longitudinal and a transversal walk-off.

Transverse beam walk-off describes the refraction of extraordinary polarized photons relative to ordinary polarized ones in birefringent media. A beam of ordinary polarized photons will therefore be widened by about 70μm per millimeter crystal length [53] and have an elliptical profile, while the shape of the extraordinary beam remains unchanged. A longer crystal will therefore not necessarilly result in higher photon count rates due to the transverse beam walk-off which can significantly affect the coupling efficiency[5]. A model describing the influence of the crystal length on the collection efficiency of entangled photon pairs created in parametric down conversion is presented in [60].

Photons will also suffer longitudinal walk-off. Inside a BBO crystal horizontal and vertical polarized photons travel with different speeds of light, since the index of refraction, n, for the **e**xtraordinary polarization (V) is smaller than for **o**rdinary polarization (H), $n_e = 1.55 < n_o = 1.66$. An ordinary and an extraordinary polarized photon at 702 nm will be separated by 200 fs per millimeter crystal length. This temporal separation has to be compared with the coherence time of the downconverted photons which is determined by the bandwidth collected. For the case that two interfering beams are obtained from a single beam, the relation between coherence time $\Delta\tau_c$ and bandwidth $\Delta\lambda$ is given by [61]:

$$\Delta\tau_c \Delta\nu \sim 1 \tag{3.4}$$

$$\text{with} \quad \Delta\nu = \frac{c\Delta\lambda}{\lambda^2} \tag{3.5}$$

For a spectral width of $\Delta\lambda = 4$ nm, the coherence time of the two downconverted photons becomes $\Delta\tau_c \sim 411$ fs.

If the temporal separation exceeds the coherence time of the downconverted photon pair it is possible to distinguish both photons leaving the crystal on the

[5] In [60] a coupling efficiency of 18% for 3 mm and 29% for 1 mm crystal length was experimentally obtained.

basis of their correlation in time and direction of propagation. Then, we cannot speak of a polarization entangled state anymore because it is possible to determine the polarization of one photon by its arrival time relative to the other.

As photons are created with equal probability (normalized to pump photon density) at any position in the crystal, photon pairs generated close to the input plane of the crystal will suffer a different longitudinal walk-off than pairs created close to the output plane. The longer the crystal, the bigger the spread in arrival time of two simultaneously created photons with different polarizations relative to each other.

To compensate for these beam walk-off effects, a $\lambda/2$-plate and a compensation crystal was placed in both arms behind the crystal. The $\lambda/2$-plate is set to 45°, so that ordinary polarization is transformed into extraordinary polarization and vice versa. The same walk off effects as in the pumped BBO crystal then happen in the compensation crystals, which are BBO crystals as well but only half as long as the pumped downconversion crystal. Accordingly, due to the transverse walk-off, the ordinary polarized beam will lie at the center of the widened elliptical extraordinary beam after having passed the compensation crystal. The temporal displacement will be compensated on average as well, because photon pairs created close to the input plane will be shifted in phase just by the opposite amount of pairs created close to the output plane.

After the compensation of walk-off effects, the photon pair produced in the BBO crystal can be described by the state (2.45). The relative phase shift φ can be adjusted by tilting one of the compensation crystals. That way it is possible to set φ to any desired value, for example $\varphi = 0$, resulting in $|\psi\rangle = (|HV\rangle + |VH\rangle)/\sqrt{2}$, and $\varphi = \pi$, yielding $|\psi\rangle = (|HV\rangle - |VH\rangle)/\sqrt{2}$, two of the four Bell states. With a supplementary half waveplate transforming H into V polarization and vice versa in one arm it is also possible to produce the other two Bell states.

Therefore, I conclude that this setup is well suited to produce the necessary entangled initial state of the quantum game. The achieved coupling efficiencies, photon pair detection rates and entanglement properties of the detected pairs are presented in section 4.1.

3.2 Local Unitary Operations

The next step for the realization of the game is the implementation of the player's local unitary operation on their respective photon as shown in figure 3.4. As described in the preceeding section the players can be supplied with any of the four Bell states from the downconversion source. This state then has to be transformed into the initial state $|\psi_{CC}\rangle$ given in (2.18). Afterwards, Alice and Bob have to be able to manipulate the photon's polarization according to their choice of strategy. To determine which state is realized after the polarization manipulations were performed, one has to be able to identify any of the four possible final states (2.18)-(2.21) corresponding to the entries of the payoff matrix. Therefore, it is necessary to transform the state into the Bell basis and perform a complete Bell state analysis to determine the payoffs. The first realization of such a deterministic Bell state analyzer with linear optical elements will be presented in the following section.

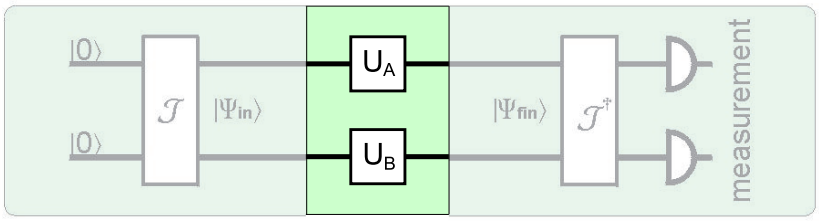

Figure 3.4: Local unitary operations

In general a transformation acting on one qubit can be described by a unitary 2×2 matrix:

$$U = \begin{pmatrix} a & b \\ c & d \end{pmatrix} \quad . \tag{3.6}$$

Accordingly the basis states $|0\rangle$ and $|1\rangle$ are transformed into $U|0\rangle = a|0\rangle + b|1\rangle$ and $U|1\rangle = c|0\rangle + d|1\rangle$. In the following, I will represent the components needed to perform the transformations by unitary operators[6]. In quantum mechanics the evolution of (superposition) states (s. section 2.1) is assumed to be *unitary* if the state is not interacting with the environment such that the superposition decays into an incoherent mixture (decoherence). This is of course an idealization, because it assumes that no particles are lost (non-absorbing components) [62], but shows how a strategy can be implemented.

[6]Unitary operations can be seen as the analogue of rotations in the Euclidean space for such transformations in a Hilbert space.

In the following, states of the two-qubit system will be represented as vectors

$$|\psi\rangle = k|H_A H_B\rangle + l|H_A V_B\rangle + m|V_A H_B\rangle + n|V_A V_B\rangle = \begin{pmatrix} k \\ l \\ m \\ n \end{pmatrix} \quad , \tag{3.7}$$

with A denoting Alice's and B Bob's path. As Alice and Bob will only be able to perform single particle operations on the state $|\psi\rangle$, the overall transformation matrix has to be factorizable into a tensor product of single qubit operations.

First of all, the Bell state from the down conversion source has to be transformed into the initial state $|\psi_{CC}\rangle$ (2.18) by single particle operations. The set of all four Bell states can bijectively be mapped onto the set of the $|\psi_{ij}\rangle$ (2.18-2.21) by applying for example the operator $T^\dagger = T_A^\dagger \otimes T_B^\dagger$, which can be factorized into $T_A^\dagger = \begin{pmatrix} 1 & 0 \\ 0 & i \end{pmatrix}$ und $T_B^\dagger = \begin{pmatrix} 1 & 0 \\ 0 & 1 \end{pmatrix}$. Operating $T^\dagger$ on the Bell state then yields:

$$T^\dagger|\Phi^+\rangle = \quad T^\dagger \begin{pmatrix} 1 \\ 0 \\ 0 \\ 1 \end{pmatrix} = \begin{pmatrix} 1 \\ 0 \\ 0 \\ i \end{pmatrix} \quad = |\Psi_{CC}\rangle \tag{3.8}$$

$$T^\dagger|\Phi^-\rangle = \quad T^\dagger \begin{pmatrix} 1 \\ 0 \\ 0 \\ -1 \end{pmatrix} = (-i) \begin{pmatrix} i \\ 0 \\ 0 \\ 1 \end{pmatrix} \quad = (-i)|\Psi_{DD}\rangle \tag{3.9}$$

$$T^\dagger|\Psi^+\rangle = \quad T^\dagger \begin{pmatrix} 0 \\ 1 \\ 1 \\ 0 \end{pmatrix} = i \begin{pmatrix} 0 \\ -i \\ 1 \\ 0 \end{pmatrix} \quad = i|\Psi_{DC}\rangle \tag{3.10}$$

$$T^\dagger|\Psi^-\rangle = \quad T^\dagger \begin{pmatrix} 0 \\ 1 \\ -1 \\ 0 \end{pmatrix} = \begin{pmatrix} 0 \\ 1 \\ -i \\ 0 \end{pmatrix} \quad = |\Psi_{CD}\rangle \quad . \tag{3.11}$$

After the operations U_A and U_B of the players are performed, the resulting state can then be transformed back into the corresponding Bell states modulo some global phase. The inverse transformation $|\Psi_{ij}\rangle \xrightarrow{T} |BS\rangle$ is simply given by the hermitian conjugate of the transformation $|BS\rangle \xrightarrow{T^\dagger} |\Psi_{ij}\rangle$ as $T^{-1} = T^\dagger$.

In our implementation of a two-player quantum game, the application of the players operations $(U_A \otimes U_B)$ to the initial state of the game $|\Psi_{CC}\rangle$ (s. figure 3.5)

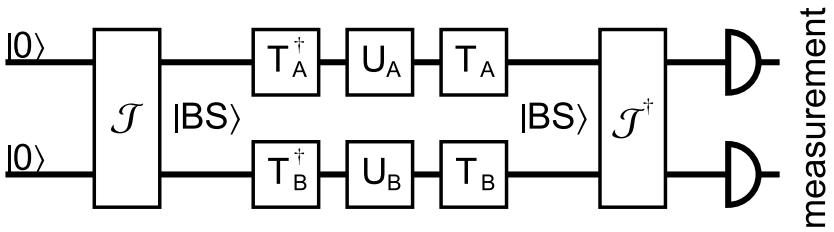

Figure 3.5: Local state transformations

is hence realized as operating with the transformation $T(U_A \otimes U_B)T^\dagger$ on the Bell state $|\Phi^+\rangle$, obtained from the down conversion source.

The operations T, U_A, U_B and $T^\dagger$ can be experimentally realized with a combination of two $\lambda/4$- and a $\lambda/2$-waveplate as shown in figure 3.6. With this array of waveplates it is possible to perform any arbitrary manipulation of the photon's polarization. A $\lambda/2$-waveplate and a $\lambda/4$-waveplate can be represented by

$$U_{\lambda/2}(\varphi) = \begin{pmatrix} \cos^2(\varphi) - \sin^2(\varphi) & \sin(2\varphi) \\ \sin(2\varphi) & -\cos^2(\varphi) + \sin^2(\varphi) \end{pmatrix} \quad \text{and} \tag{3.12}$$

$$U_{\lambda/4}(\varphi) = \begin{pmatrix} \cos^2(\varphi) - i\sin^2(\varphi) & (\frac{1}{2} + \frac{i}{2})\sin(2\varphi) \\ (\frac{1}{2} + \frac{i}{2})\sin(2\varphi) & -i\cos^2(\varphi) + \sin^2(\varphi) \end{pmatrix} \quad , \tag{3.13}$$

where φ is the angular setting of the waveplate. Therefore we are not restricted to implementing all three single qubit operations ($T_i^\dagger$, U_i and T_i) separately, i.e. one by one. Instead, it is possible to find some angular setting of the waveplates corresponding to any joint operation $T(U_A \otimes U_B)T^\dagger$ performing the state transformations as well as any of the players moves.

For example it is possible to implement the classical operations C and D as well as the quantum strategy Q (**??**) in this way. For C and Q, Alice and Bob both have to apply the operations $U_{\lambda/4}(0°)U_{\lambda/2}(0°)U_{\lambda/4}(0°)$ and $U_{\lambda/4}(90°)U_{\lambda/2}(90°)U_{\lambda/4}(0°)$, respectively, i.e. set the waveplates to the angles given in parenthesis. Since the single qubit operations T_A and T_B for the state transformation are different for Alice and Bob, it happens that for some strategies Alice will have to apply a different polarization manipulation than Bob, even though they want to perform the same move. For example, this is the case for an implementation of the strategy D, where Alice has to set her waveplates according to $U_{\lambda/4}(0°)U_{\lambda/2}(135°)U_{\lambda/4}(0°)$, while Bob has to perform $U_{\lambda/4}(0°)U_{\lambda/2}(45°)U_{\lambda/4}(90°)$ to defect as well[7].

[7]This issue could be resolved by a change of basis (for example choosing H and $\frac{1}{\sqrt{i}}V$ as a basis in both Hilbert spaces instead of H and V). Then, however, the matrix representation of strategy D would contain complex entries. Nevertheless, I will stay with notation used so far, to not confuse classical and quantum strategies.

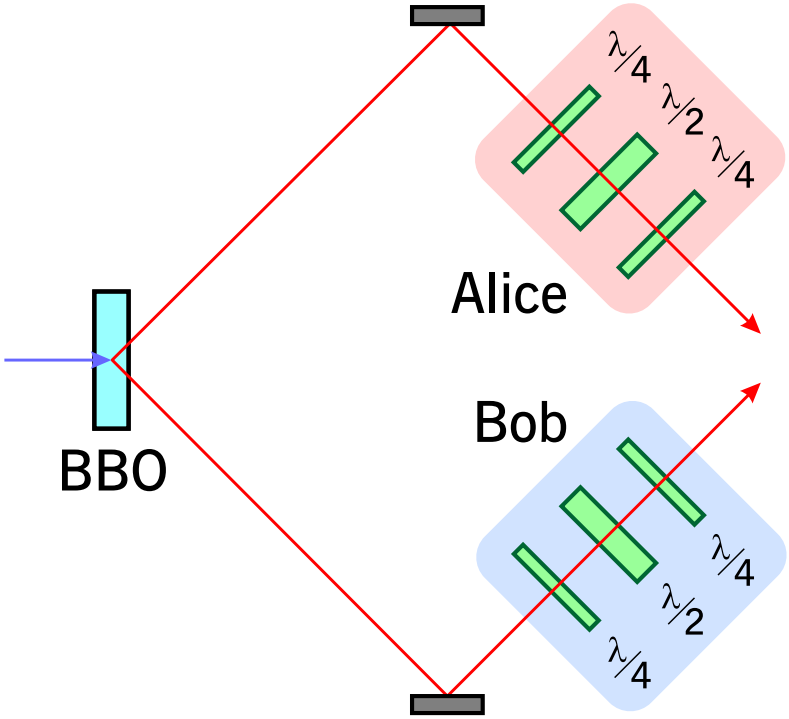

Figure 3.6: Schematic implementation of local unitary operations to perform basis-transformations and certain strategies for Alice and Bob on the state of the game.

As shown for the transformations (3.8-3.11) any of the four Bell states corresponds to one of the possible final states of the game (2.18-2.21). Hence it suffices to be able to identify all four Bell states for the payoff determination. Inserting the values given in the payoff matrix (table 2.5), Alice's and Bob's payoff for a given final state $|\psi_{fin}\rangle$ after having performed the operations discussed above, is obtained from

$$\$_A = 3|\langle\phi^+|\psi_{fin}\rangle|^2 + 0|\langle\psi^-|\psi_{fin}\rangle|^2 + 5|\langle\psi^+|\psi_{fin}\rangle|^2 + 1|\langle\phi^-|\psi_{fin}\rangle|^2 \quad (3.14)$$

$$\$_B = 3|\langle\phi^+|\psi_{fin}\rangle|^2 + 5|\langle\psi^-|\psi_{fin}\rangle|^2 + 0|\langle\psi^+|\psi_{fin}\rangle|^2 + 1|\langle\phi^-|\psi_{fin}\rangle|^2 \quad (3.15)$$

To perform the quantum game it finally remains to identify all four possible final states of the game, corresponding to the entries in the payoff matrix. In the following section it is presented how this can be done.

3.3 Complete Bell State Analysis

In the last stage of the game we have to implement the "judge", who determines the players payoffs, i.e. their punishment. Therefore, the final state of the game has to be projected onto the basis vectors of the strategic space corresponding to the four entries in the payoff matrix (s. fig. 2.5). As discussed before (s. section 3.2), we

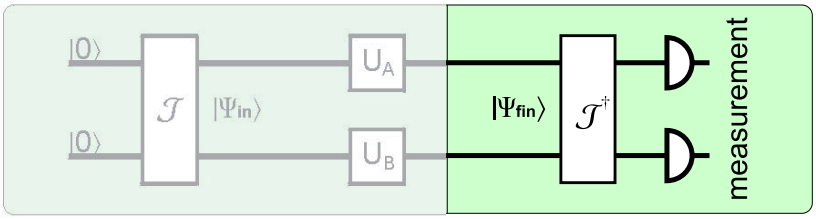

Figure 3.7: Payoff determination.

therefore have to be able to perform a complete Bell state analysis, because every Bell state can be identified with exactly one entry in the payoff matrix.

To be able to perform such a complete Bell measurement, we have to set up a reversible two-qubit gate corresponding to the operator $J^\dagger$ in figure 3.7. For a two-qubit gate, the evolution of one qubit depends on the state of another qubit. The gate has to project an arbitrary combination of input Bell states, prepared by the players, onto a complete set of states, which can unambiguously be identified by a detection signal in the coincidence basis. This could easily be achieved if one would be able to implement a controlled NOT (also called two-qubit exclusive-OR) and a Hadamard gate on the two entangled qubits (s. figure 3.8). A Hadamard gate is a single qubit gate which turns the states $|0\rangle$ and $|1\rangle$ into $(|0\rangle + |1\rangle)/\sqrt{2}$ and $(|0\rangle - |1\rangle)/\sqrt{2}$, respectively. A controlled NOT (c-NOT) is a two-qubit gate where the bit value of the (lower) target qubit is flipped if the (upper) control qubit carries the logical bit value "1", and not flipped if it carries "0", i.e. leaving the control qubit unchanged.

For quantum computation networks, the controlled NOT plays a decisive role because it can be shown [6, 7] that the combination of one-qubit gates and the controlled NOT allows to perform all unitary operations on an arbitrary number of qubits. Therefore, the c-NOT, together with the single-qubit operations is forming a set of *universal* gates. One of the main challenges in quantum information processing to date therefore is the implementation of the gates needed for a universal quantum circuit.

An optical implementation of a deterministic controlled NOT gate could be achieved if a strong non-linear interaction between two photons could be accomplished. However, in currently known optical materials, non-linear processes only

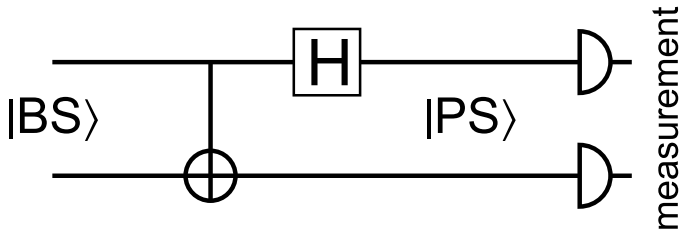

Figure 3.8: 2-Qubit gate consisting of a c-NOT and a Hadamard gate to transform Bell states ($|BS\rangle$) into product states ($|PS\rangle$).

occur with a negligible probability for weak light fields, and hence it is highly improbable that two photons will interact. However, one can try to achieve the experimental implementation of photonic quantum gates involving a c-NOT operation without the requirement of a direct two-photon interaction, using only linear optical elements[8]. An idea published by E. Knill, R. Laflamme and G.J. Milburn (KLM) utilizes auxiliary photons and two-photon interference effects in linear optical networks [8].

To implement a c-NOT gate in form of the operator $J^\dagger$ for the identification of all four Bell states with linear optical elements in my experiment, a somewhat different approach will be followed. Instead of auxiliary photons as in the KLM-scheme, we will use additional degrees of freedom of the two-qubit state in question. Therewith, it will be possible for the first time to experimentally demonstrate how to identify all four polarization Bell states simultaneously in one measurement just using linear optics.

3.3.1 Distinguishability of Bell States

Until now the identification of only *two* of the four polarization Bell states was experimentally demonstrated, for example in the dense coding experiments [13], where the remaining two Bell states give the same detection result. For Bell states entangled in the momentum degree of freedom, an analogous interferometric Bell state analysis has been performed with the same result [63].

For different polarization (or momentum) analysis settings of these interferometric Bell measurements, it is furthermore possible to identify any two Bell states [64, 13]. In this sense, a "complete" Bell state analysis has been performed before, but it only works if one is allowed to conditionally measure at least two pairs in the same given state. However, for the implementation of the prisoner's dilemma as

[8] Linear optical elements are devices which can be described by an at most quadratic Hamiltonian (in the field amplitudes), such as phase shifters, beam splitters, polarizers and mirrors. With linear optical elements it is possible to produce any linear combination of a unitary operation performed on a one-photon input state (i. e. arbitrary unitary maps of creation operators).

well as for other new communication protocols, one has to be able to extract all the information about the state from a single two-qubit system with one setting of the measurement apparatus.

J. Calsamiglia and N. Lütkenhaus showed that it is not possible to perform a von Neumann projection measurement[9] on a maximally entangled basis [65, 4]. They conclude that the four polarization Bell states cannot unambiguously be distinguished using only linear optical elements, and derive an upper bound of 50% probability of success for a Bell measurement if no auxiliary photons and no conditional measurements[10] are allowed for.

The main idea to nevertheless be able to do a complete Bell state analysis with linear optical elements is to make use of entanglement in more than one degree of freedom. In principle, entanglement in a particular degree of freedom is as good as in any other. However, in practice it is most convenient to work with the polarization degree of freedom, because it is easy to control with off-the-shelf optical components and robust against decoherence. For photon pairs generated in the process of parametric downconversion though, entanglement is not restricted to the polarization degree of freedom, but one can also make use of their *energy-time-entanglement*. When the Bell states are embedded in a higher dimensional Hilbert space, we can utilize entanglement in the auxiliary degree of freedom with an additional interferometer.

The supplementary entanglement in the time degree of freedom arises as follows: In section 3.1 two photons from a parametric down conversion source were said to be produced "simultaneously", which means in the sub-picosecond range [66]. The time at which the first photon is emitted is initially uncertain over an interval as long as the coherence time of the pump photon the pair is created from. However, by the point in time when the first photon was emitted, its detection immediatly determines the position of the other within a very small uncertainty, given by the optical bandwidth allowed for the photon, resulting in a narrow (in time) coincidence peak. This can be interpreted as a non-classical correlation in the time (or position) degree of freedom, analogous to the polarization entanglement of a Bell state [67].

The correlation time[11] in our experiment is limited by the bandwidth of the collected downconverted photons given in section 3.1. It is important to notice that the correlation time is independent of the coherence time of the incident pump beam [66, 68]. From the bandwidth of the pump field the coherence time of a pump photon can be calculated, describing the uncertainty in time of this photon, which does not

[9] i.e. a measurement for which every classically distinguishable outcome (a combination of detector clicks) is proportional to a projection on exactly one of the four Bell states.

[10] i. e. measure one photon and afterwards perform operations on the remaining photons depending on the measurement outcome.

[11] By the correlation time conventionally the time delay between the detection of the two photons is described.

affect the relative time delay of signal and idler photon. For our down conversion source, the time interval in which the two photons are produced is exceedingly short ($\tau_C = 411$ fs; calculated in section 3.1) compared to the long coherence time of the pump photon ($T_C \approx 17$ ns; given in section 2.3.2). From this, it follows that the downconverted light has a substantial spread in the emitted wavelength, because the energy of each individual downconverted photon is only imprecisely defined. This connection of the correlation time and the energy of the created photon pair has to be distinguished from the similar relation for the incident pump photon. Because of the relatively small bandwidth of the pump light, the sum of signal and idler photon energy is very well defined, while the time they were generated is only imprecisely known. It is this time-energy correlation we will use in the following to perform a complete Bell state analysis of an EPR-pair from a downconversion source.

This is not a violation of the no-go theorem of Lütkenhaus et al.; it is rather a circumvention, because the theorem doesn't apply to states entangled in more than one degree of freedom.

3.3.2 Embedded Bell state analysis

A setup to actually perform the complete Bell state analysis utilizing the time-energy correlation explained in the section above was suggested by P. G. Kwiat and H. Weinfurter in [5]. It is shown in figure 3.9, where the birefringent elements of the original suggestion are replaced by polarizing beam splitters to delay one polarization relative to the other.

In the following, I will show how the four Bell states are transformed by the linear optical components of the setup, and which detector signals are expected for the different states. As introduced in the preceeding section, I will describe the components by unitary matrices. This is a simplification which will be used only to show how the Bell state analyzer works in principle. Effectively, it is possible for the given setup to compensate for phase shifts between horizontal and vertical polarized photons beforehand by tilting the compensation crystals in the downconversion setup and adjusting the relative path difference of the two interferometer arms accordingly. Generally, the matrix describing an optical element, for example a beam splitter, has to be determined by *measuring* its reflectivity, transmittivity and phase shifts.

Hong-Ou-Mandel interference

Firstly, we will interfere the two qubits of the given Bell state at the 50:50 beam splitter. For the calculation of the state behind the beam splitter I assume that the phase shift between the transmitted and reflected beam after having passed a beam splitter is $\phi = \pi/2$ [62].

In some calculations, it is assumed for simplicity that both polarizations suffer equal phase shifts when passing the beam splitter [64]. This has led to some con-

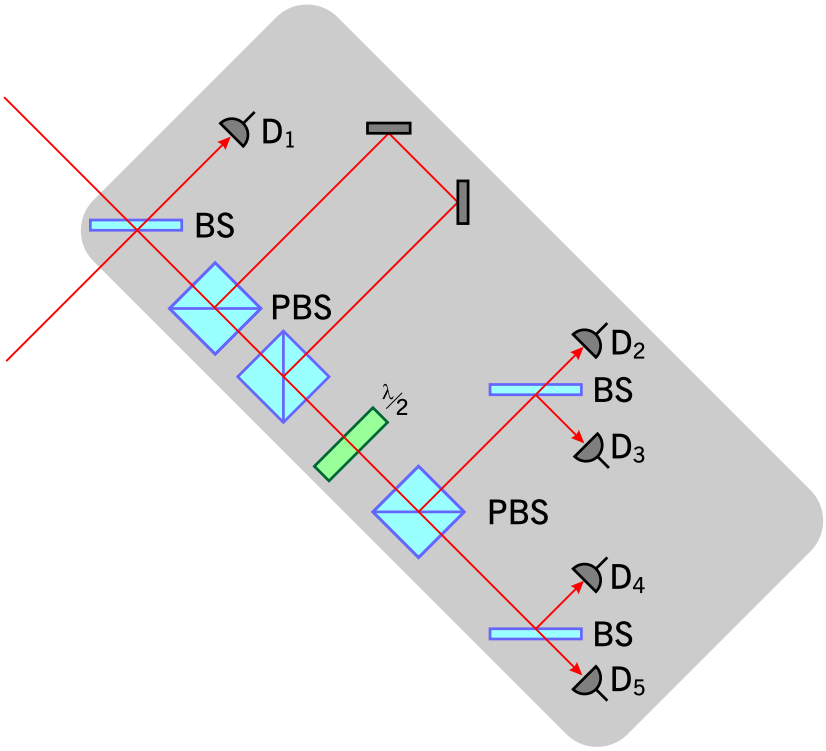

Figure 3.9: Setup for a complete Bell state analysis.

fusion recently, because it is a misleading description of what is actually observed for light in the reflected arm of (some) beam splitters [69]. Generally speaking, the relative phase shift for different polarizations depends on the angle of incidence and the different indices of refraction of the materials the semireflecting layer consists of, which is normally not revealed by the manufacturer. For a correct identification of the Bell states however, it is important to know how polarization is altered when passing a beam splitter. Therefore, I estimated the relative phase shift between horizontal and vertical polarization in the output ports of a beam splitter by shining in $+45°$ polarized light and analyzing in $\pm 45°$ in both output ports. For the reflected arm I observed minimal transmission behind a polarizer set to approximately $+45°$. This means that H and V polarizations must have suffered a relative phase shift of approximately π, disregarding an overall phase factor which all beams have in common, and which is thus not relevant in interferometric setups only sensitive to relative phase. The beam splitter hence transforms $+45°$ polarization of the input beam into $-45°$ polarization of the reflected output beam. For the transmitted arm, I observed minimal transmission behind a polarizer set to approximately $-45°$. Hence the polarization must have been almost unaffected by the beam splitter. These measurements were repeated for different orientations of the

beam splitter, yielding the same result.

In the following, I will therefore assume that the reflected component of a horizontally polarized photon will suffer a phase shift of $-\pi/2$, while for vertical polarization the phase shift is $\pi/2$. In the experiment it is possible to compensate for deviations from these values by tilting the compensation crystals in both arms. A beamsplitter with input modes i and j will hence be represented by the matrix:

$$U_{bs}(i,j) = \frac{1}{\sqrt{2}} \begin{pmatrix} 1 & -i & 0 & 0 \\ -i & 1 & 0 & 0 \\ 0 & 0 & 1 & i \\ 0 & 0 & i & 1 \end{pmatrix} \tag{3.16}$$

I will denote the input modes of the beam splitter by a and b, and the output modes by a' and b' as shown in figure 3.10. Then a photon pair combined on the beam splitter will be transformed according to

$$\begin{pmatrix} Ha' \\ Hb' \\ Va' \\ Vb' \end{pmatrix} = \frac{1}{\sqrt{2}} \begin{pmatrix} 1 & -i & 0 & 0 \\ -i & 1 & 0 & 0 \\ 0 & 0 & 1 & i \\ 0 & 0 & i & 1 \end{pmatrix} \quad \begin{pmatrix} Ha \\ Hb \\ Va \\ Vb \end{pmatrix} \quad . \tag{3.17}$$

To calculate how the two photons forming a Bell state, one in each input mode, superposed on a 50:50 beam splitter, are transformed, we have to write down the complete states – polarization as well as spatial mode – which have to be completely symmetric according to the bosonic nature of the system[12]:

$$\begin{aligned} |\psi^+\rangle &= \frac{1}{4}(|HV\rangle + |VH\rangle)(|ab\rangle + |ab\rangle) \\ |\psi^-\rangle &= \frac{1}{4}(|HV\rangle - |VH\rangle)(|ab\rangle - |ab\rangle) \\ |\phi^+\rangle &= \frac{1}{4}(|HH\rangle + |VV\rangle)(|ab\rangle + |ab\rangle) \\ |\phi^-\rangle &= \frac{1}{4}(|HH\rangle - |VV\rangle)(|ab\rangle + |ab\rangle) \end{aligned}$$

To find out how these states look behind the beamsplitter I apply the operator $U_{bs}(a,b)$ for input modes a and b as defined above and disregarding global phase

[12]This is because now, the particles are not distinguishable anymore by their spatial mode.

shifts:

$$
\begin{aligned}
U_{bs}(a,b)\,|\psi^+\rangle &= \frac{1}{2}(|Ha'\,Vb'\rangle + |Hb'\,Va'\rangle + |Va'\,Hb'\rangle + |Vb'\,Ha'\rangle) \\
U_{bs}(a,b)\,|\psi^-\rangle &= \frac{1}{2}(|Ha'\,Va'\rangle - |Hb'\,Vb'\rangle + |Va'\,Ha'\rangle - |Vb'\,Hb'\rangle) \\
U_{bs}(a,b)\,|\phi^+\rangle &= \frac{1}{2}(|Ha'\,Ha'\rangle - |Hb'\,Hb'\rangle - |Va'\,Va'\rangle - |Vb'\,Vb'\rangle) \\
U_{bs}(a,b)\,|\phi^-\rangle &= \frac{1}{2}(|Ha'\,Ha'\rangle + |Hb'\,Hb'\rangle + |Va'\,Va'\rangle + |Vb'\,Vb'\rangle)
\end{aligned}
$$

Obviously, only for the $|\psi^+\rangle$ as input state one will observe the two photons in different spatial output modes a' and b'. For all other Bell states, both photons will be found in the same output mode a' or b'. By the detection signal behind the first beam splitter one can therefore distinguish the $|\psi^+\rangle$ from the other three Bell states.

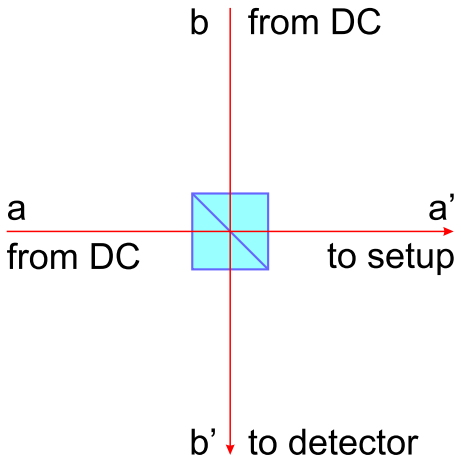

Figure 3.10: Beam splitter: a and b denote the input modes for photons coming from the downconversion, a' and b' denote the output modes. In the experiment a detector will be placed in mode b' directly behind the beamsplitter, while in the other arm further processing is performed.

C. K. Hong, Z. Y. Ou and L. Mandel were the first to discover this interference effect of signal and idler photons created in parametric down conversion [70]. It was demonstrated [71] by increasing the coherence time of the two photons that the interference of detection events behind the beam splitter can be understood as the interference of probability amplitudes of the two photon state and not as interference of individual photons. Later on, this effect was used in many experiments to distinguish between two of the four Bell states [13, 72]. If the two beams from the down conversion source (section 3.1) travelling on two different paths a and b are recombined on a beam splitter, their spatial mode behind the beam splitter and a

polarization measurement (i.e. a polarizing beam splitter and two detectors in at least one of the output arms) in the coincidence basis suffices to identify any two of the four Bell states. Remarkably, this effect *cannot* be used to distinguish between the states of the game given in equations **??**, because the $|\psi_{CD}\rangle$ and $|\psi_{DC}\rangle$ states will result in the same detection signal.

In order to observe this Hong-Ou-Mandel (HOM) effect in an experiment, one has to take care that the two distinguishable input photons are indistinguishable after they have passed the beam splitter.

To optimize this spatial mode matching, two conditions have to be fulfilled: The photons have to travel along the exact same path behind the beam splitter, and their wavefront curvature has to be equal. To optimally overlap the two paths determined by the output fiber couplers behind the downconversion, one needs four degrees of freedom for adjustment. One of the beams is taken as reference and the other can then be adjusted by horizontally and vertically tilting and moving (with translation stages) the coupler in x- and y-directions. A different divergence of the two input modes would also allow to identify the input path of each photon by its wavefront curvature. Therefore it was tried to adjust the beams such that they are both collimated, i.e. the spot size remains unchanged over a distance of approximately five meters. To achieve better control over this important parameter, it might be advantageous to use more accurately adjustable fiber mounts in the future.

Furthermore, the spectra of both photons have to be equal, and it must not be possible to identify them by their polarization. Also the distance between the BBO crystal and the beam splitter has to be made equal to within the correlation length of the down conversion photons, for them to arrive within their correlation time at the beam splitter. For this purpose, one of the output fiber couplers is mounted on a (motorized) translation stage to accurately align the relative path length difference between the two arms.

As long as the relative time delay between the photons arriving at the beam splitter is distinctly bigger than the correlation time, the number of observed coincidences is determined by

$$N_{coinc} = N_{coinc,0}(r^2 + t^2) \quad . \tag{3.18}$$

Therein, $N_{coinc,0}$ is the coincidence rate which is observed without the beam splitter in the beamline, and r and t are the reflectivity and transmittivity for amplitudes, respectively. If the photons arrive at the beam splitter within their correlation time, the coincidence rate is observed to drop down or peak up depending on how the respective Bell state behaves at the beam splitter[13], resulting in the so called

[13]For a first path length alignment independent of the input state one can search for the position of the dip by placing horizontally adjusted polarizers between the fiber coupler and the beam splitter. If two horizontally polarized photons are superposed on the beam splitter, they will show the same behavior as the Bell states.

Hong-Ou-Mandel-dip (for the $|\psi^-\rangle$, $|\phi^+\rangle$ and $|\phi^-\rangle$) or -bump (for the $|\psi^+\rangle$).

In case not all of the above mode matching conditions are fulfilled, or if the reflectivity and transmittivity of the beam splitter are not equal to 50%, the HOM-dip cannot be expected to drop down to zero.

The asymmetric interferometer

Having identified one of the Bell states (the ψ^+) by the observation of HOM-interference, it remains to identify the other three. Note that in the setup shown in figure 3.9 it is only possible to identify the remaining three Bell states in one output port of the beam splitter. Hence, I will in the following only consider one output mode. The events where the two photons are emitted in the other ouput mode will not be recorded as a coincidence, because both photons will hit the same detector, giving a signal which cannot be distinguished from a single-photon event. This is not a loss of universality for the ability to distinguish between all four Bell states, but it will cause not all events to be detected. By building the the same setup in both arms this issue would be resolved, however at the expense of more optical components, detectors and a more complex coincidence logic.

In accordance with the considerations made for the beam splitter in the previous paragraph, I will represent a polarizing beam splitter (PBS) by the unitary operator

$$U_{pbs}(i,j) = \begin{pmatrix} 1 & 0 & 0 & 0 \\ 0 & 1 & 0 & 0 \\ 0 & 0 & 0 & i \\ 0 & 0 & i & 0 \end{pmatrix} \quad . \tag{3.19}$$

Denoting the output modes of a polarizing beam splitter by l and s corresponding to the long and short arm of the asymmetric interferometer shown in figure 3.3, one obtains the states after the photon pair has passed the beam splitter and the two polarizing beam splitters (global phase factors disregarded):

$$\begin{aligned} U_{pbs}(s,l)\, U_{pbs}(a')\, U_{bs}(a,b)\, |\psi^-\rangle &= \frac{1}{2}(|Hs\ Vl\rangle + |Vl\ Hs\rangle) \\ U_{pbs}(s,l)\, U_{pbs}(a')\, U_{bs}(a,b)\, |\phi^+\rangle &= \frac{1}{2}(|Hs\ Hs\rangle + |Vl\ Vl\rangle) \\ U_{pbs}(s,l)\, U_{pbs}(a')\, U_{bs}(a,b)\, |\phi^-\rangle &= \frac{1}{2}(|Hs\ Hs\rangle - |Vl\ Vl\rangle) \end{aligned}$$

For this calculation, the relative phase between horizontally and vertically polarized photons was set to π. In the experiment this relative phase will depend on the path length difference between the long and the short arm of the interferometer. To obtain the states as calculated above, it will be necessary to stabilize the path lenth difference of the interferometer arms at a value according to the phase setting of zero (modulo 2π). For an arbitrary unknown phase (or fluctuations of the phase) it

will not be possible to distinguish between the $|\phi^+\rangle$ and $|\phi^-\rangle$ states.

The polarizing beam splitters separate vertically polarized photons going the long path from horizontally polarized ones going the short path by the time Δt. Hence, a vertically polarized photon will always be delayed with respect to a horizontally polarized photon. In this way it is possible to distinguish the remaining $|\psi^-\rangle$ from the two $|\phi\rangle$-states, because only the $|\psi^-\rangle$ will result in two photons which are separated in time behind the interferometer. For the $|\phi\rangle$-states, the photons will always either both travel the long arm of the interferometer or both the short arm, and hence arrive at the detectors simultaneously in any case. To be able to resolve if two photons arrive simultaneously (i.e. within the tiny jitter of detector signals and the spread in time of signal and idler photon generation) or separated in time, the delay line has to be long enough to electronically distinguish between the two possibilities. In our case the long path will be approximately one meter longer than the short path, corresponding to a separation in time of roughly 3 ns. Accordingly, also the coincidence window has to be set such that the temporally separated events give a different coincidence detection event than simultaneously arriving photons, i.e. it has to be shorter than half of the temporal separation between horizontally and vertically polarized photons.

Identification of $|\phi^+\rangle$ and $|\phi^-\rangle$

The identification of the two $|\psi\rangle$-states as described in the preceeding two paragraphs is a variation of previous implementations of Bell state analyzers (e.g. the one in [13]). In this paragraph it will now be shown how to go beyond these previous experiments, exploiting the new possibilities of the additional time-energy-entanglement.

For the complete Bell measurement, it remains to distinguish between the two $|\phi\rangle$-states. The idea is to analyze the state in the $+45°/-45°$-basis, because then coherence of detection events is restored, and the information about which of the probability amplitudes led to the coincident detection is lost. Therefore, the photons are sent through a $\lambda/2$-waveplate, described by the matrix (3.12), set to 22.5°, transforming horizontal and vertical into $|+45°\rangle = (|H\rangle + |V\rangle)/\sqrt{2}$ and $|-45°\rangle = (|H\rangle - |V\rangle)/\sqrt{2}$ polarization, respectively. In the H/V basis the state behind $\lambda/2$-waveplate then reads:

$$\begin{aligned}
U_{\lambda/2}(22.5°)\, U_{pbs}(s,l)\, U_{pbs}(a')\, U_{bs}(a,b)\, |\phi^+\rangle = \\
\tfrac{1}{4}(|Hs\ Hs\rangle + |Hs\ Vs\rangle + |Vs\ Hs\rangle + |Vs\ Vs\rangle \\
+|Hl\ Hl\rangle - |Hl\ Vl\rangle - |Vl\ Hl\rangle + |Vl\ Vl\rangle) \\
U_{\lambda/2}(22.5°)\, U_{pbs}(s,l)\, U_{pbs}(a')\, U_{bs}(a,b)\, |\phi^-\rangle = \\
\tfrac{1}{4}(|Hs\ Hs\rangle + |Hs\ Vs\rangle + |Vs\ Hs\rangle + |Vs\ Vs\rangle \\
-|Hl\ Hl\rangle + |Hl\ Vl\rangle + |Vl\ Hl\rangle - |Vl\ Vl\rangle)
\end{aligned}$$

For photon pairs generated in parametric down conversion, one has the same probability for such states to be produced at any time within the coherence length, defining the relative separation, within which two photons can still interfere. Consequently, one can separate the temporal degree of freedom, distinguishing between photon pairs having taken the long or the short path, from the polarization degree of freedom. Then, interference of the probability amplitudes for detection events of two photon pairs at different points in time, t and $t + \Delta t$, is observed as long as Δt does not exceed the coherence time of the pump photon from which they originate [67]. Therefore the delay line has to be shorter than the coherence time of the pump field, $\Delta t < T_C$. The upper bound of $T_C \approx 17$ ns for photons from the pump beam used here is in our case clearly longer than the delay line of approximately three nanoseconds.

Polarization analysis with a polarizing beam splitter then yields states being detected at time t in the output ports corresponding to H and V polarization:

$$\begin{aligned} U_{pbs}(a')\, U_{\lambda/2}(22.5^\circ)\, U_{pbs}(s,l)\, U_{pbs}(a')\, U_{bs}(a,b)\, |\phi^+\rangle &= \frac{1}{2}(|H\ H\rangle - |V\ V\rangle)\, |t,\ t\rangle \\ U_{pbs}(a')\, U_{\lambda/2}(22.5^\circ)\, U_{pbs}(s,l)\, U_{pbs}(a')\, U_{bs}(a,b)\, |\phi^-\rangle &= \frac{1}{2}(|H\ V\rangle + |V\ H\rangle)\, |t,\ t\rangle \end{aligned}$$

Finally, we obtain that the $|\phi^+\rangle$ and $|\phi^-\rangle$ behave differently at the polarizing beam splitter after the $\lambda/2$-waveplate. The $|\phi^-\rangle$ will split up at the polarizing beam splitter and hence always lead to a coincidence detection event, while for the $|\phi^+\rangle$ both photons are emitted into the same output port. For comparison a similar calculation for the $|\psi^-\rangle$ leads to

$$\begin{aligned} &U_{pbs}(a')\, U_{\lambda/2}(22.5^\circ)\, U_{pbs}(s,l)\, U_{pbs}(a')\, U_{bs}(a,b)\, |\psi^-\rangle \ = \\ &\frac{1}{4}(|H\ H\rangle - |V\ V\rangle - |H\ V\rangle + |V\ H\rangle)\, |t,\ t+\Delta t\rangle. \end{aligned}$$

To detect the $|\phi^+\rangle$ one has to able to verify both photons emitted into the same output port of the polarizing beam splitter. In principle a detector distinguishing between one and two photons would be the optimal solution. However, such detectors are currently not commercially available for visible light. Since photomultiplier tubes are capable of resolving the photon number for higher energetic light, work is in progress to achieve the same for the low energy regime and hence this might be an option in the future. Also, kryogenic solid-state detectors were reported to be able to resolve photon numbers, but are not available to civil customers commercially. A different approach are the so called (fiber) loop detectors, where a multi-photon state is sent through a fiber loop with an adjustable ratio coupler [73, 74] or an optical switch and a weak coupler [75] connecting the input, the loop and the output to the actual detector. First experiments in this direction where performed demonstrating a proof of principle, but they are not yet in a stage to be used as standard detector

modules. The main problem for this detectors still is the limited one-photon detection efficiency. Instead of these photon number resolving detectors, there is still a conceptionally different methode to realize the identification of the $|\phi^+\rangle$ and $|\phi^-\rangle$ states with the proposed setup, by using an antisymmetric pump beam [76, 77].

However, the simplest technique to register two photons in the same spatial mode is simply to use an additional beam splitter and two detectors instead of one as shown in figure 3.9. If the two photons are leaving the polarizing beam splitter through the same output port, it will be possible in half of the cases to identify one reflected and one transmitted photon in two detectors behind the 50:50 beam splitters. For all other cases the two photons are either both transmitted or both reflected and then absorbed simultaneously by the same detector. Such events are not distinguishable from the detection of single-photon events and will hence not appear in any coincidence statistics. Of course, it would be possible to further increase the number two-photon coincidence detections by using more beam splitters and detectors, but in excess to the unacceptably rising expenses for detectors, the coincidence logic would also become increasingly complex.

To summarize, it is possible to identify all four Bell states and to determine the players payoffs by the detection event observed with the presented setup (s.figure 3.9). But the probability amplitudes of the detection events are found to vary depending on the Bell state to be observed. Not taking the single-photon detection efficiencies into account (which are probably below 40% for the detectors used) one finds that the $|\psi^+\rangle$ has a probability of 100% to arrive at two different detectors, because it is the only Bell state splitting up in the HOM-interferometer. The probability amplitudes for the $|\phi^-\rangle$ after processing suggest that it can be identified with a probability of 50%, which could be increased to 100% by having the same setup in both arms. The $|\psi^-\rangle$ and $|\phi^+\rangle$ have lower probabilities, 37.5% and 25% respectively, for both photons to arrive at different detectors, because of the inability to unambiguously distinguish between one and two photon (Fock) states. A simple improvement of the current setup, requiring only a polarizing beam splitter and an additional detector before detector D1 (s. figure 3.9), would allow to identify the $|\psi^-\rangle$ states with a probability of 75% in total. One can think of further improvements of the same type, however, the gain in detection probability is only possible at the increasing expense of detectors needed.

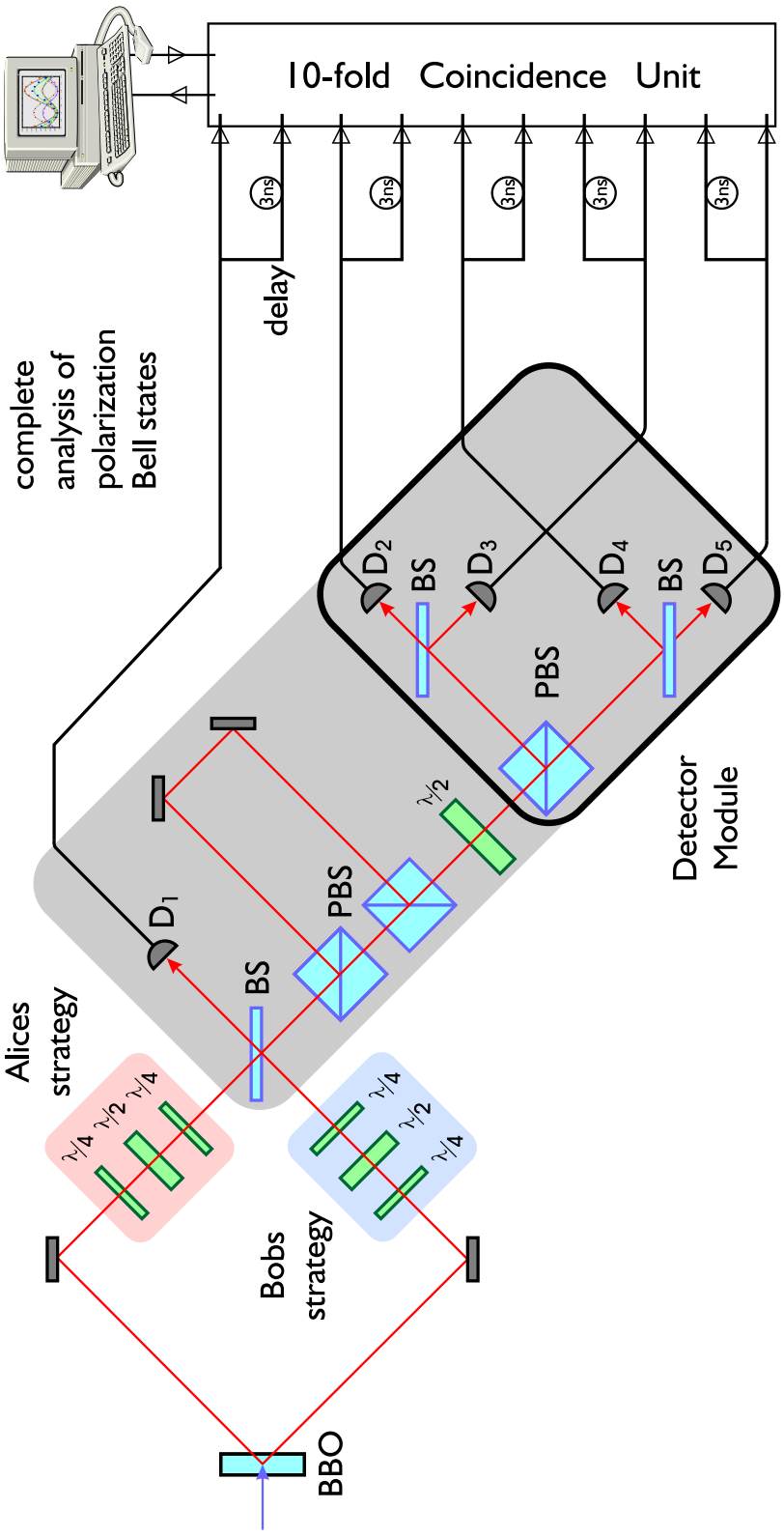

Figure 3.11: Experimental setup

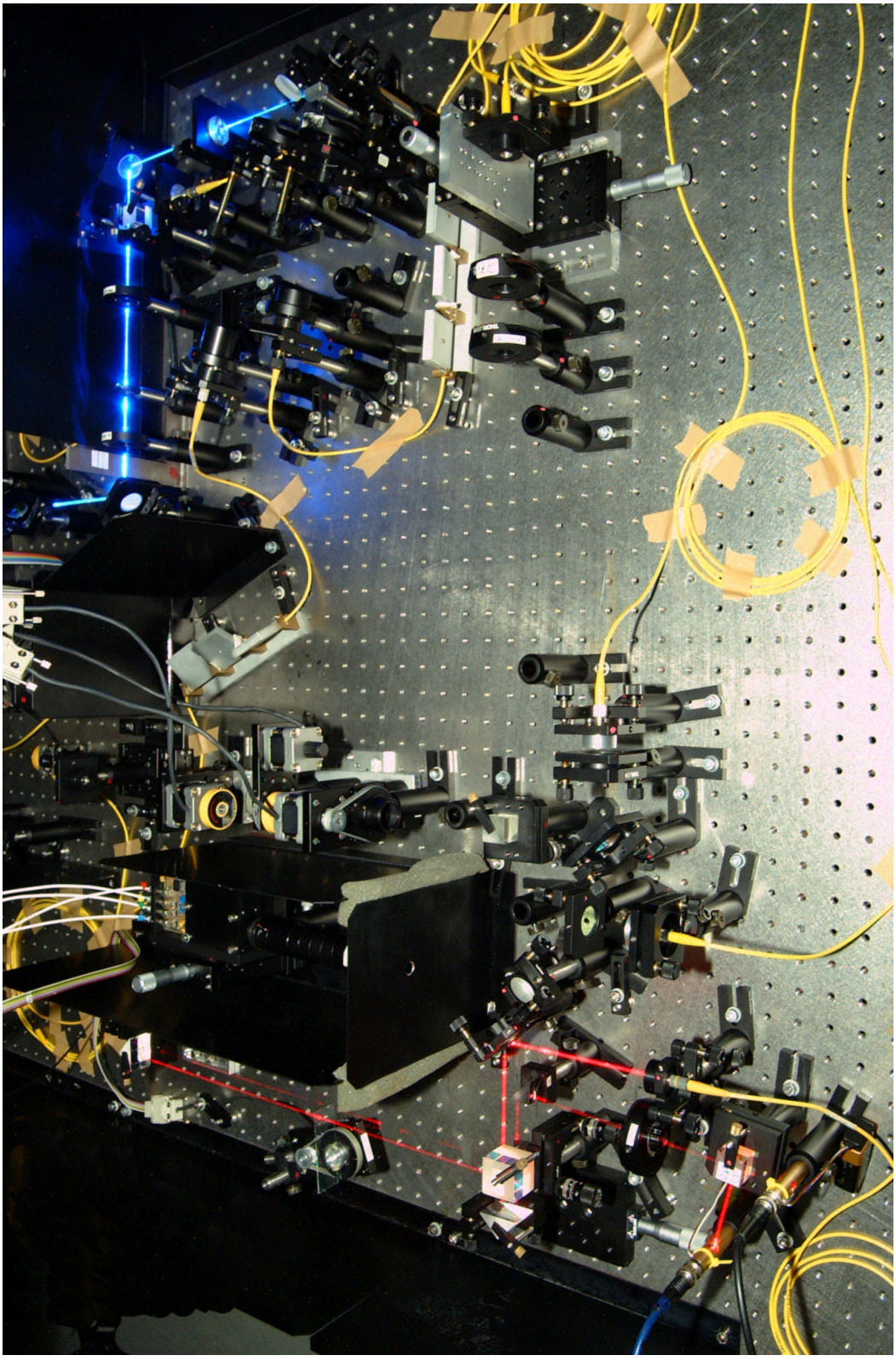

Figure 3.12: Photography of Experimental Setup

4 Experiment

Contents

4.1 Characterization of the Photon Pair Source

As a first step I tried to adjust the setup such that the intersection directions (s. section 3.1) are mapped into the fibers. Using 702 nm interference filters, I aligned the mirrors and fibercouplers such that maximal single and coincidence count rates are obtained. 'Single count rate' denotes the detection rate of one detector registering photons indepently of finding another (downconverted) photon. This rate is expected to show a pronounced maximum in the intersection directions, twice as high as anywhere else on the 702 nm cones, since signal and idler light contributes here. The rate of detecting two photons, one in each collected mode within some coincidence time window set by the experimentator (for the results presented in this section it was set to 21 ns) is then referred to as 'coincidence rate'. From the discussion in section 3.1, this rate is also expected to be maximal in the intersection directions.

With the - in this sense - optimally aligned setup it was possible to produce about *800 photon pairs per milliwatt per second* for the two millimeter long BBO crystal[1]. Typically coincidence/single count rate ratios of about $25 - 27\%$ were obtained. We used (passively quenched) silicon avalanche photodetectors, which have a recharge time of about 1 μs after the detection of a photon event, and hence they show significant saturation effects when the single count rates exceed 100 000 counts per second. In this regime the coincidence count rates don't scale linear with the pump power anymore however, even without actively quenched diodes (having smaller recharge times and therefore lower saturation effects) the source yields coincidence count rates comparable with the brightest cw-sources currently in operation.

The entangled initial state of the game produced in the process of spontaneous parametric down conversion (s. 2.3.2) has to be carried by two photons of the exact same wavelength in order to be indistinguishable as required for the observation of two-photon interference. If their wavelength distribution would be shifted relative to each other, the HOM-interference will not be optimal, because one could identify the input mode of each photon behind the beamsplitter by its wavelength. It turned out that the spectra obtained from the down conversion source aligned for maximal count rates (without the interference filters) were shifted by about 4 nm relative to each other. Hence, the setup was realigned monitoring the wavelength with a grating spectrometer and finally I obtained the spectra shown in figure 4.1. For the detected photons travelling through the spectrometer which were detected in coincidence with a second one in the other arm, the spectral width is determined by a Gaussian fit to data points:

$$(\Delta\lambda)_{exp} = 4.6 \text{ nm} \tag{4.1}$$

[1]This value was obtained after realignment without the interference filters

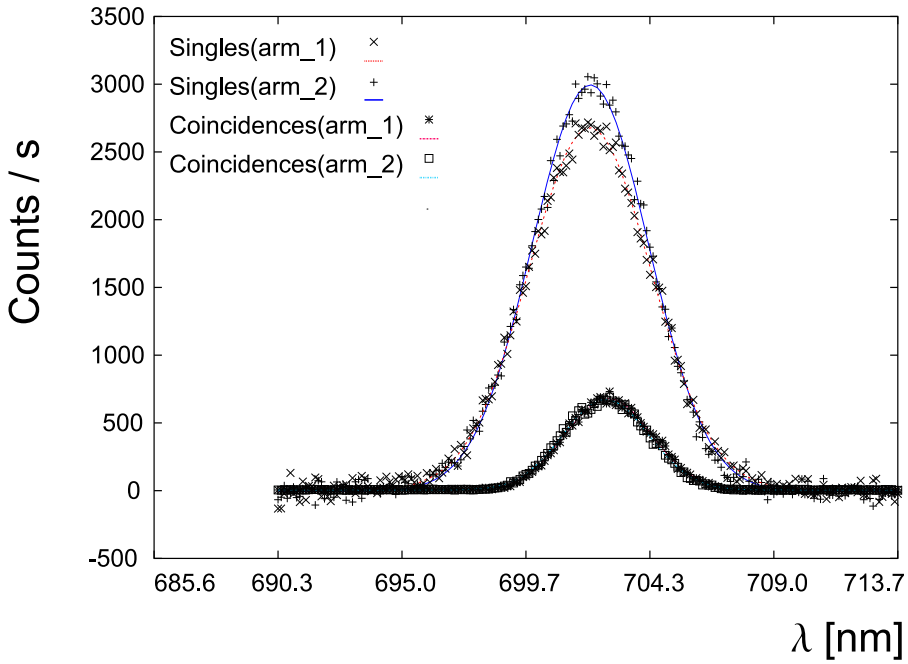

Figure 4.1: Single and coincidence spectra of down conversion photons in both arms behind the BBO crystal. For the singles background counts are substracted.

This bandwidth corresponds to a correlation time of the downconverted photons of $(\Delta\tau_C)_{exp} = 357$ fs. It is slightly above the value the setup was designed for (s. section 3.1) which could indicate that the alignment of the setup is not entirely optimal.

As mentioned in sections 2.3.2 and 3.1 the downconversion source produces photons in the state given by equation (2.45). To generate any of the four Bell states from (2.45), one has to perform phase shifts and polarization rotations on only one of the two photons (s. sections 2.1.2 and 3.1) accordingly. Since we couple the downconversion light into single mode fibers which can cause arbitrary polarization modifications and birefringence, one has to properly compensate for these effects. With polarization controller units[2] it is possible to "neutralize" an optical fiber modulo a 2π relative phase shift beween H and V polarization. These units allow controlled polarization manipulations comparable to the chain of $\lambda/4$- and $\lambda/2$-waveplates presented in section 3.2. To prepare the initial Bell state of the game, i.e. the ϕ^+, we have to rotate the polarization of one of the downconverted photons by 90° and set the phase in equation (2.45) to $\varphi = 0°$. This can be done by either neutralizing both fibers and then rotate the polarization in one arm with

[2]Polarization controllers are also referred to as "bat ears" or in the Austrian and Bavarian language area they bear the tuneful name "Ohrwaschl-Geräte".

a $\lambda/2$-waveplate set to 45°, or neutralizing just one of the fibers and adjust the polarization controllers in the other fiber such that the setting corresponds to a $\lambda/2$-waveplate set to 45°.

To neutralize a fiber, I placed one polarizer in front of the input fiber coupler and another one with perpendicular setting behind the output coupler. By setting the three loops of the controller unit accordingly, one can minimize the count rates for say horizontal input polarization. In this way it is ascertained that the fiber transforms a horizontal polarized photon into horizontal polarized one. To compensate a relative phase shift between horizontal and vertical polarization, one then can switch to the $+45°/-45°$-degree basis and repeat the minimization procedure. As this will in general change the properties of the fiber for horizontal polarization adjusted before, one has to switch between both bases and iteratively set the loops as independent as possible for each basis (e.g. always try to minimize the count rates with the same two of the three loops for one basis). To adjust the polarization controller such that it acts as a half waveplate, the procedure is the same, only the polarizer settings have to be changed accordingly. With this technique I was able to adjust the polarization controllers such that less then 0.2% of the photons detected with parallel polarizers were observed for a perpendicular setting of the two polarizers. This is assumed to be sufficient for our purpose, because it corresponds to less than ten coincidences per second above the dark count rate, which has to be compared with 6000 coincidences when the polarizers are removed.

However, maintaining the polarization[3] when passing through a fiber is not enough to prepare the desired state, because the relative phase between both arms has to be fixed to obtain the desired Bell state. In principle this can also be achieved with the polarization controller units but then it is difficult to ascertain that the phase shift between horizontal and vertical polarization is equal to zero and not $n\ 2\pi$, with integer n. Therefore, this relative phase shift is easily and accurately set by tilting the compensation crystals (s. section 3.1), as they cause phase shifts between horizontal and vertical polarization.

4.1.1 Polarization Correlations

To ascertain that I really produced the desired state, I analyzed the state behind the fibers in the H/V and $+45°/-45°$ basis with a polarizer in both arms as shown in figure 4.2. Then it is possible with two measurements (1. both polarizers analyze in H/V basis; 2. both polarizers analyze in $P = +45°/M = -45°$ basis) to identify

[3]Maintenance of the polarization here means that H, V, $+45°$ and $-45°$ polarized input photons will also be detected with the respective polarization after the fiber. No polarization is damped out, as it is the case for the commercially available 'polarization maintaining' fibers.

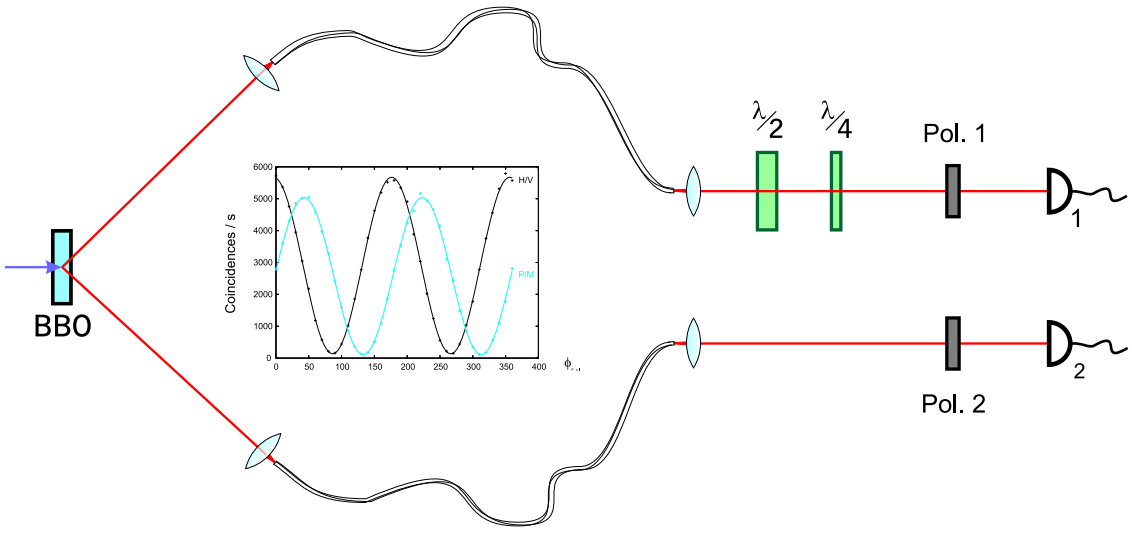

Figure 4.2: With this setup it is possible to prepare any of the four Bell states and measure its polarization correlations, a violation of the CHSH inequality and the entanglement witness for respective polarizer and waveplate settings.

any of the four Bell states:

$$
\begin{aligned}
|\psi^+\rangle &= \tfrac{1}{\sqrt{2}}(|HV\rangle + |VH\rangle) &&= \frac{1}{\sqrt{2}}(|PP\rangle - |MM\rangle) \\
|\psi^-\rangle &= \tfrac{1}{\sqrt{2}}(|HV\rangle - |VH\rangle) &&= \frac{1}{\sqrt{2}}(|MP\rangle - |PM\rangle) \\
|\phi^+\rangle &= \tfrac{1}{\sqrt{2}}(|HH\rangle + |VV\rangle) &&= \frac{1}{\sqrt{2}}(|PP\rangle + |MM\rangle) \\
|\phi^-\rangle &= \tfrac{1}{\sqrt{2}}(|HH\rangle - |VV\rangle) &&= \frac{1}{\sqrt{2}}(|MP\rangle + |PM\rangle).
\end{aligned}
$$

It is this method of identification which is most commonly used to characterize the correlations between the polarizations of a photon pair. To record the polarization correlation functions, i.e. the expectation value $E_{\alpha,\beta} = \langle \sigma_\alpha \sigma_\beta \rangle$ for polarization measurements of the two photons at angles α and β, polarizers are placed in both arms behind the source (s. figure 4.2). Firstly, one polarizer is set to 0° which corresponds to the case that only horizontal polarized photons can pass. Then, the other polarizer is rotated by 360° in steps of ten degrees and the coincidences between the detectors in both arms within one second are counted.

To characterize the quality of the polarization correlations, the visibilities of

the sinusoidal pattern can be used:

$$V = \frac{n_{max} - n_{min}}{n_{max} + n_{min}} \tag{4.2}$$

Experimental values for V are obtained from a sinusoidal fit of the function

$$f_{ij}(\phi) = \frac{a}{2}\left(1 - V_{ij}\sin\left(\frac{\phi - \phi_0}{p}\right)\right) \tag{4.3}$$

to the measured data points. The angular setting of the rotating polarizer is referred to as ϕ, the amplitude of the function corresponding to the coincidence count rate is termed a, p determines the periodicity of the function ($p = \frac{360}{4\pi}$ for $f_{ij}(\phi) = \sin(\phi/p)$), and ij denotes the measurement basis.

The observed sinusoidal dependence on the orientation of the polarizers is shown in figure 4.3 and proves with a visibility of $V_{H/V} = 95.6 \pm 0.6\%$ that, if one photon of a pair is vertically polarized, the other is found to be horizontally polarized and vice versa. However, this does not prove that the photon pair is in an entangled state, because the state $\psi = (|HV\rangle\langle HV| + |VH\rangle\langle VH|)/\sqrt{2}$, which is a statistical mixture, would show the same behavior.

The peculiarity of entangled states is that they show these correlations independent of the measurement basis. To verify that the produced state is entangled, we therefore checked the correlations also for the P/M basis (one polarizer set to $P = +45°$) and the L/R basis (one polarizer set to $P = +45°$ preceeded by a $\lambda/4$ waveplate set to $0°$ in both arms). Again, we observe sinusoidal curves (figure 4.3) with visibilities of $V_{P/M} = 96.2 \pm 0.7\%$ and $V_{L/R} = 96.9 \pm 0.6\%$, which no separable state could reproduce. The product state considered before would for example show a completely flat curve if one of the polarizers is set to $P = +45°$.

For the measurements presented above, we observed single detector count rates N_{D1} and N_{D2} of approximately 40000 and 65000 per second. Also the single count rates showed a (much less pronounced) sinusoidal variation when rotating the polarizer, because of the different beam walk-off effects for unequal polarizations described in 3.1. These single detector clicks are assumed to be randomly distributed in time, and will hence cause accidental coincidences for some given time window in which one click in each detector leads to an event which is counted as a coincidence. As long as the single count rates are below the inverse of the coincidence time window, which was set to $\tau_{coinc} = 21$ ns in our case, one can calculate the number of accidental coincidences from the two independent single count rates via

$$N_{acc} = N_{D1}N_{D2}\tau_{coinc} \quad . \tag{4.4}$$

For the measurement of the polarization correlations, one obtains $N_{acc} = 54.6\ \mathrm{s}^{-1}$. Subtracting the accidental coincidences from the measured rates yields the visibilities:

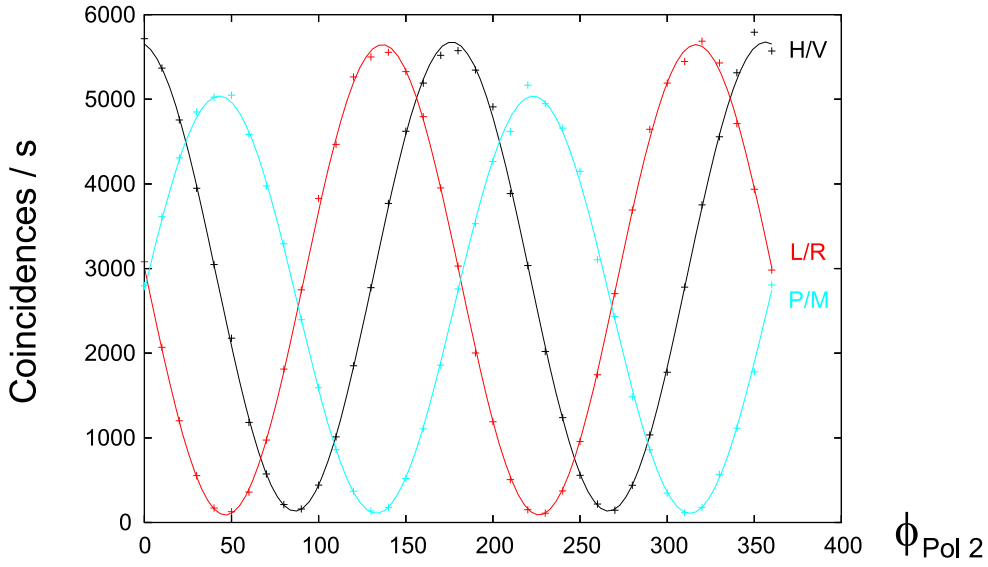

Figure 4.3: Polarization correlations for different settings of analyzer 1.

$$V_{H/V} = 97.4 \pm 0.6\%,\ V_{P/M} = 98.3 \pm 0.8\% \text{ and } V_{L/R} = 98.8 \pm 0.6\%.$$

These results are a proof for non-classical correlations between the two photons of one pair.

4.1.2 Violation of Bell's inequality

Another test if the created photon pairs show quantum correlations is to test for a violation of the CHSH inequality (2.6). To calculate $S(\alpha, \alpha', \beta, \beta')$, we have to determine the expectation values of $E(i, j)$ (s. section 2.1). For each particle $P = a, b$ and analyzer setting $\varphi = \alpha, \alpha', \beta, \beta'$, three measurement outcomes are possible:

$$P_\varphi = \begin{cases} +1 & \text{“spin up” particle a, b} \\ -1 & \text{“spin down” particle a, b} \\ 0 & \text{particle a, b not detected} \end{cases}$$

“Spin up” and “spin down” correspond in our case to orthogonal polarizations, φ and φ_{perp}, and not to opposite directions. Hence we expect maximal violation of the inequality for angles $\alpha = 0°, \alpha' = 45°, \beta = 22.5°$ and $\beta' = 67.5°$. For a given state ψ, the expectation values of the product of a_i and b_j can be written as

$$E(i, j) = \int \langle a_i(\psi) \rangle \langle b_j(\psi) \rangle d\rho. \tag{4.5}$$

To determine the expectation value for the settings $(i, j) = (\alpha, \beta)$ we have to perform four coincidence measurements for given bases α, $\alpha_\perp$ for particle a, and β, $\beta_\perp$ for particle b, yielding the four possible combinations:

a \ b	α (+1)	$\alpha_\perp$ (-1)
β (+1)	$n_{\alpha\beta}$	$n_{\alpha_\perp\beta}$
$\beta_\perp$ (-1)	$n_{\alpha\beta_\perp}$	$n_{\alpha_\perp\beta_\perp}$

Then, we can calculate the expectation value

$$E(\alpha, \beta) = \frac{n_{\alpha\beta} - n_{\alpha_\perp\beta} - n_{\alpha\beta_\perp} + n_{\alpha_\perp\beta_\perp}}{n_{\alpha\beta} + n_{\alpha_\perp\beta} + n_{\alpha\beta_\perp} + n_{\alpha_\perp\beta_\perp}}. \tag{4.6}$$

The signs in the numerator correspond to the product of the measurement outcomes of particle a and b for respective angular settings.

To calculate the standard deviation $\Delta S = \sqrt{\sum_{i,j}(\Delta E(i,j))^2}$ of $S(\alpha, \alpha', \beta, \beta')$ one has to compute the standard deviations via standard error propagation techniques assuming independent errors on the individual measurements

$$\Delta E(i,j) = \sqrt{\sum_{k,l}\left(\frac{\partial E(i,j)}{\partial n_{k,l}}\right)^2 (\Delta n_{k,l})^2} \tag{4.7}$$

of the expectation values $E(i, j)$, with $i = \alpha, \alpha'$, $j = \beta, \beta'$ and $k = i, i_\perp$, $l = j, j_\perp$. The standard deviation of the $n_{k,l}$ counted events is assumed to be Poisson distributed: $\Delta n_{k,l} = \sqrt{n_{k,l}}$.

The results $n_{k,l}$ of the measurements performed on a ϕ^+-state from the downconversion source are given in table 4.1. Inserting the values of table 4.1 into equations

a \ b	$\alpha = 0°$ (+1)	$\alpha_\perp = 90°$ (-1)	$\alpha' = 45°$ (+1)	$\alpha'_\perp = 135°$ (-1)
$\beta = 22.5°$ (+1)	24582	4020	23617	5340
$\beta_\perp = 112.5°$ (-1)	6280	25965	3435	28643
$\beta' = 67.5°$ (+1)	3850	23959	21616	5670
$\beta'_\perp = 157.5°$ (-1)	27466	5056	5264	28827

Table 4.1: Coincidence count rates in 5s for measurement settings corresponding to a maximal violation of the CHSH inequality.

4.6 and 4.7, we obtain

$$S = 2.722 \pm 0.006. \tag{4.8}$$

Inequality (2.6) ($S_{Cl} \leq 2$) was violated by **122 standard deviations** in 5 seconds integration time per angular setting and the maximal value of $S_{qm} = 2\sqrt{2}$ predicted by quantum mechanics was almost reached.
Within the 5 s measurement time for each angular setting, an average of 304 000 and 190 000 singles were detected in detectors D_1 and D_2, respectively. These single events lead - as described before for the polarization correlation functions - to 242.6 accidental coincidences within the time of data collection. Subtracting the accidental coincidences from the measured total count rates and repeating the above calculation yields

$$S = 2.766 \pm 0.006, \tag{4.9}$$

corresponding to a violation of Bell's inequality by **130 standard deviations** in 5 s per angular setting.

4.1.3 Entanglement witness

Yet another method to detect entanglement was presented in section 2.1.3. Given the case that one is aiming at producing some particular state — as in our case, where we wish to produce the ϕ^+ — one can construct an entanglement witness W and measure if one succeeded [38]. To find out what we actually have to measure to determine the value of $Tr(W\rho)$, we use the witness operator as defined in equation (2.12). With $Tr(A+B) = Tr(A) + Tr(B)$ and the invariance of the trace under basis transformations, one obtains:

$$\begin{aligned}
Tr(W\rho) &= \sum_{i,j} \langle ij| \frac{1}{2}(|HV\rangle\langle HV| + |VH\rangle\langle VH| - |PP\rangle\langle PP| - |MM\rangle\langle MM| \\
&\quad + |LL\rangle\langle LL| + |RR\rangle\langle RR|)\, \rho\, |ij\rangle \\
&= \frac{1}{2}\Big(\sum_{i,j} \langle ij|HV\rangle\langle HV|\rho|ij\rangle + \sum_{i,j} \langle ij|VH\rangle\langle VH|\rho|ij\rangle - \sum_{i,j} \langle ij|PP\rangle\langle PP|\rho|ij\rangle \\
&\quad - \sum_{i,j} \langle ij|MM\rangle\langle MM|\rho|ij\rangle + \sum_{i,j} \langle ij|LL\rangle\langle LL|\rho|ij\rangle + \sum_{i,j} \langle ij|RR\rangle\langle RR|\rho|ij\rangle \Big) \\
&= \frac{1}{2}(\langle HV|\rho|HV\rangle + \langle VH|\rho|VH\rangle - \langle PP|\rho|PP\rangle - \langle MM|\rho|MM\rangle \\
&\quad + \langle LL|\rho|LL\rangle + \langle RR|\rho|RR\rangle).
\end{aligned}$$

To determine the expectation values, I performed the corresponding measurements in the three different bases. Only three measurements are required when four detectors, waveplates and two polarizing beamsplitters are available. Any combination

of two detectors behind a polarizing beamsplitter can be associated with one of the basis vectors. Since I was only using two detectors I performed four measurements in each basis for the four possible combinations of two polarizers in front of the detectors. The results are given in table 4.2.

Pol. A	Pol. B	Coinc.	Sing. A	Sing. B	acc. Coinc.
H	H	28300	340 k	172 k	246
H	V	771	340 k	206 k	294
V	H	296	271 k	172 k	196
V	V	27857	273 k	213 k	244
P	P	25053	310 k	180 k	234
P	M	534	312 k	201 k	263
M	P	623	299 k	180 k	226
M	M	30662	301 k	204 k	258
R	R	431	301 k	184 k	233
R	L	28396	302 k	196 k	249
L	R	25701	301 k	183 k	231
L	L	1060	302 k	197 k	250

Table 4.2: Coincidence and Single count rates and accidental coincidences in 5s for measurement settings of polarizers in arm A and B to calculate the entanglement witness.

Calculating the necessary expectation values from table 4.2, we determine

$$Tr(W\rho) = -0.467 \pm 0.001. \tag{4.10}$$

This corresponds to a probability p of 95.6% of really having created the desired ϕ^+-state in accordance with the assumptions made in 2.1.3. This probability accords to the visibilities obtained from the polarization correlation curves, where $(1-p)$ corresponds to the count rates in the minima of the curves. From the single count rates, one can calculate the number of accidental coincidences for the coincidence time window, which was again set to 21 ns. Subtracting the accidental coincidences from all measured coincidences in 5 s yields

$$Tr(W\rho) = -0.480 \pm 0.001. \tag{4.11}$$

The probability p of having created the ϕ^+-state then becomes 97.3%.

From the obtained count rates, the recorded spectra, the visibilities of the polarization correlation curves, the violation of the CHSH inequality and the measurement of the entanglement witness I conclude that it is possible with our source to produce highly entangled photon pairs at a high rate, which fulfill the constraints on the initial state formulated in the preceeding sections 3.1 and 3.3.

4.2 The Hong-Ou-Mandel Dip

After the players performed their operations on their respective photon, the final state of the game is sent to the complete Bell state analyzer. As explained in section 3.3 and shown in figure 3.9, the two photons are superposed on the beam splitter in order to distinguish the $|\psi^+\rangle$ from the other three Bell states by virtue of Hong-Ou-Mandel (HOM) interference.

To observe the HOM interference effect, the coincidence rate was measured as a function of the relative path length difference Δl between the two arms of the down conversion crystal to the beam splitter. Therefore, one of the fiber couplers behind the down conversion was mounted on a motor-driven translation stage and displaced in the direction of the beam. This changes the distance from the coupler to the beam splitter and hence the relative path length difference between the two arms.

When the distance Δl is close to zero the coincidence count rate drops to a few percent of the rate in the wings of the HOM-dip, as shown in figure 4.4 for a $|\psi^-\rangle$ being the input state[4].

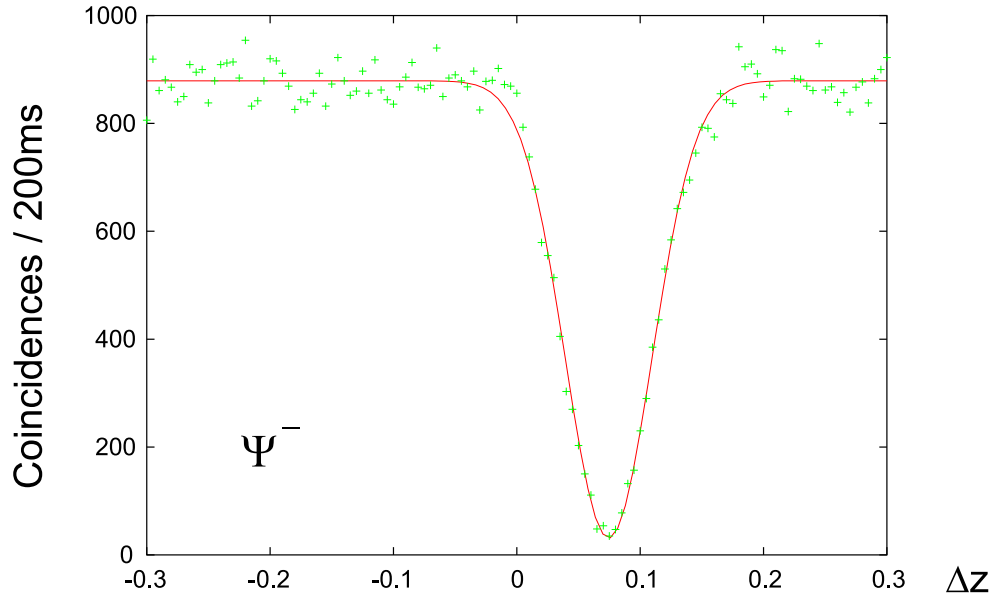

Figure 4.4: Hong-Ou-Mandel interference on a beam splitter for a $|\psi^-\rangle$ input state.

On the abscissa the position of the fiber coupler is displayed. The zero-position is just the starting position of the motor and does not mark the position of equal pathlength difference here. The motor position Δz where both photons travel the

[4]To ensure that the input state in fact is the $|\psi^-\rangle$ we performed a measurement of the polarization correlations with the setup shown in figure 4.2 before sending the photons to the beam splitter.

same distance from their origin to the beam splitter is defined by the minimum of the dip.

For the Bell state analysis, the fiber coupler has to be set to the exact minimum position Δz_0. A displacement from this position in the experiment would cause a $|\psi^-\rangle$ (in this case) to be identified as a $|\psi^+\rangle$. Analogously, the other two Bell states $|\phi^-\rangle$ and $|\phi^+\rangle$ showing destructive interference at the beam splitter would cause a similar misidentification of Bell states. For optimal alignment of the fiber coupler, the minimum position was obtained by fitting a Gaussian function to the data points:

$$f(x) = \; a\, e^{-\frac{(\Delta z - \Delta z_0)^2}{w^2}} + y_0 \tag{4.12}$$

Here, a denotes the (negative) amplitude of the dip compared to the coincidence count ratevalue y_0 far out in the wings. According to equation (4.2), the visibility can be calculated from a and y_0 analogously and is obtained to be $V_{dip}(\psi^-) = 95.3 \pm 0.8\%$. The visibility gives a lower bound on the number of wrongly identified coincidence events.

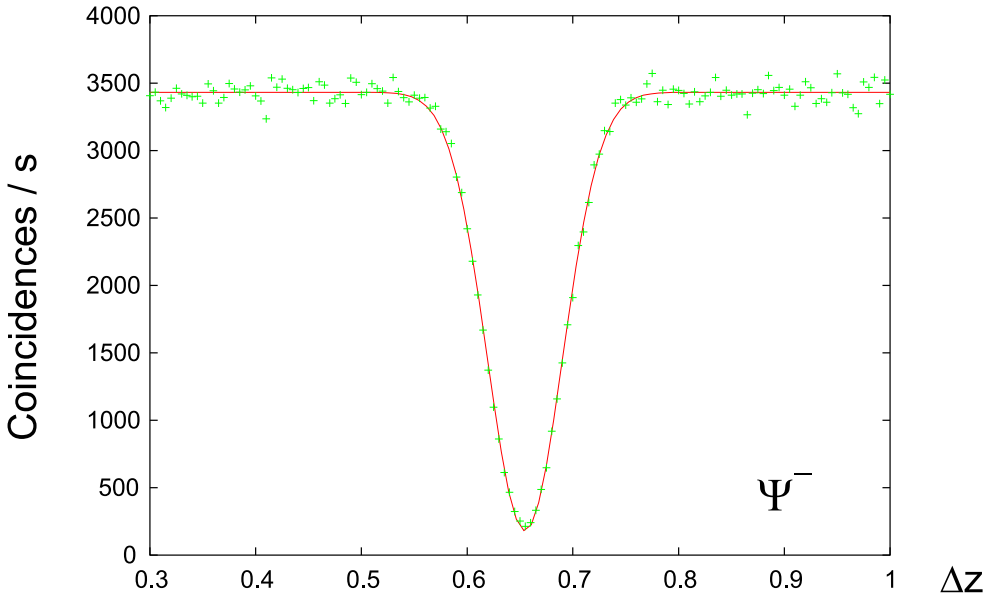

Figure 4.5: Hong-Ou-Mandel dip for the $|\psi^-\rangle$.

The width w of the dip (equation 4.12) determines the correlation time [70] and was found to be 99.4 ± 1.6 μm. This corresponds to a correlation time of the down converted photons of $\frac{w}{c} = (\Delta\tau_C)_{dip} = 331.6 \pm 5.3$ fs, which is in good agreement with the value obtained from the spectra in the previous section. Via equations (3.4-3.5) the collected bandwidth can then be estimated as $\Delta\lambda \approx 5$ nm. This indicates as well (s. section 4.1) that that the alignment of the down conversion source could

still be optimized, because it was initially designed for 4 nm.

To show how the $|\psi^+\rangle$ can be distinguished from the other three Bell states, we measured the HOM-interference for all four Bell states. This is of course inherent in analyzing all four Bell states with the setup discussed in section 3.3, however, for (online) alignment of the setup it is advantageous to place only two fiber couplers in both output ports of the beam splitter and couple into single mode fibers connected to the detectors.

For the purpose of demonstrating the complete Bell measurement, the down conversion source was adjusted such that $|\psi^-\rangle$ is obtained as an initial state measured behind a $\lambda/2$- and a $\lambda/4$-waveplate in one arm, both set to 0°. By adjusting the waveplates we are able to implement first strategies of a quantum game, which here correspond to switching between the four Bell states. The resulting HOM-dip after alignment of the spatial overlap as discussed in section 3.3 is shown in figure 4.5. The visibility of $V_{\psi^+} = 90 \pm 0.2$ % is again obtained by a Gaussian fit.

By setting the $\lambda/4$-waveplate to 90° and leaving the $\lambda/2$-plate unchanged one can switch from $|\psi^-\rangle$ to $|\psi^+\rangle$ and observes the HOM-bump as expected from the calculation in section 3.3. The bump is shown in figure 4.6 and has a visibility (calculated for $a \rightarrow -a$) of $V_{\psi^+} = 92.8 \pm 0.2$ %.

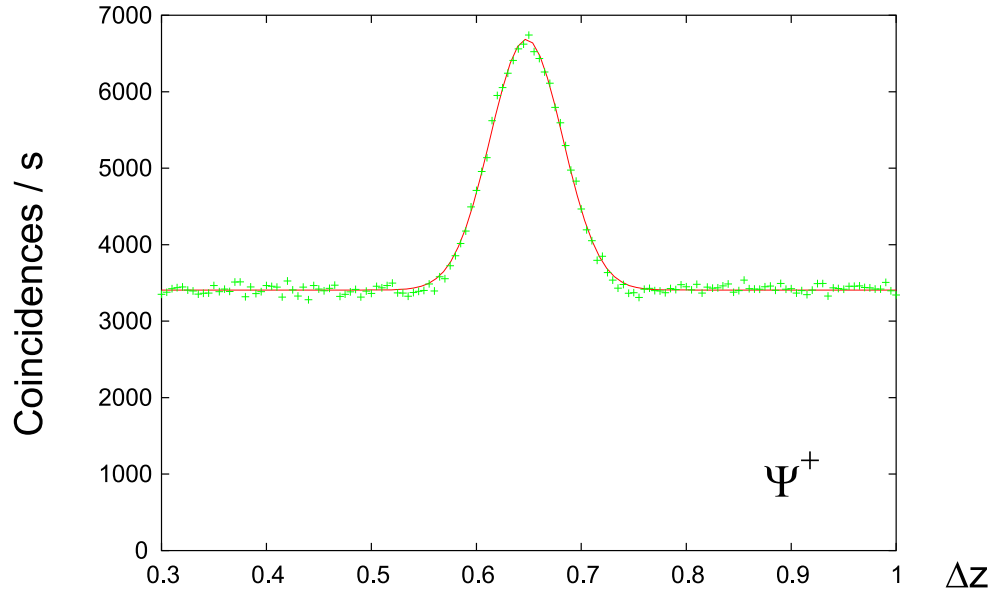

Figure 4.6: Hong-Ou-Mandel bump for the $|\psi^+\rangle$.

If the $\lambda/4$-waveplate remains at 90° but the $\lambda/2$-plate is set to 45°, one has prepared $|\phi^+\rangle$. Here, the visibility of the HOM-dip was found to be $V_{\phi^+} = 80 \pm 0.2$ %.

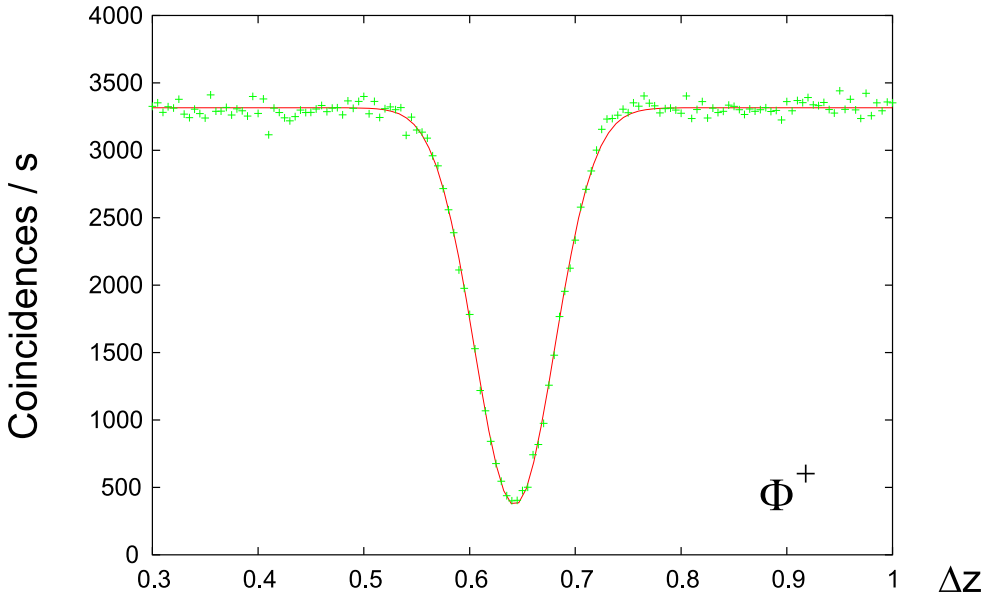

Figure 4.7: Hong-Ou-Mandel dip for the $|\phi^+\rangle$.

The fourth Bell state is then obtained by switching the $\lambda/4$-plate back to 0°. Again, a HOM-dip is observed with a visibility of $V_{\phi^-} = 82.1 \pm 0.2$ %.

All of the last four measurements presented above were performed in one run, one after the other, just by switching the waveplate settings and hence switching between the Bell states. This way it was ensured that the state to start with from down conversion did not change due to experimental drifts. The setup was not realigned in between any two measurements.

Compared to the first measurement of $|\psi^-\rangle$ presented in the beginning of this section the visibilities in this measurement are lower, for the $|\phi\rangle$-states even by $10 - 15\%$. In the first measurement the alignment was similar as in the last four except from the fact that only one waveplate (the $\lambda/2$) was placed in one of the arms. Introducing the second waveplate therefore seems to have slightly influenced the quality of the spatial mode, for example caused by beam walk-off, and hence the visibility of the dip. The significantly lower visibilities for the $|\phi\rangle$-states could be due to a wedge of the $\lambda/4$-waveplate. During the alignment of the setup, i.e. before measuring the dip for the $|\psi^-\rangle$, the waveplate was set to 0°. For $|\phi\rangle$ states, it had to be rotated by 90°, and hence a wedge could significantly affect the spatial mode.

However, as already discussed in section 3.3, there might as well be other imperfections which will affect the correlations between the photons and lead to a reduced dip visibility. We observed for example that the spectra of the collected down conversion light was subject to slight drifts, because the beam pointing of the pump light was not entirely stable (even for active beam lock in the laser system

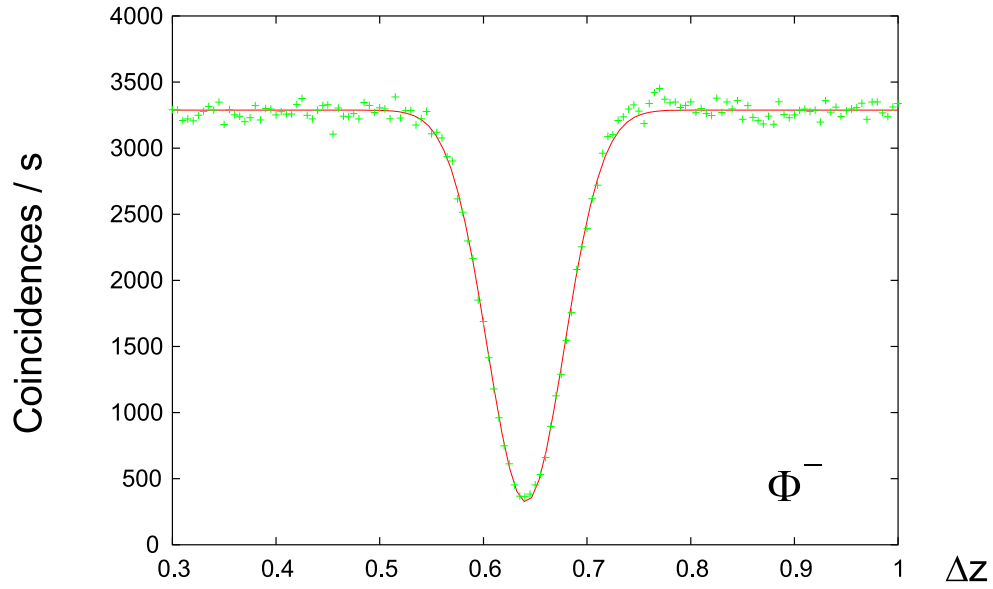

Figure 4.8: Hong-Ou-Mandel dip for the $|\phi^-\rangle$.

used[5]). In some cases fluctuations of about 20% in the single (and hence also the coincidence) count rates were observed on a time scale of roughly 15 minutes. If these fluctuations are due to a decrease in coupling efficiency (and not output power), the beam might not always point at the same spot in the crystal, which in turn would also affect the collected center wavelength. Another reason could be a remaining temporal distinguishability of the photons as discussed in section 3.1.

Among the imperfections reducing the visibility of the observed HOM-interference patterns, spatial mode matching seems to be the main problem. In previous experiments [63] it was observed as well that it is crucial to select the photons with equal wave vector in both arms to obtain high dip visibilities. Hence, we coupled the down conversion photons into single-mode fibers to select one well defined mode. We were able to couple approximately 90% of the photons observed with a multi-mode fiber into a single-mode fiber, and in this case we also obtained the maximally achieved dip visibilities shown in figure 4.4.

In the experiment only one of the modes will be coupled into a single mode fiber, while in the other arm the photons are processed for the further state analysis and will then be directly incident on a freestanding detector. Therefore, it will be important for an improvement of the experimental results to adjust curvature and diameter of the beams at the output couplers as accurately as possible to fulfill the mode matching conditions given in 3.3.

Nevertheless, the observed Hong-Ou-Mandel interference clearly shows a differ-

[5]Spectral Physics

ent behavior (constructive interference resulting in the HOM-bump; figure 4.6) for the $|\psi^+\rangle$ than for the other three Bell states (destructive interference resulting in the HOM-dips; figures 4.5-4.8). Further processing of these states is presented in the following chapter.

4.3 Identification of Bell States

4.3.1 The Interferometer

The interferometer needed for the temporal separation of horizontally and vertically polarized photons in order to be able to identify the $|\psi^-\rangle$ is realized as a folded asymmetric Mach-Zehnder interferometer instead of the open one shown in figure 3.9. The processing of the input states is the same, but a folded Mach-Zehnder interferometer is easier to align and probably more stable, because one needs only a single polarizing beam splitter (and two retroreflecting prisms, which compensate for alignment angle errors in one direction as a cat-eye, and therefore we found them to be less critical than beam splitters in terms of stability).

The relative pathlength difference between the two arms of the interferometer determines the relative phase shift a vertically polarized photon suffers relative to a horizontally polarized one. As discussed in section 3.3, this relative phase shift has to be set to a fixed value for the correct identification of the $|\phi\rangle$ states. However, this phase shift might not be stable due to vibrations and long term drifts of the components, namely the prism and the polarizing beam splitter positions. Even air flow suffices to change the optical pathlength of the interferometer-arms and therefore also the relative phase.

Hence, it is necessary to stabilize the distance between the components of the interferometer to an accuracy of less than $0.035\lambda = 25$ nm to allow for an error of maximally 5%. This is achieved with a configuration shown in figure 4.9. The 45° polarized beam of a Helium-Neon (He-Ne) laser is aligned such that it travels about 1 cm below the beamline of the photons from the down conversion source. Behind the interferometer, the He-Ne beam is analyzed in the $+45°/-45°$-basis. For this purpose the recombined beams are sent through a $\lambda/2$-waveplate set to 22.5° and a polarizing beam splitter. For detection in the $+45°/-45°$-basis it is not possible anymore to infer the interferometer arm a photon of the adjustment laser took by its polarization, and interference from the two different paths is observed with standard PIN photodiodes in each of the output ports. The interference patterns on both photodiodes will be shifted in phase by π relative to each other and hence the observed photocurrent difference can be used as an error signal to control the path length difference. The obtained error signal is fed into a controller, which regulates the high-voltage for a piezoceramic-translator, adjusting the position of one of the prism mounts and thereby closing the feedback loop [78].

The stability of the interferometer under measurement conditions locked to the He-Ne reference laser can be estimated from figure 4.10. The observed variations of the count rates due to phase shifts over approximately 15 minutes are still rather large, i.e. up to 50% of the count rate. This noise will accordingly affect the quality of the measurement results. The observed phase instabilities could mainly be tracked down to the mechanical response of the setup to vibrations caused by the

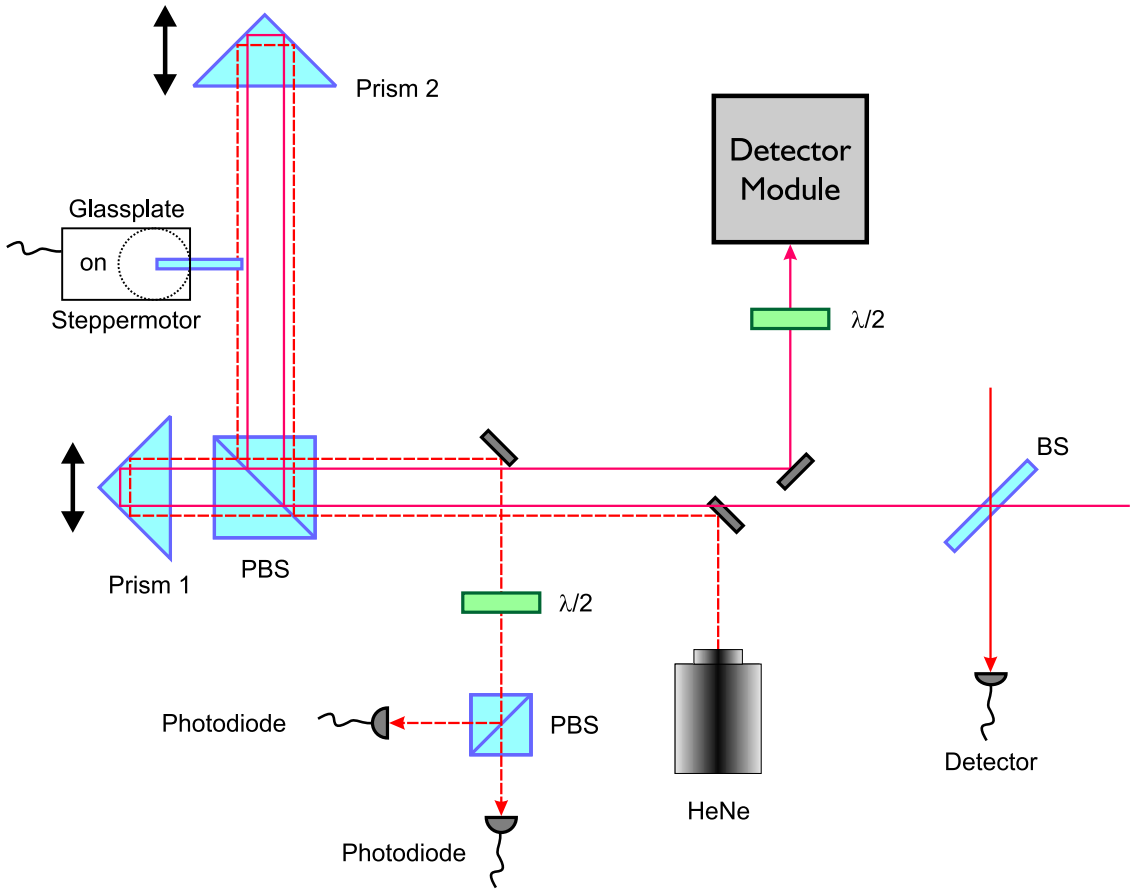

Figure 4.9: Setup of the intererometer: the HeNe-beam (broken line) is displaced about 1 cm in height relative to the path of the downconverted photons (solid line). Prism 1 is mounted on a micrometer-driven translation stage to adjust beam overlap, prism 2 on piezo-driven translation stage to adjust the phase.

watercooling system of the Argon-ion laser. To prevent these fluctuations, more stable mounts for the prisms and the polarizing beam splitter seem to be necessary. Furthermore, it would help to decrease the integration time constant of the controller to be able to compensate for faster fluctuations than currently possible.

However, it is not enough to just keep the phase as stable as possible, one also needs to be able to set it to the value desired for the Bell measurement. To achieve this, a microscope objective slide (glass plate, 1 mm thick) was introduced into the He-Ne reference beam in one of the interferometer arms (s. figure 4.9).

By tilting that glass plate, one can adjust the pathlength difference of the reference beam. The controller will try to keep this distance constant and hence change

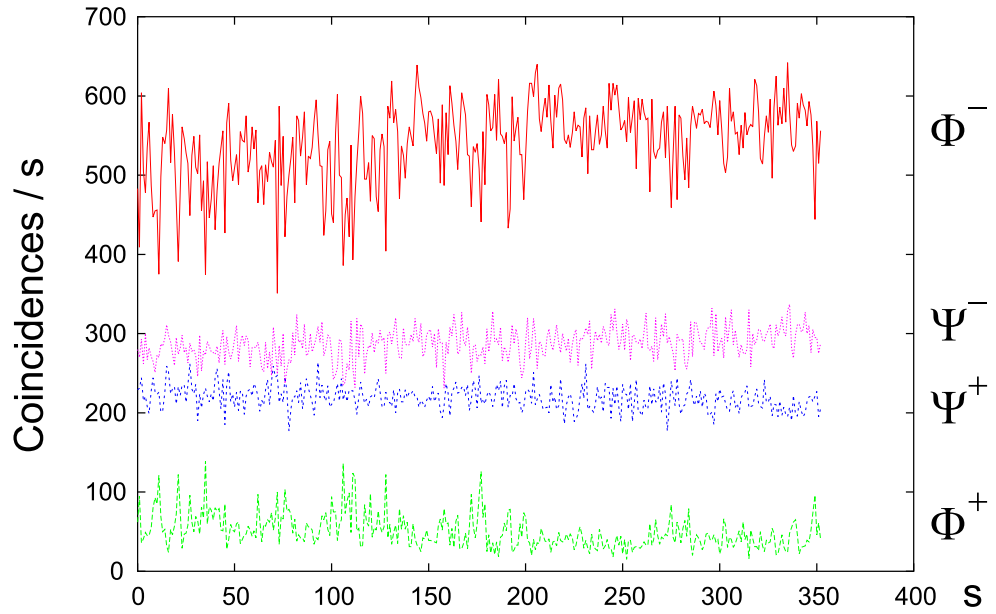

Figure 4.10: Totaled count rates per second of all detector combinations corresponding to one of the four Bell states. The data was collected in approximately fifteen minutes, showing the long term stability of the interferometer. (Only 360 datapoints (sec) were recorded in this time because the readout and plotting takes about $1 - 2.5$ seconds per datapoint.) The input state was a $|\phi^-\rangle$.

the relative phase for the down conversion photons travelling along the different paths.

To find the right setting of the glass plate for the experiment, we chose the $|\phi^+\rangle$ as input state for the Bell state analyzer and observed the coincidence count rates for detector combinations which are identified with the two $|\phi\rangle$ states. Changing the relative phase between the long and short arm of the interferometer continuously changes the relative phase between horizontal and vertical polarization. Accordingly, $|\phi^+\rangle$ can be transformed into $|\phi^-\rangle$ and hence give a detection signal which would be expected from the calculation presented in section 3.3 for $|\phi^-\rangle$ as shown in figure 4.11. For a known input state (determined independently, for example by its polarization correlations) it is thus possible to find the position of the glassplate corresponding to the phase shift which was assumed for the calculation in 3.3, and allows for a correct assignment of detection events to input states.

However, from the curves presented in figure 4.11 it is also apparent that it is indeed possible to distinguish between the different detection signals expected for the two $|\phi\rangle$–states. Final results on the complete Bell state analysis will be presented in the following section.

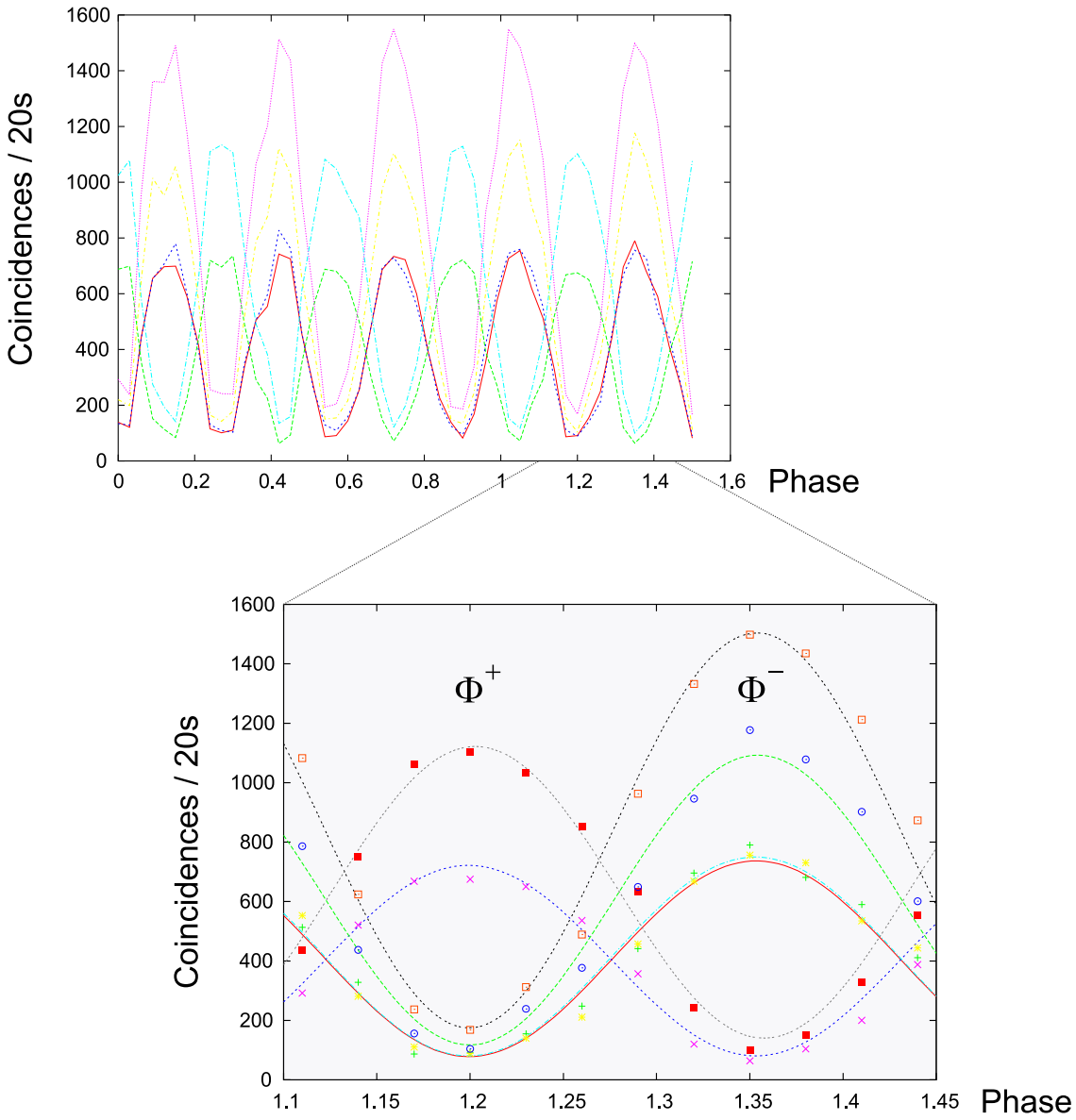

Figure 4.11: Dependence of the count rates for all combinations of detectors corresponding to $|\phi^+\rangle$ and $|\phi^-\rangle$ states on the interferometer path length difference. This corresponds to scanning the relative phase between the two arms; the input state for this run was a $|\phi^+\rangle$.

4.3.2 The Detector Module

For the detection of the photons after they travelled through the setup we use silicon avalanche photodiodes (APD) from Perkin-Elmer (formerly EG&G Optoelectronics)

[79],[80]. An APD basicly consists of an absorption region and a multiplication region (s. figure A.1). If an incident photon is absorbed, an electron-hole pair is created. To separate the photo-generated electrons from the holes in the absorption region, a relatively weak electric field is applied to attract the electrons towards the multiplication region, where a high electric field causes an avalache by impact ionization.

For single photon counting the detectors are biased approximately 15 V above their breakdown voltage. In this so-called Geiger mode, even a single photoelectron or a thermally generated one may cause an avalanche pulse which discharges the diode slightly below the breakdown voltage. The quantum efficiency for 702 nm photons is typically around 70%, while the photoelectron detection probability in the Geiger mode is increasing with reverse bias voltage and reaches approximatly 55% at 20 Volts above the breakthrough voltage. The photon detection probability is given by the product of the quantum efficiency and the photoelectron detection probability and reaches roughly 40% in our case.

When an avalanche is triggered, the process has to be suppressed before the current flowing through the device destroys the APD. Hence one has to quench the avalanche, and after some recovery time reactivate the diode by raising the excess bias voltage above the breakdown voltage. To do so we are using a passive quenching circuit, where the APD is connected in series with a large quench resisitor and a small series resistor. When the diode is in the conducting state after an avalanche was triggered by either a photo- or thermal electron, a suffiently large current, to maintain the cunductive state is supplied by parasitic capacitances for a short time. If the current through the diode drops below the so-called latching current, the APD switches to the non-conducting state and recharges with the time constant $\tau = C_p R_q \approx 0.6\mu$s, where $C_p \approx 1.6$ pF is the stray- and junction capacitance of the APD. For a large quenching resistor the diode will normally be in the non-conducting state. The width of the breakdown pulse depends on the bias voltage and the capacitances and is in our case about $2ns$ at $U_{bias} = 15V$. (For applications of single-photon avalanche diodes, e.g in quantum cryptography, see [81].)

An important parameter of a detector is its dark count rate, which is determined by the rate an avalanche is triggered by bulk carriers generated in thermal, tunneling or trapping processes. For the detectors I used the dark count rates, depending on the temperature at which they are operated, are given in figure A.3. The thermal noise in the detector was minimized by cooling the block in which the detector is mounted. Under experimental conditions we observed dark count rates of approximately 1500 single events per second which did not lead to an observable amount of accidental coincidences.

As shown in figure 3.11, four of the detectors were mounted in one detector module together with the polarizing beam splitter and the two 50:50 beam splitters for the final state analysis. The module is very compact and it turned out to be

relatively easy to align as a whole. Inside the module the detectors are mounted in two blocks which are cooled by Peltier elements. All detectors are placed at an equal optical path length from the polarizing beam splitter. The three beam splitters were aligned beforehand such that the images of all four detectors overlap when viewed in the direction of the input beam. A picture of the detector module is shown in figure 4.12

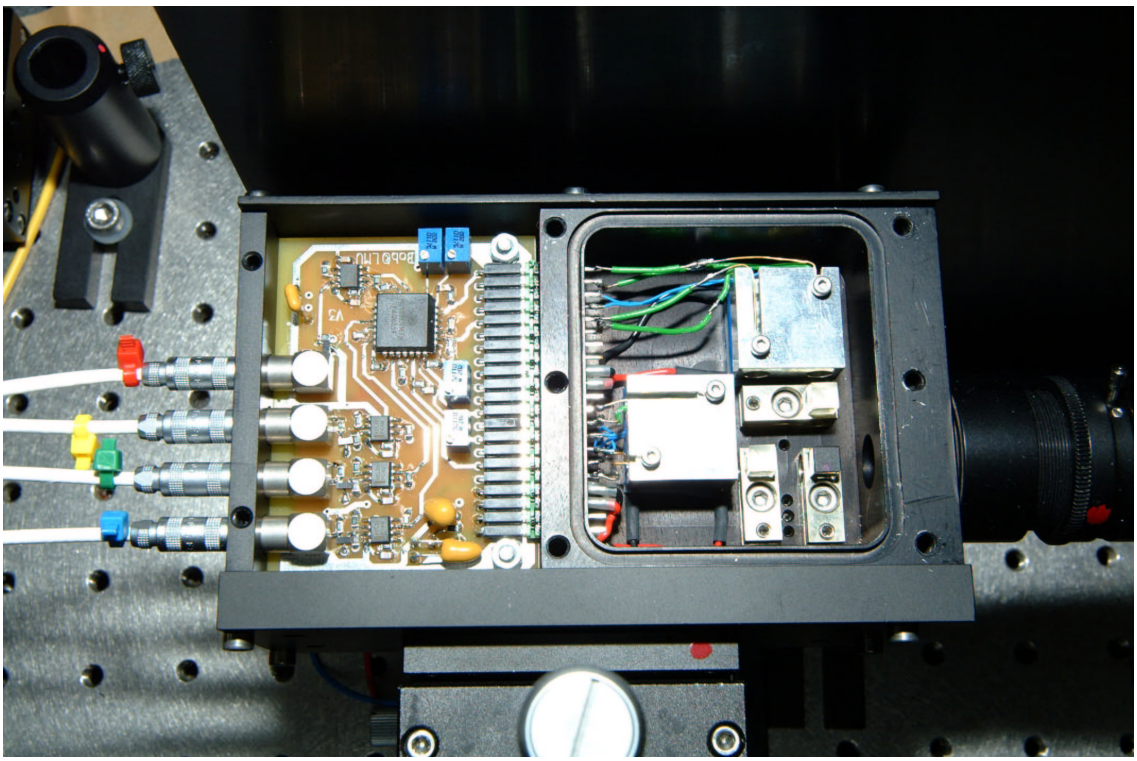

Figure 4.12: Photograph of Detector Module.

The pulses from the detectors when an avalanche was triggered were converted (s. figure A.2) into a NIM signal[6] and stretched to a width of 15 ns, and then sent to a coincidence unit described in the next section.

To verify the pathlength difference of the interferometer arms we recorded the coincidences for different detector combinations for an arbitrary input state. In figure 4.13, the detectors are denoted by the polarization observed in the output ports of the polarizing beam splitter. The data was recorded with an oscilloscope registering the relative time delay of two detector clicks. It is observed that photons with equal polarization arrive approximately simultaneously at the detectors,

[6]Logical "0" and "1" correspond to voltages of 0 V and -1 V, respectively, on a 50Ω terminating resistor.

because the photons took the same path in the interferometer. For perpendicular polarization the photons have travelled through different arms of the interferometer and hence the vertically polarized one arrives delayed at the detector with respect to the other. From the temporal separation of the two peaks, i.e. 3.4 ns, the path length difference is obtained to be 101.9 cm.

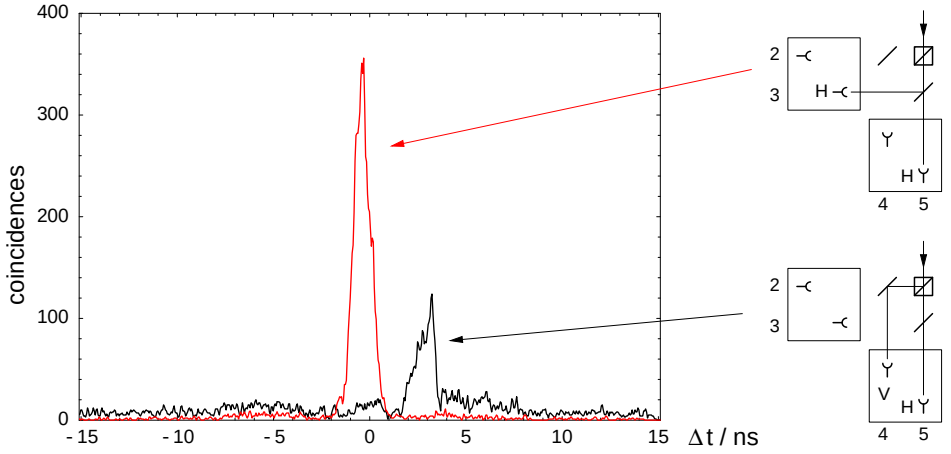

Figure 4.13: Coincidence count rates for two combinations of detectors. The combination of two H detectors corresponds to two photons having travelled the short arm of the interferometer. For the combination of H and V, one photon (V) has travelled the long interferometer arm and the other (H) the the short.

The coincidence peaks shown in figure 4.13 are larger than it would be expected from the correlation time τ_C (s. section 3.3). This is due to the time resolution of the detectors and the processing of the detector signals until recorded by the oscilloscope.

Furthermore, the wings of the peaks seemed to be rather broad. Therefore, we analyzed this feature by shining in ambient light and observed the coincidences for different detector pairs; an example is given in figure 4.14. The observed peaks at $\Delta t = \pm 5$ ns are caused by optical crosstalk between two detectors. If a shutter is placed in front of one of the detectors no such peak is observed, verifying that the peak was not caused by electronical crosstalk. The peaks can be explained by the breakdown flash of the photodiodes. When a photon strikes the detector and triggers an avalanche, about 10-100 photons will be emitted in the breakdown flash, which then freely propagate in the detector module and eventually strike another detector, for example after they are reflected from one of the surfaces of the optical components. In [82] the effect was studied in more detail and a fluorescence intensity spectrum as function of the wavelength of the photons emitted in a breakdown flash is given. The emission is maximal for 850 nm photons and does not show significant contributions at 702 nm. Short-pass filters could here be used to cut off the main contributions from photons emitted in breakdown flashes.

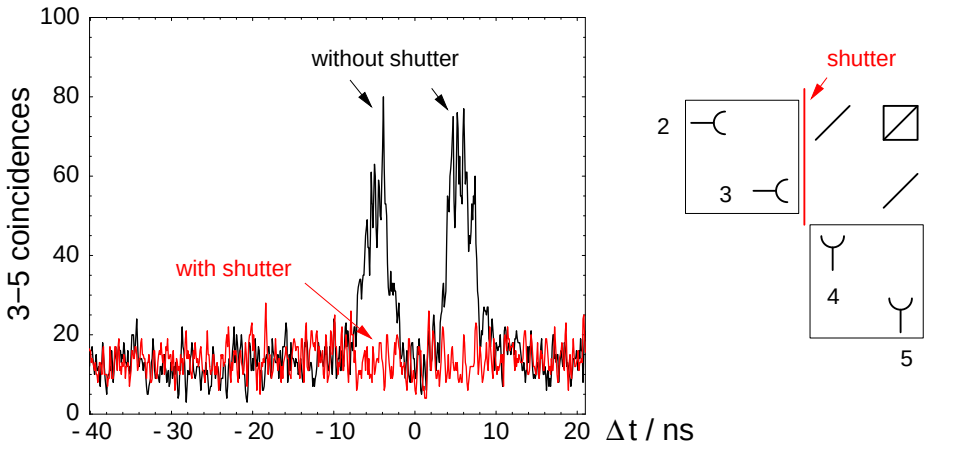

Figure 4.14: Observation of optical crosstalk between detectors 3 and 5. The high background is due to straylight.

To check if the beam splitters show an (optimal) ratio of reflectivity to transmittivity of approximately 1, a polarizer was rotated in front of the module. The observed single count rates of all four detectors are shown in figure 4.15. Both beam splitters deviate from the optimal behavior but the probability for a pair to split up depends only weakly on the ratio of reflectivity to transmittivity and hence the influence on the measurement results will be negligible.

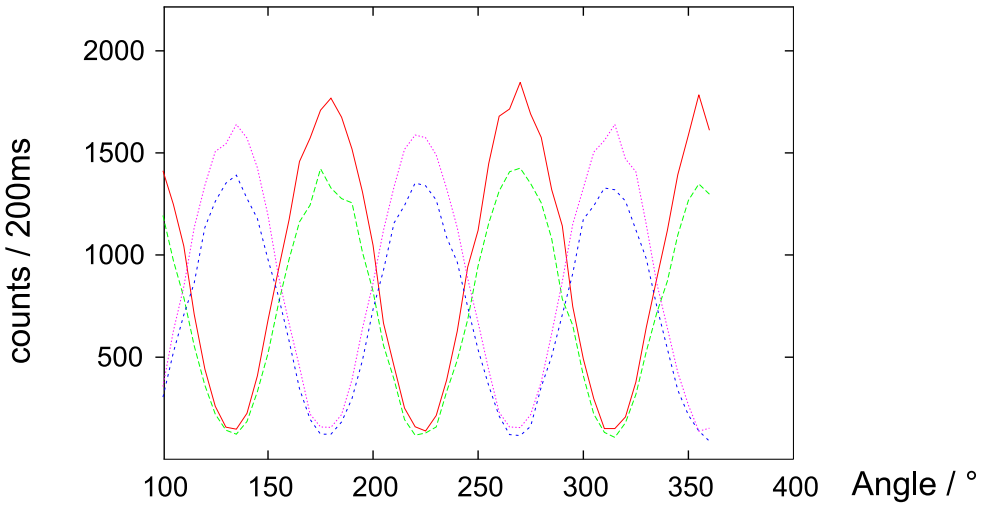

Figure 4.15: Count rates for the four detectors inside the detector module when a polarizer in front of the module is rotated.

4.3.3 The Coincidence Unit

So far it was presented how the Bell state analysis works assuming that it is possible to distinguish between the different coincidence detection events. Hence, the experiment also requires a coincidence logic which converts the signals from the detectors into an output signal telling us which of the Bell states the input signal corresponded to.

The requirements for this coincidence unit are that it needs to be able to distinguish between simultaneously arriving input signals from two detectors (for $|\psi^+\rangle$-, $|\phi^+\rangle$- and $|\phi^-\rangle$-events) and signals which arrive with a temporal separation (for $|\psi^-\rangle$-events). Thereby, the temporal separation is determined by the path length difference of the interferometer arms, which was measured to be $\Delta t = 3.4$ ns (s. section 4.3.2). Furthermore, the coincidence time window must be shorter than half of this separation to unambiguosly distinguish photons arriving simultaneously or with a relative delay. Since the down conversion source produces photon pairs at a high rate (s. section 4.1), the coincidence unit should also be able to process these events fast enough, in order not to loose coincidence events registered by the detectors.

To meet these requirements, a fast ten-fold coincidence unit was built which can be read out by a PC. A schematic diagram of the logic and its key elements is shown in figure 4.16. Although only five detectors are used in the actual experiment, we will need ten signals for the processing to distinguish temporally separated coincidence detection events from simultaneous detector clicks.

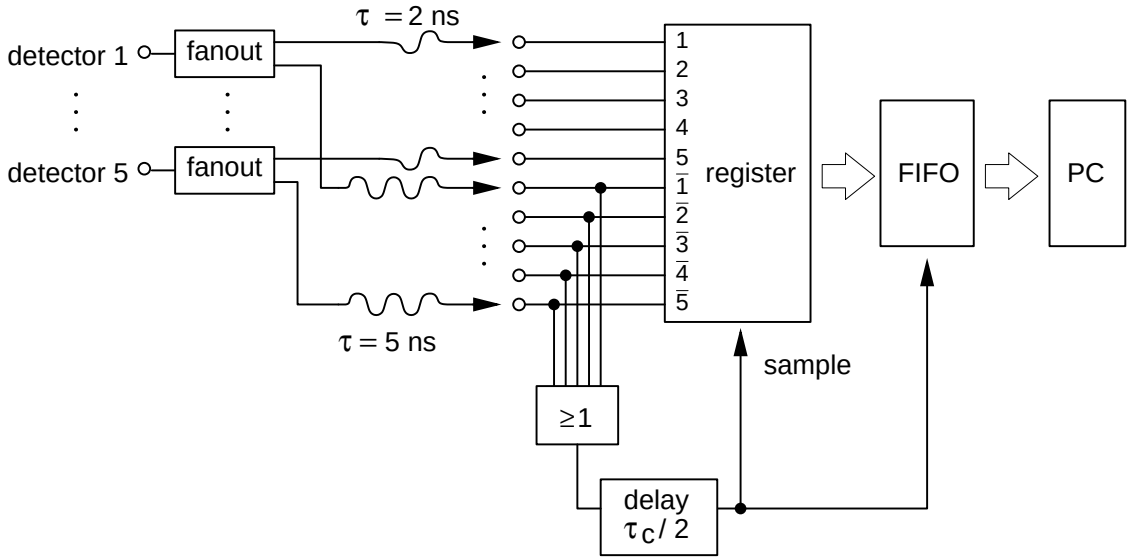

Figure 4.16: Schematic diagram of the 10–fold coincidence unit

The NIM signals from the detector module are first fed into a fanout, where the signal is copied. One of the copies is then sent through a short NIM cable, while another copy has to travel through a longer cable. Essentially, the length-difference between the two cables should correspond to the temporal separation with which simultaneously created photons travelling through different arms of the interferometer arrive at the detectors. However, due to the commercial availability of integer valued NIM cables, the temporal delay of two pulses from one fanout unit at the detector in our case was 3 ns instead of $\Delta t = 3.4$ ns. A simple improvement will therefore be to shorten the long arm of the interferometer by about 6 cm to synchronize the optical and electronic delays.

If one of the inputs of the coincidence unit for the delayed copies from the fanouts changes its logical state as a consequence of a detector event, the whole pattern of the ten detector inputs (delayed and undelayed copies) is sampled into a register after some well defined time delay $\tau_C/2$. This time delay corresponds to half of the coincidence time window τ_C and can be adjusted. For our purpose τ_C was set to ~ 1.5 ns.

The difference between a signal from one of the detectors arriving early or late at the fanouts should be equal to (or at least lie within the coincidence time window τ_C) the relative delay of two signals from one fanout. In this case, detector signals arriving at the fanouts with an according temporal separation will lead to a different sampled pattern than signals arriving simultaneously, as shown in figure 4.17. Consider for example the identification of a $|\psi^-\rangle$: The horizontally polarized photon will travel the short arm of the interferometer, while the vertically polarized one will travel the long path. Hence, the horizontally polarized photon will arrive earlier at a detector. Then its delayed copy from the fanout will cause the logical OR gate (denoted by ≥ 1 in figure 4.16) to send to the register a sample command after a time delay of $\tau_C/2$. By the time this signal reaches the register to initiate the sampling, the vertically polarized photon will have travelled the longer path and will be detected. However, one of its copies which had to pass through the longer NIM cable will not have had time to reach the register before the sampling is done. The sampling pattern given in the upper part of figure 4.17 will then be written to the register.

If the two photons arrive simultaneously (as it is the case for the other three Bell states) at two different detectors, one of their delayed detector signals will start the sampling, but in this case also the delayed copy of the other signal will have time to reach the register before the sampling is done (lower part of figure 4.17). This results in a sampled pattern which is different from the above case, and therefore will allow to distinguish between the $|\psi^-\rangle$ and the other three Bell states.

In each case the sampled pattern will contain the information which detector sent a signal, and when the signal was sent relative to other detector events. These patterns are then written to an event buffer (the FIFO) which only takes 15 ns to store the data before the next event can be recorded. In this way it is ascertained

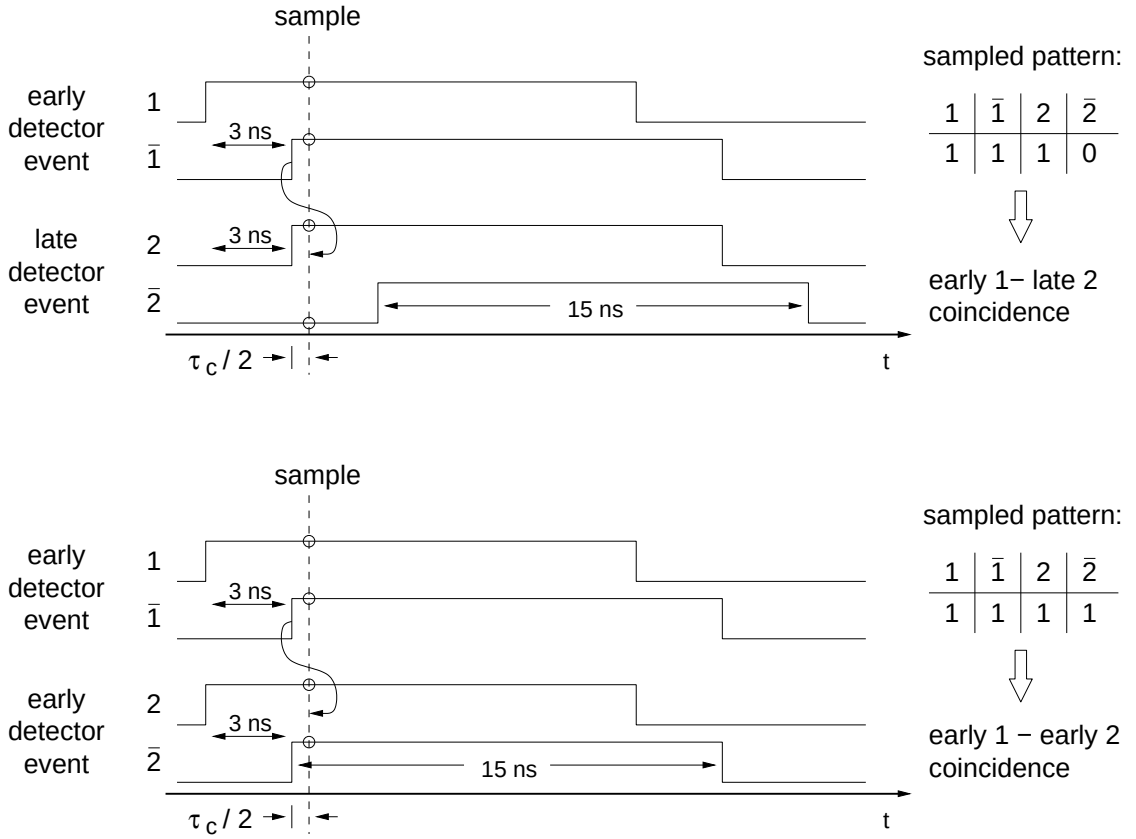

Figure 4.17: Sample patterns for detection events at different times (above) and at the same time (below).

that no events are lost up to high single-event rates. From the buffer the raw-data (i.e. the patterns) can be read out by a high-speed digital input card into the PC for the event-histogramming. This readout may for some time also take place at a slower rate. The average event rate for the unit is limited by the digital input card to approximately 10^6 events per second.

This ten-fold coincidence unit was used for the collection of the data presented in the following. It fulfills all of the requirements formulated in the beginning of this section and will therefore allow to distinguish between the different detection events of the four Bell states according to figure 4.18.

		Alice	
		C	D
Bob	C	$\lvert\phi^+\rangle$ D_2D_4 D_3D_5	$\lvert\psi^+\rangle$ D_1D_2 D_1D_4 $D_1\overline{D_2}$ $D_1\overline{D_4}$ D_1D_3 D_1D_5 $D_1\overline{D_3}$ $D_1\overline{D_5}$
	D	$\lvert\psi^-\rangle$ $D_2\overline{D_3}$ $D_3\overline{D_4}$ $\overline{D_2}D_3$ $\overline{D_3}D_4$ $D_2\overline{D_4}$ $D_3\overline{D_5}$ $\overline{D_2}D_4$ $\overline{D_3}D_5$ $D_2\overline{D_5}$ $D_4\overline{D_5}$ $\overline{D_2}D_5$ $\overline{D_4}D_5$	$\lvert\phi^-\rangle$ D_2D_3 D_3D_4 D_2D_5 D_4D_5

Figure 4.18: According to the calculation performed in section 3.3 one kann identify Bell states with the coincidence detection events. Here $\overline{D}_i$ denotes a detector which will click later than another detector D_j.

4.4 Results of a Complete Bell measurement

For the implementation of a quantum game it is necessary to be able to distinguish between all four Bell states (sections 3.2 and 3.3). To show that a complete Bell measurement is possible with the presented setup, a dense coding protocol was realized. This protocol demonstrates how more than one bit of information can be sent by manipulating only one qubit. Different from previous implementations of dense coding protocols [13], it was shown here for the first time that it is experimentally possible to transmit one of *four* possible messages by manipulating only one qubit of an entangled pair.

As in the case of the observation of HOM-interference the down conversion was set such that the state $|\psi^-\rangle$ can be observed behind a combination of one $\lambda/2$- and one $\lambda/4$-waveplate in one arm, both set to 0°. This was verified by measuring the polarization correlations (s. section 4.1) right after the waveplates in one and the fiber coupler in the other arm. By setting the angles of the waveplates, one can prepare all other Bell states, which are then incident on the first beam splitter in the setup for the complete Bell state analysis. Then, the measurements of the HOM-interference presented in in section 4.2 were performed and the position of the fiber coupler was fixed at the point where the coincidence rate was maximal for the $|\psi^+\rangle$, and minimal for the other three Bell states. For a defined input state ($|\phi^+\rangle$ or $|\phi^-\rangle$), we aligned the glass plate in the interferometer such that only the combinations of detectors given in table 4.18 (corresponding to the input state) show maximal count rates, while minimal count rates are observed for the other combinations. In this way, the same relative phase as assumed in the calculation in section 3.3 is obtained, which is important to identify the $|\phi^+\rangle$ and the $|\phi^-\rangle$ states (the $|\psi\rangle$ states are unaffected by a change of the relative phase difference of horizontal and vertical polarization behind the interferometer).

Then, we measured the coincidence events per second for all possible combinations of two detectors for four settings of the waveplates. For the initial setting, i.e. both waveplates set to 0°, the $|\psi^-\rangle$ is transmitted to the Bell state analyzer and we obtain the coincidence count rates given in figure 4.19. The count rates displayed over a measurement time of 30 s are obtained by adding up the coincidence events of all detector combinations corresponding to the identification of the same Bell state.

Then the $\lambda/4$-plate was set to 90° and the measurement was repeated. Now the $|\psi^+\rangle$ should be observable. The experimental results from the Bell state analyzer are given in figure 4.20.

Similar the remaining two Bell states were prpared by setting the $\lambda/2$-waveplate to 45°, and then switching the $\lambda/4$-plate between 0° for the $|\phi^-\rangle$ and 90° for the $|\phi^+\rangle$. The experimental results for 30 s of measurement time are given in figures 4.21 and 4.22, respectively.

As mentioned in section 3.3, the probabilities to be able to detect either one of the Bell states are different for every Bell state. Namely a probability of 100%

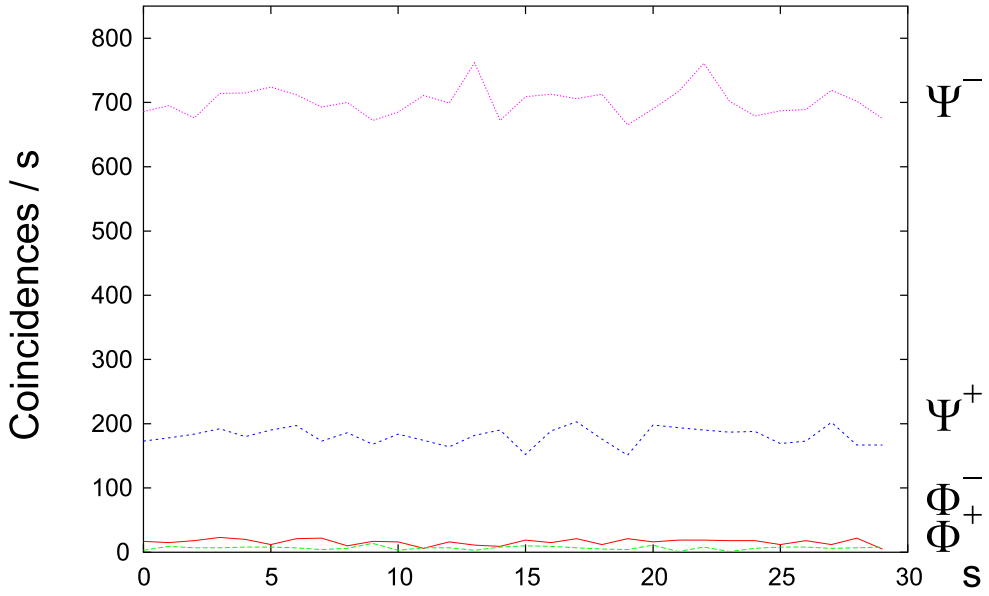

Figure 4.19: Totaled count rates per second of all detector combinations corresponding to one of the four Bell states for the $|\psi^-\rangle$ as input state.

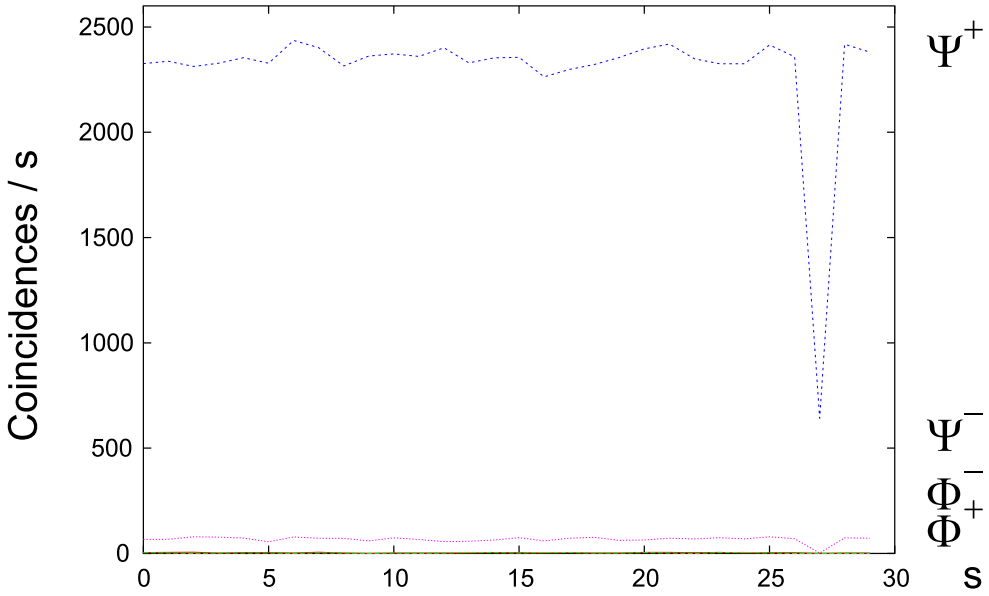

Figure 4.20: Totaled count rates per second of all detector combinations corresponding to one of the four Bell states for the $|\psi^+\rangle$ as input state. The pronounced dip is caused by some electronic crosstalk which we could not completely get rid of.

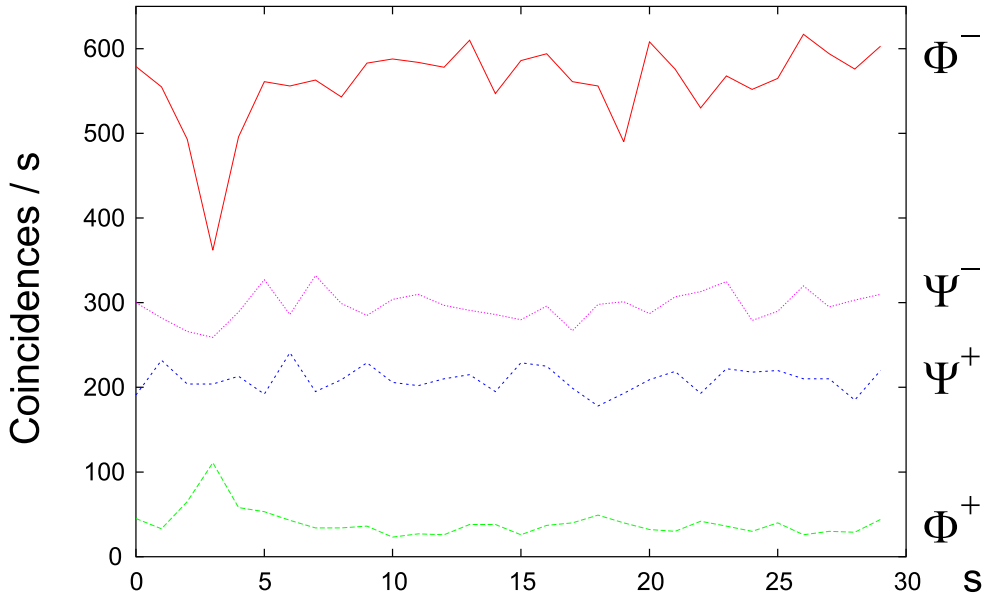

Figure 4.21: Totaled count rates per second of all detector combinations corresponding to one of the four Bell states for the $|\phi^-\rangle$ as input state.

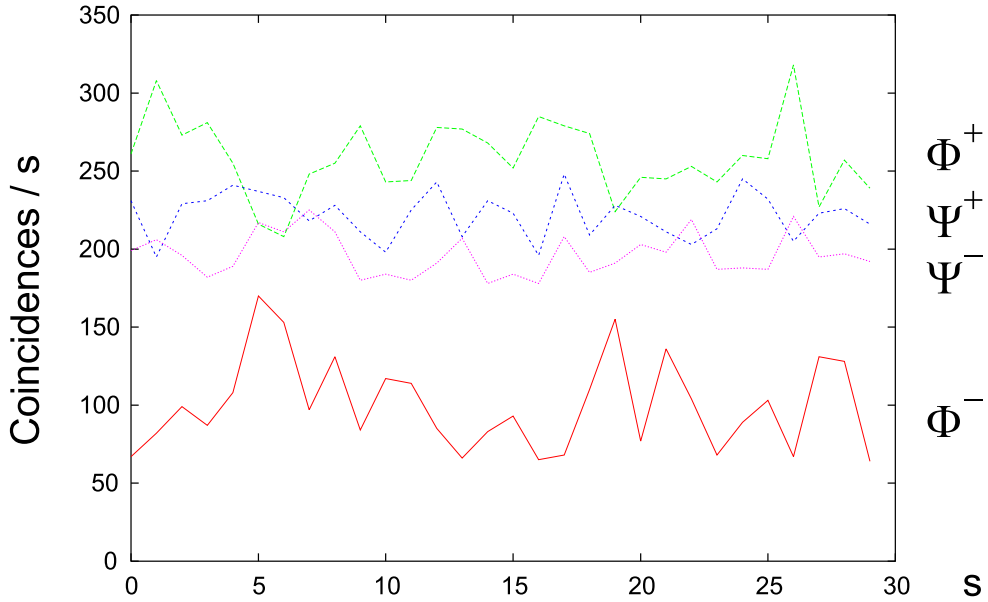

Figure 4.22: Totaled count rates per second of all detector combinations corresponding to one of the four Bell states for the $|\phi^+\rangle$ as input state.

was only obtained for finding the $|\psi^+\rangle$, while the other three Bell states have lower detection efficiencies: 50% for the $|\phi^-\rangle$, 37.5% for the $|\psi^-\rangle$, and only 25% for the $|\phi^+\rangle$. As explained in 3.3, this is due to the different possibilities of two-photon states in one spatial mode splitting up at beamsplitters. Taking this into account by multiplying the measured count rates with the inverse of the probabilities, the final results (within this work) are obtained for the Bell state analyzer, shown in figures 4.23-4.26.

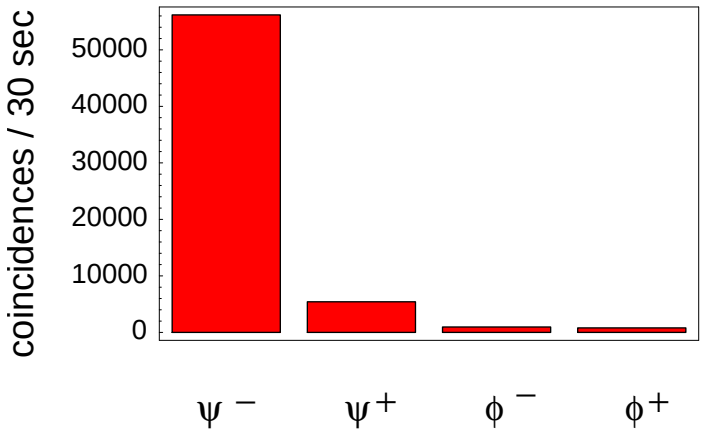

Figure 4.23: Totaled coincidence count rates recorded over 30 seconds for all four Bell states. Input state for the Bell state analyzer was the $|\psi^-\rangle$. The count rates have been multiplied by the inverse of the probabilities to compensate for different detection efficiencies of the four Bell states.

The results show that the Bell state analyzer reliably identifies the $|\psi^-\rangle$ and the $|\psi^+\rangle$. For the two $|\phi\rangle$ states the input state was found with a higher probability than any other Bell state. However, the background was rather high for these states.

The observed background for all of the four Bell states is mainly due to deficiencies in the stabilization of the interferometer and the deviations of the HOM-dip or -bump visibilities from the optimal value of 100%. From the raw data presented in figures 4.19-4.22 it is apparent that the coincidence count rates are subject to rather large variations (up to 50%) of the count rates. These fluctuations are probably caused by instabilities in the interferometer. To enhance the stability I suggest to improve the mechanical mounting of the polarizing beam splitter and to optimize the integration time constant of the controller, as discussed in section 4.3.1. In particular it should thereby be possible to increase the reliability of the identification of the $|\phi\rangle$ states, which crucially depends on the phase stability of the interferometer (s. sections 3.3 and 4.3.1).

Another approach to improve the quality of the results is to achieve higher visibilities in the observation of HOM-interference. As observed in section 4.2, the

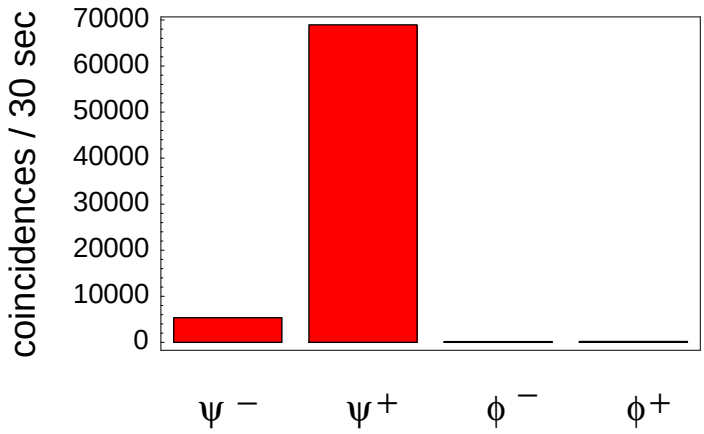

Figure 4.24: Totaled coincidence count rates recorded over 30 seconds for all four Bell states with an input state $|\psi^+\rangle$. The count rates have again been multiplied by the inverse of the probabilities.

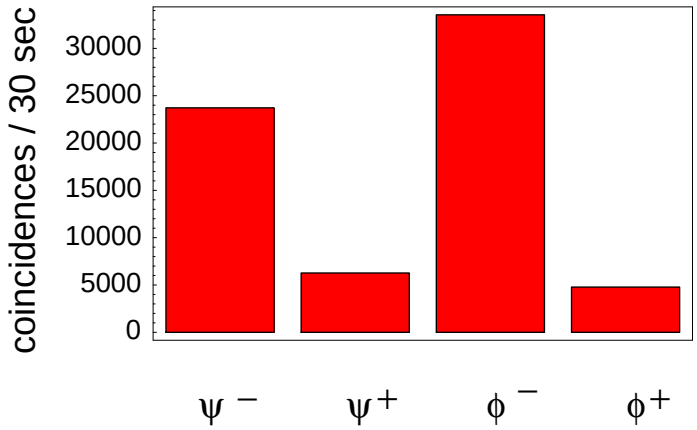

Figure 4.25: Totaled coincidence count rates recorded over 30 seconds for all four Bell states. Input state for the Bell state analyzer was the $|\phi^-\rangle$. The count rates have again been multiplied by the inverse of the probabilities.

visibilities for the $|\phi\rangle$ states were about ten percent lower than for the $|\psi\rangle$ states, which is surely one of the reasons for the higher background observed for the $|\phi\rangle$ states. Also for the $|\psi^-\rangle$ identification, a higher background of detection signals corresponding to Bell states different from the input state was found compared to the case of the $|\psi^+\rangle$. This could be an artifact of the higher visibility of the HOM-bump compared to the HOM-dips presented in section 4.2.

Certainly an improvement of the HOM-interference, which crucially depends

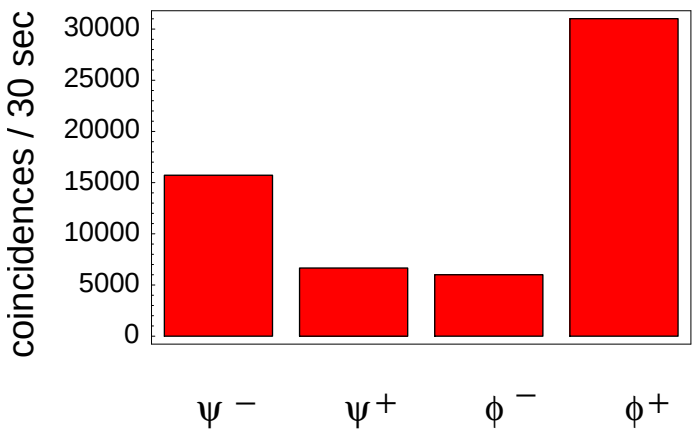

Figure 4.26: Totaled coincidence count rates recorded over 30 seconds for all four Bell states. Input state for the Bell state analyzer was the $|\phi^+\rangle$. The count rates have again been multiplied by the inverse of the probabilities.

on spatial mode matching, as mentioned in sections 3.3 and 4.2, would lead to a better reliability of the Bell measurement. It should also be checked that the different HOM-interference visibilities are correlated with different settings of the waveplates, because wedges of the plates would lead to a reduced quality of the mode matching. This would somehow complicate the implementation of the prisoner's dilemma, because for such an experiment many more waveplates are needed for the realization of different strategies.

5 Conclusion & Outlook

Within the scope of this thesis it has for the first time been demonstrated how a complete Bell state measurement can be realized. A simple non-trivial network of quantum logic gates has been implemented with linear optical elements. The presented setup will allow the realization of new quantum information processing protocols, in particular the first implementation of a quantum game.

Quantum game theory emerged from a combination of quantum information theory and the theory of games, which are both concerned with the communication of information. For the implementation of the quantum version of a classical example of game theory, the prisoner's dilemma, it is necessary to provide the players with an entangled initial state on which they will have to perform quantum strategies to obtain a new solution to the classically unsolvable game [44]. Subsequently, it has to be possible to determine the benefits of the players, which in this case requires the identification of all states of a maximally entangled basis.

To generate the entangled initial state of the game, a compact and highly efficient parametric down conversion source for entangled photon pairs was set up. Measurements of the polarization correlations, a violation of a Bell inequality and the entanglement witness verified that the collected photons are highly entangled.

For the first complete polarization Bell state measurement with linear optical elements it was made use of entanglement in higher dimensional state spaces [5]. This idea should be considered as an extension of the proposal of Knill, Laflamme and Milburn, who need auxiliary photons (ancillas) for their universal quantum logic operations [8].

As a first protocol where a complete analysis of all four polarization Bell states was performed, an optimal dense coding scheme has been realized. It was shown that the Bell states $|\psi^-\rangle$ and $|\psi^+\rangle$ could reliably be identified. However, the identification of the $|\phi^-\rangle$ and $|\phi^+\rangle$ still suffers from high background. Ideas how to improve the setup to increase the quality of the experimental data are given along the text.

This experiment can be understood as the first step towards the implementation of the prisoner's dilemma. Yet, for the current setup only one player is actively able to perform strategic moves, which may be quantum as well, while the other remains completely passive. For one player, first quantum strategies on an entangled initial state have been performed and it was shown how to arrive at classically unaccessable final states.

The obtained results demonstrate that it is possible to identify all four Bell states with linear optical elements. After an improvement of the reliability of the complete Bell state measurement, the implementation of the prisoner's dilemma is straightforward. Minor modifications of the current setup will also allow to implement new and improved protocols for efficient quantum communication tasks as well as quantum versions of other well known two-player games.

One might now hope to use the complete Bell state analysis presented here to implement improved teleportation schemes. However, the efficiency of teleportation schemes that have been implemented to date [72] will not benefit from this Bell state analyzer because the necessary time-energy correlations which are made use of are not present in qubits from different sources. For long coherence times (cw pumped sources) it is not very probable that two photons from independent creation processes will be generated simultaneously and for pulsed pumped sources the coherence time is too short to implement the analyzer.

To conclude I will give a short outlook on quantum game theory, which was the motivation for this thesis.

In the last years many classical games have been generalized to quantum games. It was found that quantum strategies and entanglement provide new solutions to classical unsolvable game situations similar to problems in quantum communication. Since many mathematical problems can be reformulated as games, it was suggested that quantum games might help to find new quantum algorithms.

For future experiments it might be interesting to consider what new possibilities arise if entanglement of multi-particle states is allowed for in multiplayer games. For example the Prisoner's dilemma can be extended to the case of three (or more) players, which is possible to implement [83, 84] using the GHZ- [85] or the W-state [86]. More multiplayer (multiparticle) games, like Vaidman's Game [87, 88] may also be interesting to study.

What hasn't been looked into in very much detail until now is what new possibilities quantum rules offer in iterated games, where the player's actions can depend on the past behavior of the other players. For the classical prisoner's dilemma it was shown in computer tournaments that the best strategy is "tit for tat"[1]. First ideas on optimal strategies in repeated quantum games are published in [91, 92].

Most applications of game theory in science have focussed on biology, at the macroscopic scale analyzing the behavior of species or individual decision makers. However, a very different perspective on quantum games has been triggered by a famous book [93] of the evolutionary biologist Richard Dawkins[2]. Dawkins speculated that games of survival are being played already on a microscopic level where

[1] Cooperate in the first round, then do whatever the other player did in the previous round. The computer tournaments and the success of the strategy is discussed in [89, 90].

[2] Dawkins reformulated the theory of natural selection. Instead of thinking about organisms using

quantum mechanics dictates the rules [43, 92]. And effectively it was recently discovery that an RNA virus - a primitive but fundamental microbiological structure - may also be engaged in a situation properly described by the prisoner's dilemma [94]. So effectively it might very well be, that after all life is just a ...

genes to reproduce themselves, he imagined that "our" genes build and maintain us, from the perspective of molecules competing for limited space and resources to produce more of their own kind.

A Appendix

A.1 Detectors

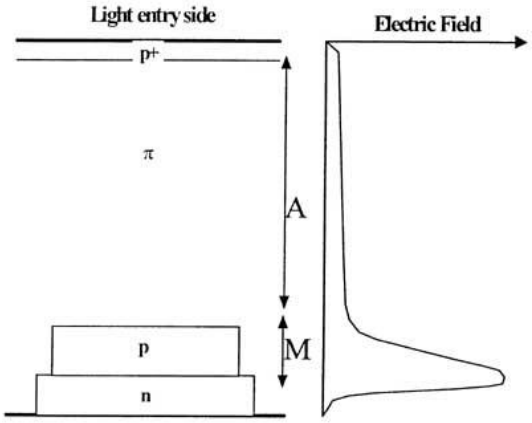

Figure A.1: Reach-through APD Structure [79]

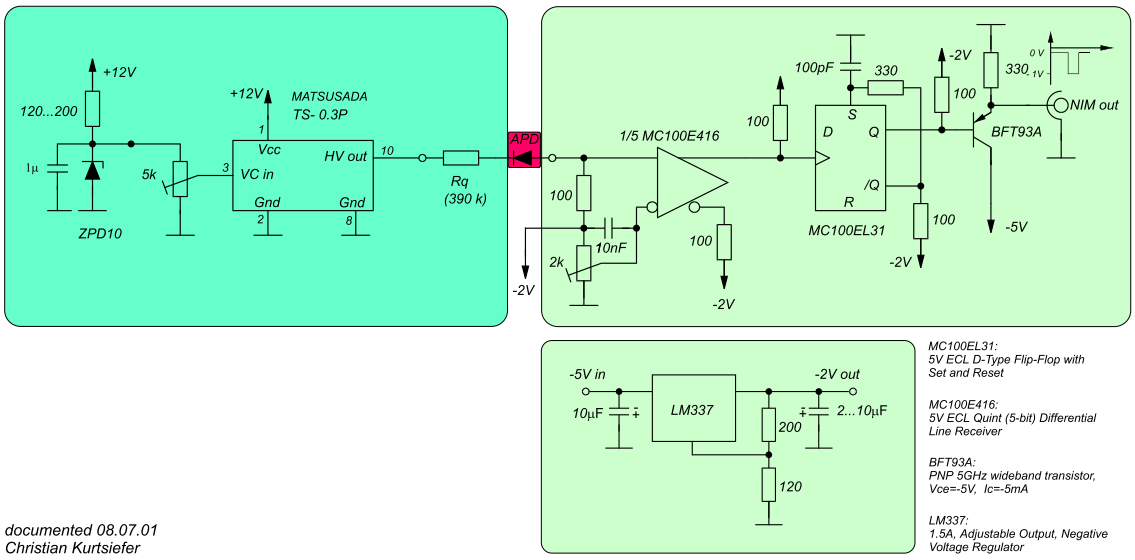

Figure A.2: Electronics circuit for the Bob detector module.

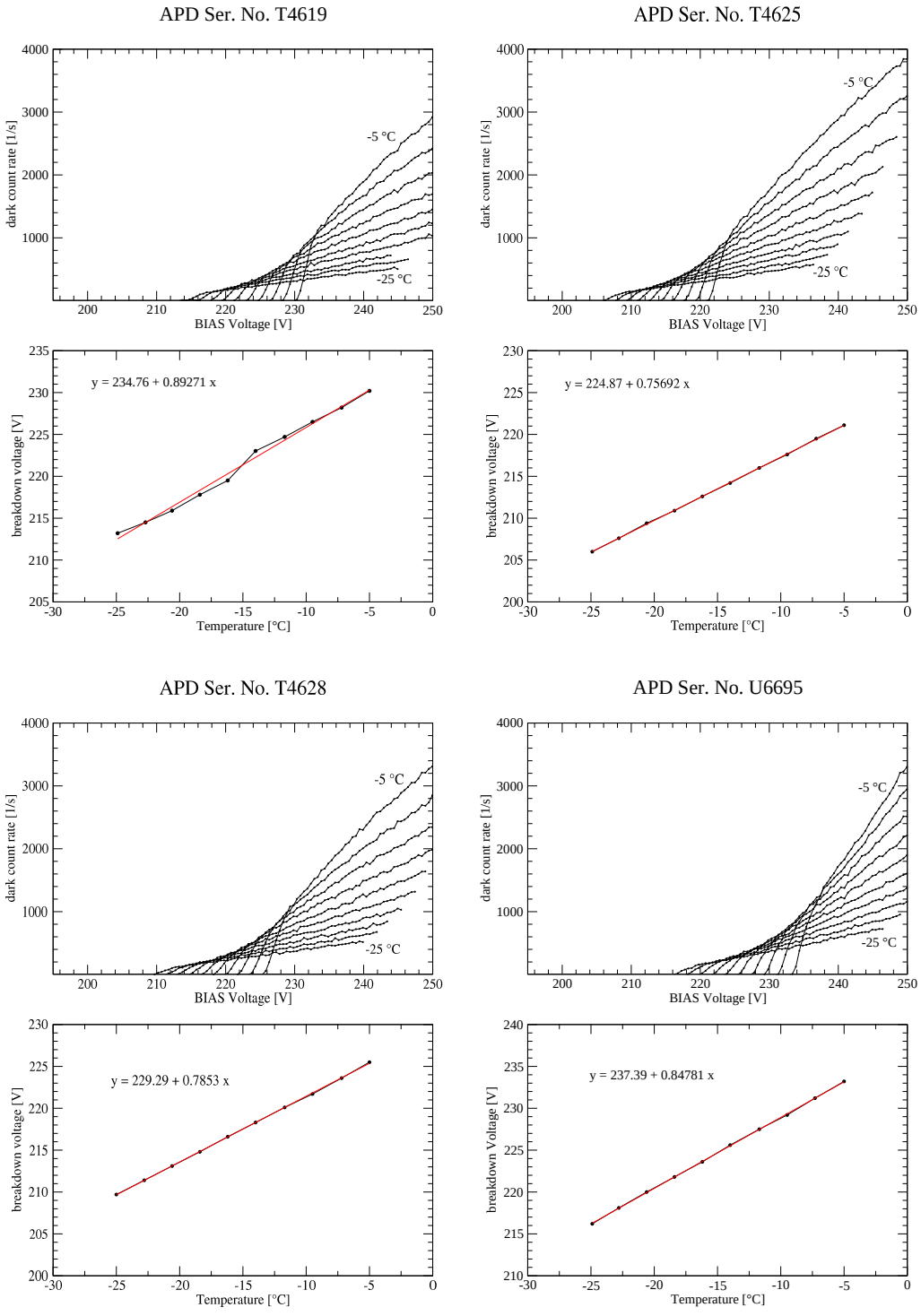

Figure A.3: Temperature dependence of the dark count rates and the breakdown voltage for the APD's used in the Bob module

A.2 Definitions & Explanations

Chicken Game

Like the Prisoner's dilemma, the game of "chicken" is a model for a diverse range of human conflicts.

The game of chicken came to public attention in the 1955 movie "Rebel Without a Cause", starring James Dean and Natalie Wood. James Dean plays Jim who is so afraid of being a 'chicken' like his father - a wimp, ineffectual and completely overshadowed by his domineering wife - that the very mention of the word in application to himself drives him wild. Jim gets mixed up with the wrong crowd and has to prove his worth in the pivotal scene of the movie: the 'chickie' run. Buzz, the head of the teens and Jim drive stolen cars to the brink of a cliff. The first one to jump from the car is a chicken. Jim sees this as a point of honor that he cannot refuse. The race is on and Buzz fails to jump since his leather jacket becomes caught on the door handle and he plunges with his car into the ocean. The movie and the game got a lot of publicity not only because it was perhaps the best of the three major movies James Dean did but also because James Dean himself died aged twenty-four in a car accident on a public highway in September 1955, shortly before the film's release, while on his way to a sports car meeting. In subsequent low-budget "juvenile delinquent" films, variations of the chicken game became almost an obligatory scene.

Since in the movie game the pure strategic space is continuous and the payoffs are discontinuous at the cliff's edge, in game theory one translates the off-the-cliff version into the abstract game of highway chicken [47]. Jim drives his hot rod south down the middle of the road while Buzz drives north. As collision threatens each driver - being aware of his reaction time and his car's turning radius (assumed to be identical for both drivers and cars) - must decide whether to ***C****ontinue* in the middle or ***S****werve* to the side [89].

The worst thing that can happen is for both players not to swerve and get killed. If a player is the only one to continue and lets the other driver swerve he is covered with glory while the other guy is "chicken" and loses face. Being chicken is the next to the worst outcome - still better than dying. However, there is a cooperative outcome if both players swerve and come out alive but no one can call the other a chicken (it is assumed that to swerve means to swerve right; if one driver would swerve right and the other one left they would both be dead and mortified).

The situation of the players in the Chicken Game can be described by the payoff matrix in Tab. A.1.

Both players want to do the opposite of whatever the other is going to do. If Jim knew with certainty that Buzz was going to swerve, he would drive straight and if he knew Buzz was going to drive straight, he would want to swerve. Hence, in pure classical strategies there exist two Nash Equilibria: $\hat{S} \otimes \hat{C}$ and $\hat{C} \otimes \hat{S}$, but

		Buzz: S	Buzz: C
Jim: S		(6,6)	(2,8)
Jim: C		(8,2)	(0,0)

Table A.1: Payoff matrix in the Chicken Game.

they have the defect of being asymmetric. Unlike for the unique Nash equilibrium in the Prisoner's Dilemma, there is no way to find out which will be realized by the players. Each player is hoping for a different asymmetric equlibrium result and the outcome may not be an equilibrium point at all.

However, there is a Nash equilibrium in mixed classical strategies with expected payoff[1] $\overline{\$}_J = \overline{\$}_B = 4$.

To investigate the new features of the game, if superpositions of classical strategies are allowed, the same sets of operations as in the Prisoner's Dilemma can be considered. A unique Pareto optimal solution emerges with payoff $\$_J = \$_B = 6$ for the two parameter set of operations and a focal equilibrium for the set of all quantum mechanically allowed local operations with payoff $\overline{\$}_J = \overline{\$}_B = 4$, as the mixed strategy in the classical game.

The classical chicken game was subject to detailed studies during the cold war [89]. Bertrand Russell, the president of the Cambridge University Labour Club, saw in chicken a metaphor for the nuclear stalemate in the nineteenfifties and describes another version of the game now known as the "canonical" chicken.

Strategists of the RAND[2] Corporation, to whom the Kennedy administration

[1] For the Nash equilibrium in mixed strategies the payoffs $\overline{\$}_J$, $\overline{\$}_B$ and probabilities p_i^α, $i = J, B$, $\alpha = S, C$ depend on the entries in the payoff matrix; e.g. for $P_{CC,i} = 0$ we find the probabilities $p_i^\alpha = \frac{1}{2}\ \forall i, \alpha$ giving $\overline{\$}_J = \overline{\$}_B = 4$, while for $P_{CC,i} = -2$ we get $\overline{\$}_J = \overline{\$}_B = \frac{14}{3}$ with probabilities $p_i^S = \frac{2}{3}$ and $p_i^C = 1 - p_i^S = \frac{1}{3}\ \forall i$. Apparently, increasing the loss from crashes reduces the equilibrium probability of continuing down the middle of the road. If the payoff for $\hat{C} \otimes \hat{C}$ reaches or exceeds the payoff for being the chicken while the opponent continues we have a different game where the only equlibrium is in pure strategies $(\hat{C} \otimes \hat{C})$ - the game has become the Prisoner's dilemma!

[2] Project-RAND (a contraction of the term research and development) derives from "operations research" conducted in World War II. It started in 1945 under special contract to the Douglas Aircraft Company as an organization to connect military planning with research and development decisions because it was realized that conventional military strategy was inadequate as wars became more terrible and complex. In 1948 RAND became an independent nonprofit organization "To further and promote scientific, educational, and charitable purposes, all for

was receptive, pointed out that U.S. - Soviet conflicts were chicken dilemmas. Leaders of both nations agreed that nuclear war was the worst possible outcome, but the horror of a third world war did not make them cooperate to avoid it. The classic instance of a political chicken dilemma is the Cuban missile crisis of October 1962 where both sides were tempted to threaten war. Either side hoped to convince the other that it was serious, so they might back down in order to prevent global holocaust, since being exploited is better than war, or as Khrushchev quoted a Russian saying: "It will be too late to cry over lost hair after your head is cut off." Like all applications of game theory to foreign relations, the identification of the Cuban missile crisis with the game of chicken depends on some assumptions about what would have happened. In this case, one has to assume that mutual rigidity would have lead to (a chance of) nuclear war and that both sides would prefer loss of face to the chance of war.

Battle of the Sexes

The Battle of the Sexes game is a non-zero sum two person static game of complete information. Alice and Bob are trying to decide how to spend the saturday evening:

- Alice would like to attend the opera (**O**)
- Bob would like to watch the football match in TV (**T**)
- and both would be happier to stay together rather than apart.

The payoff matrix takes the form of table A.2 with $\alpha > \beta > \gamma$.

Neither player can rationally eliminate one of his strategies and prefer the other, hence there are no strictly dominated strategies. One finds two Nash equilibria in pure classical strategies: $O \otimes O$ with payoffs $\overline{\$}_A = \alpha$ and $\overline{\$}_B = \beta$ and $T \otimes T$ with payoffs $\overline{\$}_A = \beta$ and $\overline{\$}_B = \alpha$. Introducing mixed classical strategies yields a third Nash Equilibrium. If Alice chooses Opera with probability $p = \frac{\alpha-\gamma}{\alpha+\beta-2\gamma}$ (and Television with probability $1-p$) and Bob with $q = \frac{\beta-\gamma}{\alpha+\beta-2\gamma}$ (Television with probability $1-q$) their payoff sum up to: $\overline{\$}_A = \overline{\$}_B = \frac{\alpha\beta-\gamma^2}{\alpha+\beta-2\gamma} < \beta < \alpha$. Again the theory fails to say which of the three Nash equilibria represents the real development of the game.

the public welfare and security of the United States of America." As they intended to make major efforts on applications of game theory John von Neumann and John Nash became RAND consultants. It was the first organization to be called a "think tank". They are best known for "thinking about the unthinkable" and their works on the consequences of nuclear war, 'push-button' warfare, the 'fail-safe' protocol, nuclear proliferation and American second-strike capabilities - or as a satirical folk song puts it: "they sit and play games about going up in flames". In recent years RANDs clients have included not only all branches of the U.S. military community but also NASA, the National Institutes of Health, the Ford Foundation, the State of California and both the New York and American Stock exchanges.

		Bob: O	Bob: T
Alice: O		(α,β)	(γ,γ)
Alice: T		(γ,γ)	(β,α)

Table A.2: Payoff matrix in the Battle of the Sexes.

Just as in the other presented games also for this one a new solution can be found if quantum strategies and entanglement are allowed for, as shown in [41, 95, 96].

Density Matrices

Density matrices for common measureable two-qubit states in the H,V basis, with

$$|P\rangle = \tfrac{1}{\sqrt{2}}(|H\rangle + |V\rangle) \qquad |M\rangle = \tfrac{1}{\sqrt{2}}(|H\rangle - |V\rangle)$$

$$|L\rangle = \tfrac{1}{\sqrt{2}}(|H\rangle + i|V\rangle) \qquad |R\rangle = \tfrac{1}{\sqrt{2}}(|H\rangle - i|V\rangle)$$

$$|HH\rangle\langle HH| = \begin{pmatrix} 1 & 0 & 0 & 0 \\ 0 & 0 & 0 & 0 \\ 0 & 0 & 0 & 0 \\ 0 & 0 & 0 & 0 \end{pmatrix} \qquad |VV\rangle\langle VV| = \begin{pmatrix} 0 & 0 & 0 & 0 \\ 0 & 0 & 0 & 0 \\ 0 & 0 & 0 & 0 \\ 0 & 0 & 0 & 1 \end{pmatrix}$$

$$|HV\rangle\langle HV| = \begin{pmatrix} 0 & 0 & 0 & 0 \\ 0 & 1 & 0 & 0 \\ 0 & 0 & 0 & 0 \\ 0 & 0 & 0 & 0 \end{pmatrix} \qquad |VH\rangle\langle VH| = \begin{pmatrix} 0 & 0 & 0 & 0 \\ 0 & 0 & 0 & 0 \\ 0 & 0 & 1 & 0 \\ 0 & 0 & 0 & 0 \end{pmatrix}$$

$$|PP\rangle\langle PP| = \frac{1}{4}\begin{pmatrix} 1 & 1 & 1 & 1 \\ 1 & 1 & 1 & 1 \\ 1 & 1 & 1 & 1 \\ 1 & 1 & 1 & 1 \end{pmatrix} \qquad |MM\rangle\langle MM| = \frac{1}{4}\begin{pmatrix} 1 & -1 & -1 & 1 \\ -1 & 1 & 1 & -1 \\ -1 & 1 & 1 & -1 \\ 1 & -1 & -1 & 1 \end{pmatrix}$$

$$|PM\rangle\langle PM| = \frac{1}{4}\begin{pmatrix} 1 & -1 & 1 & -1 \\ -1 & 1 & -1 & 1 \\ 1 & -1 & 1 & -1 \\ -1 & 1 & -1 & 1 \end{pmatrix} \qquad |MP\rangle\langle MP| = \frac{1}{4}\begin{pmatrix} 1 & 1 & -1 & -1 \\ 1 & 1 & -1 & -1 \\ -1 & -1 & 1 & 1 \\ -1 & -1 & 1 & 1 \end{pmatrix}$$

$$|LL\rangle\langle LL| = \frac{1}{4}\begin{pmatrix} 1 & -i & -i & -1 \\ i & 1 & 1 & -i \\ i & 1 & 1 & -i \\ -1 & i & i & 1 \end{pmatrix} \qquad |RR\rangle\langle RR| = \frac{1}{4}\begin{pmatrix} 1 & i & i & -1 \\ -i & 1 & 1 & i \\ -i & 1 & 1 & i \\ -1 & -i & -i & 1 \end{pmatrix}$$

$$|LR\rangle\langle LR| = \frac{1}{4}\begin{pmatrix} 1 & i & -i & 1 \\ -i & 1 & -1 & -i \\ i & -1 & 1 & i \\ 1 & i & -i & 1 \end{pmatrix} \qquad |RL\rangle\langle RL| = \frac{1}{4}\begin{pmatrix} 1 & -i & i & 1 \\ i & 1 & -1 & i \\ -i & -1 & 1 & -i \\ 1 & -i & i & 1 \end{pmatrix}$$

Partial Transposition

The partial transpose of a given state ρ is the transpose with respect to one of its subsystems. For

$$\rho = \sum_{i,j}^{M}\sum_{k,l}^{N}\langle i,k|\rho|j,l\rangle|i,k\rangle\langle j,l| = \sum_{i,j}^{M}\sum_{k,l}^{N}\langle i,k|\rho|j,l\rangle(|i\rangle_a\langle j|)\otimes(|k\rangle_b\langle l|),$$

with $\dim H_a = M \geq 2$, $\dim H_b = N \geq M$ and $|i,k\rangle$, $|j,l\rangle$ being the basis vectors, the partial transpose of ρ with respect to subsystem a writes:

$\rho^{T_a} = \sum_{i,j}^{M} \sum_{k,l}^{N} \langle i,k|\rho|j,l\rangle |j,k\rangle\langle i,l| = \sum_{i,j}^{M} \sum_{k,l}^{N} \langle i,k|\rho|j,l\rangle (|j\rangle_a\langle i|) \otimes (|k\rangle_b\langle l|)$.

Although partial transposition is not a unitary operation, it preserves the hermiticity.

Gaussian Beams

In wave optics light, propagating in the form of waves, is described by a scalar wavefunction, representing any electric or magnetic field component. This complex function of position and time, say $E(x,y,z,t)$, describing an optical wave satisfies the wave equation,

$$(\nabla^2 - \frac{1}{c^2}\frac{\partial^2}{\partial t^2})E(x,y,z,t) = 0. \tag{A.1}$$

Since a general solution of the wave equation can only be found numerically one has to find an analytical approximation. The electric field solution of a monochromatic wave is a wavefunction with harmonic time dependence. In free space and within the scalar approximation, where electromagnetic fields are assumed to be uniformly (i.e. linearly or circularly) polarized, the wave can be written in the form ([51])

$$E(x,y,z,t) = u(x,y,z)e^{i(\omega t - k(x,y,z)z)} = \widetilde{E}(x,y,z)e^{i\omega t}. \tag{A.2}$$

The paraxial wave equation

Obviously[3] the complex amplitude, $\widetilde{E}(x,y,z)$, of an electromagnetic field distribution (A.2), which is sinusodial in time, propagating in a uniform and isotropic medium (e.g. in free space) has to satisfy the scalar time-independent Helmholtz wave equation

$$(\nabla^2 + k^2)\widetilde{E}(x,y,z) = 0, \tag{A.3}$$

where $k = \frac{\omega}{c}$ is the wavenumber.

The simplest solutions to the Helmholtz equation are plane and spherical waves.

Plane waves are given by $E(\mathbf{r}) = ue^{-i\mathbf{kr}}$ where u is the complex envelope, $\mathbf{k}$ is the wavevector and $\mathbf{r} = (x,y,z)$. The wavefronts of $E(\mathbf{r})$ are seperated in phase by $\Delta(\mathbf{kr} - \phi(x,y,z)) = 2\pi n$ (with integer n), where $\phi(x,y,z)$ is the phase of the complex envelope and hence they describe parallel planes, which are perpendicular to the wavevector. The spacial distance between the planes is given by the wavelength, $\lambda = 2\pi/k$.

A spherical wave originating at $r = 0$ has a complex amplitude $E(r) = \frac{u}{r}e^{-ikr}$. In this case the wavefronts are concentric spheres centered about the origin.

If the wavefront normals make small angles ($\sin\theta \approx \theta$) with the axis of propagation, the wave is called a *paraxial wave*. The complex amplitude, $E(\mathbf{r}) = u(\mathbf{r})e^{-ikz}$,

[3] substituting (A.2) into (A.1)

is a plane wave which is modulated by the slowly varying complex envelope. For an optical beam in positive z-direction the primary spatial dependence of $\widetilde{E}(x,y,z)$ is the exponential variation, e^{-ikz}.

However, transverse plane waves are not adequate to describe the field distribution of transverse modes in laser systems. The beam's complex scalar wave amplitude, $\tilde{u}(x,y,z)$, which describes the transverse amplitude and phase profile of the beam varies slowly in x- and y-direction along the z-axis compared to the e^{-ikz}-variation of the plane wave for a narrow beam. The solutions $\tilde{u}(x,y,z)$ of the wave equation are localized near the z-axis and should have approximately spherical phase fronts when they escape from the laser due to the boundary conditions in a resonator with spherical reflectors (mirror curvature $\stackrel{!}{=}$ curvature of phase front) to give satisfactory transverse modes.

More importantly for the paraxial approximation, the z-dependence of the wave amplitude - caused mainly by diffraction and propagation effects - is small compared to the optical wavelength and also compared to the transverse variations in x- and y-directions. Hence the paraxial approximation writes $|\frac{\partial^2\tilde{u}}{\partial z^2}| \ll |2k\frac{\partial\tilde{u}}{\partial z}|$, $|\frac{\partial^2\tilde{u}}{\partial z^2}| \ll |\frac{\partial^2\tilde{u}}{\partial x^2}|$ and $|\frac{\partial^2\tilde{u}}{\partial z^2}| \ll |\frac{\partial^2\tilde{u}}{\partial y^2}|$.

One can extract the propagation factor, e^{-ikz}, and the complex amplitude is given by

$$\widetilde{E}(x,y,z) = \tilde{u}(x,y,z)e^{-ikz}. \tag{A.4}$$

Substituting this into the scalar wave equation and taking into account the paraxial approximation, i.e. the slowly varying z-dependence of $\tilde{u}(x,y,z)$, we get the **paraxial Helmholtz equation**

$$\frac{\partial^2\tilde{u}}{\partial x^2} + \frac{\partial^2\tilde{u}}{\partial y^2} - 2ik\frac{\partial\tilde{u}}{\partial z} = 0, \tag{A.5}$$

which has the same form as a two-dimensional Schrödinger equation ($z\widehat{=}t$) for a free particle.

Validity of the paraxial approximation An optical beam can be considered as a superposition of plane waves propagating at an angle θ to the z-axis. In the paraxial approximation the angles θ are assumed to be small, so that $\sin\theta \approx \tan\theta \approx \theta$. Hence in a Taylor expansion of the complex scalar wave amplitude one can neglect the $\frac{\partial^2\tilde{u}}{\partial z^2}$ terms for all plane wave components propagating at small angles in agreement with the paraxial wave approximation.

Solution to the paraxial wave equation

The field distribution of a uniform spherical wave in the paraxial approximation originating from a source point (x_0,y_0,z_0) observed at (x,y,z) and propagating in

z-direction[4] can be written in the form

$$\tilde{u}(x,y,z) = \frac{1}{R(z)} e^{-i\phi(x,y,z)}. \tag{A.6}$$

$R(z) = R_0 + z - z_0$ (with $R_0 = 0$ for $z_0 = 0$) is the radius of curvature of the spherical wave at plane z increasing linearly with distance and $e^{-i\phi(x,y,z)}$ (with $\phi(x,y,z) \propto \frac{1}{\lambda R(z)}$) is the phase variation across a transverse plane at fixed z.

To derive an exact solution of the paraxial wave equation with an amplitude rapidly falling off with transverse distance, carrying finite total power across the transverse plane and remaining (complex) Gaussian in profile at all z, one introduces complex values for the source point coordinates ($\rightarrow$ complex source point approach, s. [51]). The spherical wave amplitude (A.6) has to satisfy the paraxial wave equation for an arbitrary choice of source point coordinates and we can set $x_0 = y_0 = 0$ and replace z_0 by the complex source point $z_0 - \tilde{q}_0$ where $\tilde{q}_0$ is an arbitrary[5] complex quantity. Hence we have to substitute the radius of curvature, $R(z)$, by its complex generalization $\tilde{q}(z) = \tilde{q}_0(z) + z - z_0$ and the paraxial spherical wave (A.6) converts to the spherical-Gaussian wave originating from the complex source point which can be written as

$$\tilde{u}(x,y,z) = \frac{1}{\tilde{q}(z)} e^{-ik\frac{r^2}{2\tilde{q}(z)}} = \frac{1}{\tilde{q}(z)} \underbrace{e^{-\frac{r^2}{\mathtt{w}^2(z)}}}_{amplitude factor} \underbrace{e^{-ik\frac{r^2}{2R(z)}}}_{phase factor}, \tag{A.7}$$

where $r^2 = x^2 + y^2$ is the square of the distance of the point x,y from the axis of propagation.[6] This is the lowest order (fundamental) spherical-Gaussian beam solution of an infinite family of higher order solutions (e.g. Hermite-gaussian functions) to the free-space paraxial wave equation.

The phase factor shows an imaginary quadratic transverse variation, corresponding to a spherical wave with a real radius of curvature, $R(z)$.[7] For $z = 0$ the wavefronts are plane, i.e. $R(z) \rightarrow \infty$, the minimum value of R is obtained at $z = z_R$ and at larger distances $R \approx z$.

The amplitude factor exhibits a real quadratic transverse variation giving the Gaussian amplitude profile with a rapid transverse fall-off determined by the *Gaussian spot size*, $\mathtt{w}(z)$ (Fig. 2.6). Hence the beam retains its gaussian shape, paraboloidal

[4] i.e. $z - z_0$ is large compared to the transverse distances $x - x_0$ and $y - y_0$

[5] in 2.3.1 one chooses $\tilde{q}_0$ to fullfill the ABCD law

[6] These expressions can also be derived by substituting a trial solution of the form $\tilde{u}(x,y,z) = A(z) * \exp(-ik\frac{r^2}{2\tilde{q}(z)})$ into the paraxial wave equarion and solving the resulting differential equation.

[7] Not important for our considerations but for the sake of completeness one has to include the Guoy effect; an additional longitudinal phase shift, $\psi(z) = \tan^{-1}(z/z_R)$, of $\pm 90°$ on either side of the waist within the Rayleigh length (s.(2.35)) resulting in a larger phase velocity and spacing between the phase fronts compared to a plane wave. Thus a phase front will shift forward by half a wavelength when passing through the focal region.

wavefronts which are spherical close the z axis, but the spot size (minimum occurs at z=0) increases while propagating.

List of Figures

Bibliography

[1] R. B. Myerson. *Game Theory - Analysis of Conflict*. MIT Press, Cambridge, MA, (1991).

[2] M.A. Nielsen, I.L. Chuang. *Quantum Computation and Quantum Information*. Cambridge University Press, (2000).

[3] H. Weinfurter. *Quantum Communication with Entangled Photons*. Advances in Atomic, Molecular, and Optical Physics, **42**, 489 (2000).

[4] N. Lütkenhaus, J. Calsamiglia, K.-A. Suominen. *Bell measurements for teleportation*. Phys. Rev. A, **59**, (5) 3295 (1999).

[5] P.G. Kwiat, H. Weinfurter. *Embedded Bell-state analysis*. Phys. Rev. A, **58**, (4) R2623 (1998).

[6] A. Branco, C. H. Bennett, R. Cleve, D. P. DiVincenzo, N. Margolus, P. Shor, T. Sleator, J. A. Smolin, H. Weinfurter. *Elementary gates for quantum computation*. Phys. Rev. A, **52**, (5) 3457 (1995).

[7] T. Sleator, H. Weinfurter. *Realizable Universal Quantum Logic Gates*. Phys. Rev. Lett., **74**, (20) 4087 (1995).

[8] E. Knill, R. Laflamme, G.J. Milburn. *A scheme for efficient quantum computation with linear optics*. Nature, **409**, 46-52 (2001).

[9] O. Gühne. *Characterizing Entanglement via Uncertainty Relations*. quant-ph/0306194, (2003).

[10] C. H. Bennett, D. P. DiVincenzo. *Quantum information and computation*. Nature, **404**, 247 (2000).

[11] D. Bouwmeester, A. Ekert, A. Zeilinger (Eds.). *The Physics of Quantum Information*. Springer, Berlin, (2000).

[12] E. Schrödinger. *Die gegenwärtige Situation in der Quantenmechanik*. Naturwissenschaften, **23**, 807 (1935).

[13] K. Mattle, H. Weinfurter, P. G. Kwiat, A. Zeilinger. *Dense Coding in Experimental Quantum Communication.* Phys. Rev. Lett., **76**, 4656 (1996).

[14] A. Einstein, B. Podolsky, N. Rosen. *Can Quantum-Mechanical Description of Physical Reality Be Considered Complete?* Phys. Rev., **47**, 777 (1935).

[15] P. A. Schilpp (Ed.). *Albert Einstein, Philosopher Scientist.* MJF Books, NY, (2001).

[16] D. Bohm. *A Suggested Interpretation of the Quantum Theory in Terms of "Hidden" Variables. I & II.* Phys. Rev., **85**, (2) 166-193 (1952).

[17] D. Bohm, Y. Aharonov. *Discussion of Experimental Proof for the Paradox of Einstein, Rosen, and Podolsky.* Phys. Rev., **108**, (4) 1070 (1957).

[18] N. Bohr. *Can Quantum-Mechanical Description of Physical Reality Be Considered Complete?* Phys. Rev., **48**, 696 (1935).

[19] G. Weihs. *Ein Experiment zum Test der Bellschen Ungleichung unter Einsteinscher Lokalität.* Dissertation, (1999).

[20] B. d'Espagnat. *Conceptual Foundations of Quantum Mechanics.* Addison-Wesley Publishing Company, Inc., (1976).

[21] J.F. Clauser, M.A. Horne. *Experimental consequences of objective local theories.* Phys. Rev. D, **10**, (2) 526 (1974).

[22] J. F. Clauser, A. Shimony. *Bell's Theorem: experimental tests and implications.* Rep. Prog. Phys., **41**, 1881 (1978).

[23] J. S. Bell. *On the Einstein-Podolsky-Rosen paradox.* Physics, **1**, 195 (1964), reprinted in *Speakable and Unspeakable in Quantum Mechanics*, Cambridge University Press, Cambridge, pp. 14-21 (1987).

[24] J. F. Clauser, M. A. Horne, A. Shimony, R. A. Holt. *Proposed Experiment to Test Local Hidden-Variable Theories.* Phys. Rev. Lett., **23**, (15) 880 (1969).

[25] B.S. Cirel'son. *Quantum Generalizations of Bell's Inequality.* Lett. Math. Phys., **4**, 93 (1980).

[26] A. Aspect, J. Dalibard, G. Roger. *Experimental Test of Bell's Inequalities Using Time-Varying Analyzers.* Phys. Rev. Lett., **49**, (25) 1804 (1982).

[27] A. Aspect, P. Grangier, G. Roger. *Experimental Realization of Einstein-Podolsky-Rosen-Bohm Gedankenexperiment: A New Violation of Bell's Inequalities.* Phys. Rev. Lett., **49**, (2) 91 (1982).

[28] A. Aspect, P. Grangier, G. Roger. *Experimental Test of Realistic Local Theories via Bell's Theorem*. Phys. Rev. Lett., **47**, (7) 460 (1981).

[29] G. Weihs, T. Jennewein, C. Simon, H. Weinfurter, A.Zeilinger. *Violation of Bell's Inequality under Strict Einstein Locality Conditions*. Phys. Rev. Lett., **81**, 5039 (1998).

[30] M. Lamehi-Rachti, W. Mittig. *Quantum mechanics and hidden variables: A test of Bell's inequality by the measurement of the spin correlation in low-energy proton-proton scattering*. Phys. Rev. D, **14**, (10) 2543 (1976).

[31] M. Horodecki, P. Horodecki, R. Horodecki. *Separability of mixed states: necessary and sufficient conditions*. Phys. Lett. A, **223**, 1 (1996).

[32] M. Lewenstein, D. Bruß, J. I. Cirac, B. Kraus, M. Kuś, J. Samsonowicz, A. Sanpera, R. Tarrach. *Separability and distillability in composite quantum systems - a primer*. J. Mod. Opt., **47**, (14/15) 2481 (2000).

[33] R. F. Werner. *Quantum states with Einstein-Podolsky-Rosen correlations admitting a hidden-variable model*. Phys. Rev. A, **40**, (8) 4277 (1989).

[34] B. M. Terhal. *A family of indecomposable positive linear maps based on entangled quantum states*. Lin. Alg. Appl., **323**, 61 (2001).

[35] A. Peres. *Separability Criterion for Density Matrices*. Phys. Rev. Lett., **77**, (8) 1413 (1996).

[36] B. M. Terhal. *Bell inequalities and the separability criterion*. Phys. Lett. A, **271**, 319 (2000).

[37] M. Lewenstein, B. Kraus, J. I. Cirac, P. Horodecki. *Optimization of entanglement witness*. Phys. Rev. A, **62**, 052310 (2000).

[38] O. Gühne, P. Hyllus, D. Bruß, A. Ekert, M. Lewenstein, C. Macchiavello, A. Sanpera. *Detection of entanglement with few local measurements*. Phy. Rev. A, **66**, 062305 (2002).

[39] O. Gühne, P. Hyllus, D. Bruß, A. Eckert, M. Lewenstein, C. Macchiavello, A. Sanpera. *Experimental detection of entanglement via witness operators and local measurements*. J. Mod. Opt., **50**, (6-7) 1079 (2003).

[40] M. Barbieri, F. De Martini, G. Di Nepi, P. Matalomi, G. M. D'Ariano, C. Macchiavello. *Experimental Detection of Entanglement with Polarized Photons*. quant-ph/0307003, submitted to Phys. Rev. Lett., (2003).

[41] L. Marinatto, T. Weber. *A Quantum Approach To Static Games Of Complete Information*. Phys. Lett. A, **272**, 291-303 (2000).

[42] J. von Neumann, O. Morgenstern. *The Theory of Games and Economic Behavior*. Princeton University Press, Princeton, NJ, (1947).

[43] J. Eisert, M. Wilkens, M. Lewenstein. *Quantum Games and Quantum Strategies*. Phys. Rev. Lett., **83**, 3077-3080 (1999).

[44] J. Eisert, M. Wilkens. *Quantum Games*. J. Mod. Opt., **47**, 2543 (2000).

[45] S. C. Benjamin. *Comment on: "A quantum approach to static games of complete information"*. quant-ph/0008127, (2000).

[46] L. Marinatto, T. Weber. *Reply to "Comment on: A Quantum Approach to Static Games of Complete Information"*. quant-ph/0009103, (2000).

[47] E. Rasmusen. *Games and Information*. Blackwell, (2001).

[48] J. Du, H. Li, X. Xu, M. Shi, J.Wu, X. Zhou, R.Han. *Experimental realization of quantum games on a quantum computer*. Phs. Rev. Lett., **88**, 137902 (2002).

[49] A.P. Flitney, D. Abbott. *An introduction to quantum game theory*. quant-ph/020869, (2002).

[50] J. Eisert. *private communication*.

[51] A. Siegman. *Lasers*. University Science Books, Sausalito, CA, (1986).

[52] O. Svelto. *Principles of Lasers*. Plenum Press, New York, (1998).

[53] M. Oberparleiter. *Effiziente Erzeugung verschränkter Photonenpaare*. Dissertation, LMU München, (2002).

[54] J. Volz. *Kompakte Festkörperlichtquelle für verschränkte Photonen*. Diplomarbeit, LMU München, (2000).

[55] P. G. Kwiat, K. Mattle, H. Weinfurter, A. Zeilinger, A. V. Sergienko, Y. Shih. *New High-Intensity Source of Polarization-Entangled Photon Pairs*. Phys. Rev. Lett., **75**, 4337 (1995).

[56] C. Kurtsiefer, M. Oberparleiter, H. Weinfurter. *Generation of correlated photon pairs in type-II parametric down conversion - revisited*. J. Mod. Opt., **48**, (13) 1997 (2001).

[57] C. Kurtsiefer, M. Oberparleiter, H. Weinfurter. *High efficiency entangled photon pair collection in type II parametric fluorescence*. Phys. Rev. A, **64**, 023802 (2001).

[58] M. Zukowski, H. Weinfurter. *Four-photon entanglement from down-conversion.* Phys. Rev. A, **64**, 010102(R), (2001).

[59] M. Eibl, S. Gaertner, M. Bourennane, Ch. Kurtsiefer, Marek Zukowski, H. Weinfurter. *Experimental observation of four-photon entanglement from down-conversion.* Phys. Rev. Lett., **90**, (20) 200403 (2003).

[60] F. A. Bovino, P. Varisco, A. M. Colla, G. Castagnoli, G. Di Giuseppe, A. V. Sergienko. *Effective fiber-coupling of entangled photons for quantum communication.* quant-ph/0303126, submitted to Optics Letters, , (2003).

[61] M. Born, E. Wolf. *Principles of optics.* Cambridge University Press, (1999).

[62] A. Zeilinger. *General properties of lossless beam splitters in interferometry.* Am. J. Phys., **49**, (9) 882 (1981).

[63] M. Michler, K. Mattle, H. Weinfurter, A. Zeilinger. *Interferometric Bell-state analysis.* Phys. Rev. A, **53**, (3) R1209 (1996).

[64] S. L. Braunstein, A. Mann. *Measurement of the Bell operator and quantum teleportation.* Phys. Rev. A, **51**, (3) R1727 (1995).

[65] J. Calsamiglia, N. Lütkenhaus. *Maximum efficiency of a linear-optical Bell-state analyzer.* Appl. Phys. B, **72**, (1) 67 (2001).

[66] C. K. Hong, L. Mandel. *Theory of parametric frequency down conversion of light.* Phys. Rev. A, **31**, (4) 2409 (1985).

[67] J. D. Franson. *Bell Inequality for Position and Time.* Phys. Rev. Lett., **62**, (19) 2205 (1989).

[68] S. Friberg, C. K. Hong, L. Mandel. *Measurement of Time Delay in the Parametric Production of Photon Pairs.* Phys. Rev. Lett., **54**, (18) 2011 (1985).

[69] M. W. Mitchell, C. W. Ellenor, S. Schneider, A. M. Steinberg. *Diagnosis, prescription and prognosis of a Bell-state filter by quantum process tomography.* quant-ph/0305001, (2003).

[70] C. K. Hong, Z. Y. Ou, L. Mandel. *Measurement of Subpicosecond Time Intervals between Two Photons by Interference.* Phys. Rev. Lett., **59**, (18) 2044 (1987).

[71] T. B. Pittman, D. V. Strekalov, A. Migdall, A. V. Sergienko, Y. H. Shih. *Can Two-Photon Interference be Considered the Interference of Two Photons?* Phys. Rev. Lett., **77**, (10) 1917 (1996).

[72] I. Marcikic, H. de Riedmatten, W. Tittel, H. Zbinden, N. Gisin. *Long-distance teleportation of qubits at telecommunication wavelengths.* Nature, **421**, 509 (2003).

[73] J. Rehacek, Z. Hradil, O. Haderka, J. Perina Jr., M. Hamar. *Multiple-photon resolving fiber-loop detector.* quant-ph/0303032, (2003).

[74] O. Haderka, M. Hamar, J. Perina Jr. *Experimental multi-photon-resolving detector using a single avalanche photodiode.* quant-ph/0302154, (2003).

[75] K. Banaszek, I. A. Walmsley. *Photon counting with loop detector.* Opt. Lett., **28**, 53 (2003).

[76] S. P. Walborn, W. A. T. Nogueira, S. Padua, C. H. Monken. *Optical Bell-state analysis in the coincidence basis.* Europhysics Letters, **62**, 161 (2003).

[77] S. P. Walborn, A. N. de Oliveira, S. Padua, C. H. Monken. *Multimode Hong-Ou-Mandel interference.* quantu-ph/0212017, submitted to Phys. Rev. Lett., (2002).

[78] M. Weber. *Wie man die Werte von σ_x, σ_y und σ_z eines Spin-$\frac{1}{2}$ Teilchens bestimmt.* Diplomarbeit, LMU München, (2000).

[79] EG&G Optoelectronics. *Avalanche Photodiodes: A User's Guide.* EG&G Optoelectronics, Canada, (1999).

[80] Perkin Elmer Inc. *Product Datasheet: Silicon Avalanche Photodiodes.* Perkin Elmer optoelectronics, (2000).

[81] A. Karlsson, M. Bourennane, G. Ribordy, H. Zbinden, J. Brendel, J. Rarity, P. Tapster. *A Single Photon Counter for Long-Haul Telecom.* IEEE Circuits & Devices, **15**, (6) 34 (1999).

[82] C. Kurtsiefer, P. Zarda, S. Mayer, H. Weinfurter. *The breakdown flash of Silicon Avalanche Photodiodes - backdoor for eavesdropper attacks?* J. Mod. Opt., **48**, 2039 (2001).

[83] J. Du, H. Li, X. Xu, X. Zhou, R. Han. *Entanglement Enhanced Multiplayer Quantum Games.* Phys. Lett. A, **302**, 229 (2002).

[84] Y.-J. Han, Y.-S. Zhang, G.-C. Guo. *W state and Greenberger-Horne-Zeilinger state in quantum three-person prisoner's dilemma.* Phys. Lett. A, **295**, 61 (2002).

[85] D. Bouwmeester, J.-W. Pan, M. Daniell, H. Weinfurter, A. Zeilinger. *Observation of of Three-Photon Greenberger-Horne-Zeilinger Entanglement.* Phys. Rev. Lett., **82**, 1345 (1999).

[86] N. Kiesel. *Experimental Analysis of a Three-Photon Entangled State*. Diplomarbeit, LMU München, (2002).

[87] L. Vaidman. *Variations on the Theme of the Greenberger-Horne-Zeilinger Proof*. Found. Phys., **29**, (4) 615 (1999).

[88] A. Cabello. *Winning Vaidman's Game without unspeaskable information*. quant-ph/0306075, (2003).

[89] W. Poundstone. *Prisoner's Dilemma - John von Neumann, Game Theory, and the Puzzle of the Bomb*. Doubleday, New York, (1992).

[90] M. D. Davis. *Spieltheorie für Nichtmathematiker*. R. Oldenbourg Verlag München, (1993).

[91] A. Iqbal, A. H. Toor. *Quantum repeated games*. Phys. Lett. A, **300**, (6) 537 (2002).

[92] A. Iqbal, A. H. Toor. *Evolutionary Stable Strategies in Quantum Games*. Phys. Lett. A, **280**, (5-6) 249 (2001).

[93] R. Dawkins. *The Selfish Gene*. Oxford University Press, (1989).

[94] P. Turner, L. Chao. *Prisoner's dilemma in an RNA virus*. Nature, **398**, 441 (1999).

[95] J. Du, X. Xu, H. Li, M. Shi, X. Zhou, R. Han. *Nash Equilibrium in the Quantum Battle of Sexes Game*. quant-ph/0010050, (2001).

[96] A. Nawaz, A. H. Toor. *Worst-case Payoffs in Quantum Battle of Sexes Game*. quant-ph/0110096, (2001).

Acknowledgements

Finally, I thank everybody, who helped to finish this work.
In particular, I thank Professor Harald Weinfurter, who gave me the possibility to be part of his group. He always took the time to discuss my questions and gave me many oppotunities to get in touch with the scientific community.

Many many thanks also to Dr. Christian Kurtsiefer for constantly and patiently answering my questions, helping me in many difficult stages of the experiment as well as in the completion of this work and a lot of interesting discussions.
Furthermore, I thank Oliver Schulz for helping me to get started in the lab and for his support whenever I needed it.

For a good time with many interesting discussions and funny moments I thank:
Jürgen Volz for talking over many intriguing question, especially concerning the supply of cake and how to get the best cappuccino froth.
Patrick Zarda for a lot of funny and "surprising" insights into Austrian/Tirolian language-"phenomena".
Tobias Schmitt-Manderbach with whom I shared the office and who continuously guaranteed for many funny moments, though it might not always have been to his delight.
Henning "der-Oberpraktikant" Weier, the master of allusions, for many of the same funny moments. Take good care of Captain Ahab!
Dr. Mohamed Bourennane for a lot of jokes and discussions about scientific life. Lets see which airport we meet next.
Christian Schmid, Pavel Trojek and Manfred Eibl for the down-conversion-discussions and quite some fun time.

And of course all other members of the group, Chunlang Wang, Johannes Schachaneder, Markus Weber, Johannes Vrana, Nikolai Kiesel, Julia Lau and Sascha Gaertner for the good atmosphere.

Last, but not least, I thank my parents, who always supported me and gave me the security and freedom to live and study according to my ideas and perceptions.

Erklärung

Hiermit erkläre ich, die vorliegende Arbeit selbständig verfasst
und nur die angegebenen Quellen und Hilfsmittel verwendet zu haben.

Carsten Jens Markus Schuck
München, den 22. Juli 2002